CHIRAL METAMATERIAL AND HIGH-CONTRAST GRATING BASED POLARIZATION SELECTIVE DEVICES

A THESIS

SUBMITTED TO THE DEPARTMENT OF ELECTRICAL AND

ELECTRONICS ENGINEERING

AND THE GRADUATE SCHOOL OF ENGINEERING AND SCIENCE

OF BILKENT UNIVERSITY

IN PARTIAL FULFILLMENT OF THE REQUIREMENTS

FOR THE DEGREE OF

MASTER OF SCIENCE

By

Mehmet Mutlu

July, 2013

I certify that I have read this thesis and that in my opinion it is fully adequate, in scope and in quality, as a thesis for the degree of Master of Science.

Prof. Dr. Ekmel Özbay (Advisor)

I certify that I have read this thesis and that in my opinion it is fully adequate, in scope and in quality, as a thesis for the degree of Master of Science.

Prof. Dr. Ayhan Altıntaş

I certify that I have read this thesis and that in my opinion it is fully adequate, in scope and in quality, as a thesis for the degree of Master of Science.

Prof. Dr. Bilal Tanatar

Approved for the Graduate School of Engineering and Science:

Prof. Dr. Levent Onural
Director of the Graduate School

ABSTRACT

CHIRAL METAMATERIAL AND HIGH-CONTRAST GRATING BASED POLARIZATION SELECTIVE DEVICES

Mehmet Mutlu
M.S. in Electrical and Electronics Engineering
Supervisor: Prof. Dr. Ekmel Özbay
July, 2013

The utilization of purposely designed artificial media with engineered electromagnetic responses enables the obtaining of intriguing features that are either impossible or difficult to realize using readily available natural materials. Here, we focus on two classes of artificial media: metamaterials and high-contrast gratings. Metamaterials and high-contrast gratings are designed within the subwavelength periodicity range and therefore, they are non-diffractive. We exploit the magnetoelectric coupling effect in chiral metamaterials to design several structures. Firstly, we design a linear to circular polarization convertor that operates for x-polarized normally incident plane waves. Then, we combine the chirality feature and the electromagnetic tunneling phenomenon to design a polarization insensitive 90° polarization rotator that exhibits unity transmission and cross-polarization conversion efficiencies. Subsequently, we combine this polarization rotator with a symmetric metallic grating with a subwavelength slit for the purpose of enabling the one-way excitation of spoof surface plasmons and achieving a reversible diodelike beaming regime. Then, we exploit the asymmetric transmission property of chiral metamaterials and show that a polarization angle dependent polarization rotation and a strongly asymmetric diodelike transmission is realizable. Afterwards, a brief waveguide theory is provided and eventually, the dispersion relations for a periodic dielectric waveguide geometry are derived. Then, using these relations and considering the finiteness of the waveguide length, we show the theoretical description of high-contrast gratings. Finally, we theoretically and experimentally show that the achievement of a broadband quarter-wave plate regime is possible by using carefully designed high-contrast gratings.

Keywords: Metamaterial, chirality, asymmetric transmission, spoof surface plasmon, electromagnetic tunneling, beaming, high-contrast grating, wave plate.

ÖZET

KİRAL METAMALZEME VE YÜKSEK KONTRAST IZGARA TABANLI POLARİZASYON SEÇİCİ YAPILAR

Mehmet Mutlu
Elektrik ve Elektronik Mühendisliği, Yüksek Lisans
Tez Yöneticisi: Prof. Dr. Ekmel Özbay
Temmuz, 2013

Özellikle tasarlanmış bir elektromanyetik tepkisi olan suni malzemelerin kullanımı, doğal malzemeler ile elde edilmesi zor ya da imkansız olan etkileyici özelliklerin elde edilmesini sağlayabilir. Burada özellikle iki tür suni malzeme üzerinde durulmuştur: metamalzemeler ve yüksek kontrast ızgaralar. Metamalzemeler ve yüksek kontrast ızgaralar periyotları dalga boyundan küçük olacak şekilde dizayn edildikleri için kırınımlayıcı değillerdir. Kiral metamalzemelerde rastlanan manyetoelektrik bileşim etkisi kullanılarak çeşitli polarizasyon seçici dizaynlar yapılmıştır. İlk olarak, x yönünde lineer polarize dalgaları dairesel polarizasyona çeviren bir dizayn gösterilmiştir. Devamında ise, manyetoelektrik bileşim özelliği ve elektromanyetik tünelleme etkisi birleştirilerek polarizasyondan bağımsız olarak çalışabilen bir 90° polarizasyon çevirici dizayn edilmiştir. Bu çevirici, birim iletim ve çapraz polarizasyona çevirim verimliliği göstermektedir. Sonrasında, bu çevirici ile üzerinde dalga boyu altı bir yarık bulunan simetrik bir metalik ızgara birleştirilmiştir. Böylece, yalancı yüzey plazmonlarının tek yönlü uyarımı sağlanmış ve tersine çevrilebilir bir diyot benzeri ışıma rejimi elde edilmiştir. Ayrıca, kiral metamalzemelerin asimetrik iletim özelliği kullanılarak, polarizasyon açısına bağlı çevirim elde edilebileceği ve, ek olarak, diyot benzeri bir iletim rejiminin mümkün olduğu gösterilmiştir. Devamında, kısa bir dalga kılavuzu genel bakışı verilmiş ve periyodik dielektrik plaka dalga kılavuzları için dağılma ilişkileri hesaplanmıştır. Bu ilişkiler kullanılarak ve yüksek kontrast ızgaların sonlu yapılar olduğu göz önüne alınarak, bu yapılar için teorik hesaplamalar gösterilmiştir. Son olarak, yüksek kontrast ızgara tabanlı bir genişbant çeyrek dalga levhası dizaynı hem teorik hem de deneysel olarak çalışılmıştır.

Anahtar sözcükler: Metamalzemeler, kiralite, asimetrik iletim, yalancı yüzey plazmonları, elektromanyetik tünelleme, ışıma, yüksek kontrast ızgara, çeyrek dalga levhası.

Acknowledgements

First of all, I would like to thank Prof. Dr. Ekmel Özbay for his guidance and strong motivation throughout the course of my studies.

I would also like to thank to the Scientific and Technological Research Council of Turkey (TUBITAK) for awarding me with the graduate student scholarship.

I would like to thank Prof. Dr. Ayhan Altıntaş and Prof. Dr. Bilal Tanatar for reading and commenting on my thesis, and being in my thesis committee.

I would like to thank the Electrical and Electronics Engineering department for having supported me for the past seven years. Especially, our department secretary Mürüvet Parlakay has always helped me with the issues I had encountered during my undergraduate and graduate studies.

As arguably everyone would agree, being involved in graduate studies is a very challenging life choice. I feel very lucky to have had a companion throughout this period. It has always been a pleasure to have a friend with whom I share the same ambitions and academic goals. It should also be understood that being real friends with someone in the same research group can often be challenging. However, we managed to tackle such issues and that gives me the strong belief that we will be lifelong friends. I thank Ahmet Emin Akosman for a lot of invaluable things. I sincerely believe that he will be much happier than he has ever been in the future.

I would like to especially thank Duygu Serdar for always listening to me, motivating me, encouraging me, understanding me. Her invaluable love and support can I never forget. Her advices has always been wise and helped me greatly. I can never thank her enough.

I do not know how to thank my parents. No matter how I express my gratitude to them, it will be insufficient. They are the most perfect people in the world. I hope I can be a son worthy of them.

Contents

List of Figures

List of Tables

Chapter 1

Introduction

Nature gives us a lot of useful tools and possibilities to control the propagation of light. The utilization of metallic, dielectric, nonlinear, dispersive, anisotropic, bianisotropic, and magneto-optic materials can result in a great control of light propagation and the obtaining of the desired characteristics required for certain applications. In addition, the synthesis of new stable materials with intriguing inherent properties can be handy in order to achieve phenomenal effects that are not readily observed in already known materials. The efforts to synthesize new materials for enhanced optical absorption in solar junctions is an example. However, sometimes, even nature may not enable the highly desired effects under strictly defined conditions. For instance, one can state that the large electrical thickness of a Faraday isolator can be example to such limitations. Similarly, another limitation is encountered when the diffraction of electromagnetic radiation in certain direction is desired. Due to the extremely small inter-atomic distance in bulk media, visible or lower frequency radiation is not diffracted by a bulk medium with flat interfaces.

At this point, many researchers believe that the construction of artificial materials can guide us to a solution. For instance, one can argue that an ultrathin optical isolator can be constructed by combining a very thin layer of a magneto-optic medium and an artificially structured metal. In a similar sense, a diffracting medium can be constructed by using a dielectric medium with a periodically structured interface. Briefly, we argue that the usage of man-made artificially

structured devices can help in situations where the possibilities offered by the nature are limited. In other words, the electromagnetic response of a structured medium can be engineered in order to obtain those properties required by specific applications.

Arguably the most famous class of such artificial media is known as *metamaterials*. The science and engineering of them has become a focus of intense attention since it was shown that such materials can exhibit an artificial magnetic response, even at optical frequencies. It has been shown many times that the possibilities offered by such materials exceed well beyond the artificial magnetism. A reader familiar to the metamaterial research can agree that the most interesting possibility was the obtaining of negative refraction that is a property not possibly encountered in natural materials. Metamaterials are known to be in the periodicity range that is smaller than the operation wavelength so that the structure is not diffractive and can be analyzed within the framework of the effective medium theory under certain conditions.

Another form of artificial materials is the dielectric gratings with subwavelength periodicities. The idea of designing such structures is actually older than metamaterials. However, they have become a center of attention again with the introduction of the broadband reflection characteristics of *high-contrast gratings*, which are actually subwavelength dielectric gratings where the grating is constructed by using a material that exhibits a higher refractive index compared to the surrounding media. Such gratings have been extensively investigated and it has been shown that many functionalities of conventional optical elements can be realized by using them.

In this thesis, we exploit the intriguing possibilities offered by artificial materials to design polarization selective structures that are based on chiral metamaterials and high-contrast gratings.

1.1 Outline of the Thesis

In Chapter 2, we start by the explanation and derivation of circular transmission coefficients. Next, we show the calculation of the degree of optical activity and circular dichroism. Afterwards, we introduce our metamaterial based design that converts the x-polarized electromagnetic radiation into left- or right-handed circularly polarized radiation depending on the frequency. We finalize this chapter by introducing our metamaterial design that rotated the polarization plane of an incident wave by 90° independent of the initial polarization angle.

In Chapter 3, we first discuss the possibility of obtaining truly bound states at the surface of a corrugated perfect electric conductor. We show that such modes are allowed physically and they lead to the phenomena known as extraordinary transmission and directional beaming. We complete this chapter by introducing the composite structure that is constructed for the enabling of the one-way excitation of bound surface modes and the obtaining of a reversible diodelike directional beaming regime. This composite structure is formed by combining a symmetric metallic grating with a subwavawelength slit and the metamaterial based 90° polarization rotator presented in the previous chapter.

We begin Chapter 4 with a discussion on reciprocity in bianisotropic media. We derive the reciprocity equations and describe the required conditions for reciprocity. Next, we develop the idea of asymmetric transmission in reciprocal chiral metamaterials. Afterwards, we introduce our design that exhibits the polarization angle dependent rotation and asymmetric transmission of the linearly polarized eigenstates. We finalize the chapter by demonstrating the achievement of a diodelike transmission regime by using linear and reciprocal metamaterials.

In Chapter 5, we first develop the theory for parallel-plate metallic waveguides where the utilized metal is actually a perfect electric conductor. Then, we move onto the theory of dielectric slab waveguides. Finally, by utilizing these theories, we derive the dispersion relations for periodic dielectric slab waveguides. This chapter can be regarded as a brief overview of the waveguide theory. The main purpose of this chapter is to introduce the reader to the waveguide concept and

derive the dispersion relations for the periodic dielectric slab waveguide geometry, which are essential in developing the theory of high-contrast gratings.

In Chapter 6, we derive the theory of high-contrast gratings and demonstrate the calculation of the transmission and reflection coefficients, and field distributions for a particular geometrical parameter set. Then, we introduce our theoretical design that operates as a broadband circular polarizer in the near-infrared regime. This chapter is finalized by a description of the experimental design, which has been fabricated on a silicon-on-sapphire wafer using the nanofabrication techniques. We discuss the corresponding experimental results and show that the proposed geometry operates as a quarter-wave plate centered at the wavelength of 1.55 μm.

This thesis is completed with the conclusions, which are given in Chapter 7, of the conducted research.

Chapter 2

Polarization Conversion Using Chiral Metamaterials

2.1 Introduction

The utilization of chiral metamaterials, which are bianisotropic artificial materials, can enable the achievement of optical activity [1] and circular dichroism [2]. In spite of the fact that the chirality concept in metamaterials first emerged with the aim of achieving a negative effective refractive index [3], it has soon been realized that, from the viewpoint of engineering applications, optical activity and circular dichroism features can lead to a greater variety of possibilities. Briefly, for chiral metamaterials, electric and magnetic fields are strongly cross-coupled in the vicinity of the resonance frequencies. This cross-coupling can result in the achievement of different transmission and extinction coefficients for the circularly polarized eigenwaves [4]. This difference in transmission may result in the rotation of the polarization plane of the incident plane wave, i.e., optical activity, and modification of the ellipticity parameter of the incident wave, i.e., circular dichroism. A vast number of microwave, terahertz, and optical chiral metamaterial designs that benefit from the optical activity and the circular dichroism features have been proposed in the literature [5–13].

In the effective-medium description context of reciprocal chiral metamaterials,

the strength of chirality is characterized by the chirality parameter, κ, and the constitutive relations inside the material are written as [14]:

$$\begin{pmatrix} \mathbf{D} \\ \mathbf{B} \end{pmatrix} = \begin{pmatrix} \epsilon_0\epsilon & i\kappa/c_0 \\ -i\kappa/c_0 & \mu_0\mu \end{pmatrix} \begin{pmatrix} \mathbf{E} \\ \mathbf{H} \end{pmatrix}. \tag{2.1}$$

The immediate qualitative implication of Eq. 2.1 is the observation that **D** and **B** fields are related to both **E** and **H** fields. This observation leads to the fact that **E** and **H** fields are coupled in a chiral medium. In other words, an excited electric dipole can result in the excitation of a magnetic dipole and vice versa. Therefore, it is possible to detect an electric field component at the exit interface that is orthogonal to the electric field direction of the incident wave.

In this chapter, we will first show the relation between the linear and circular transmission coefficients, and then derive the analytical expressions for the degree of optical activity and circular dichroism. Afterwards, we will demonstrate the design and characterization of an asymmetric chiral metamaterial based circular polarizer. We will complete this chapter by the analysis of a 90° polarization rotator, which can operate irrespective of the incident polarization angle and based on a fourfold rotational symmetric chiral metamaterial geometry.

2.2 Circular Transmission Coefficients

We mentioned that circularly polarized waves are the eigenwaves of chiral materials. However, most of the time, linear transmission coefficients are obtained from a reflection/transmission monitor in the simulations and from experimental measurements. Therefore, it is often required to transform the linear coefficients to the circular ones, which are more appropriate for characterizing a chiral material. In doing this transformation, one can use matrix algebra and make a change of basis vectors, see Ref. [15]. However, in this section, we will follow a longer but more instructive approach in determining the transformation relations from linear to circular transmission coefficients.

First of all, we assume that the incident plane wave propagates in the $+z$ direction and this direction is normal to the material plane. Then, we start the analysis by relating the transmitted and incident fields in the x and y directions with the aid of a transmission matrix as follows:

$$\begin{pmatrix} E_x^t \\ E_y^t \end{pmatrix} = \begin{pmatrix} T_{xx} & T_{xy} \\ T_{yx} & T_{yy} \end{pmatrix} \begin{pmatrix} E_x^i \\ E_y^i \end{pmatrix}. \tag{2.2}$$

In Eq. 2.2, E^i and E^t denote the incident and transmitted electric fields, respectively. The elements of the transmission matrix are defined such that T_{ij} denotes the contribution of the j-polarized component of the incident field to the i-polarized component of the transmitted field. Eq. 2.2 can also be written as follows:

$$E_x^t = T_{xx}E_x^i + T_{xy}E_y^i, \tag{2.3a}$$

$$E_y^t = T_{yx}E_x^i + T_{yy}E_y^i. \tag{2.3b}$$

The next step is the decomposition of the incident electric field into its right-hand circularly polarized (RCP, $+$) and left-hand circularly polarized (LCP, $-$) components. We can express the incident field as a sum of RCP and LCP basis vectors as follows:

$$\begin{pmatrix} E_x^i \\ E_y^i \end{pmatrix} = A\,\frac{1}{\sqrt{2}}\begin{pmatrix} 1 \\ +i \end{pmatrix} + B\,\frac{1}{\sqrt{2}}\begin{pmatrix} 1 \\ -i \end{pmatrix}. \tag{2.4}$$

By using Eq. 2.4, coefficients of the RCP and LCP components (A and B, respectively) can simply be expressed as:

$$A = \frac{1}{\sqrt{2}}\left(E_x^i - iE_y^i\right), \tag{2.5a}$$

$$B = \frac{1}{\sqrt{2}}\left(E_x^i + iE_y^i\right). \tag{2.5b}$$

Now, we can express the transmitted electric field in terms of RCP and LCP

waves by using the circular transmission coefficients as follows:

$$\begin{pmatrix} E_x^t \\ E_y^t \end{pmatrix} = \frac{1}{\sqrt{2}} T_{++} A \begin{pmatrix} 1 \\ +i \end{pmatrix} + \frac{1}{\sqrt{2}} T_{-+} A \begin{pmatrix} 1 \\ -i \end{pmatrix} + \frac{1}{\sqrt{2}} T_{+-} B \begin{pmatrix} 1 \\ +i \end{pmatrix} + \frac{1}{\sqrt{2}} T_{--} B \begin{pmatrix} 1 \\ -i \end{pmatrix}. \quad (2.6)$$

In Eq. 2.6, T_{++} and T_{--} are the co-polarized circular transmission coefficients, and T_{-+} and T_{+-} are the cross-polarized ones. Next, by rearranging the terms of Eq. 2.6, we obtain the following two equations:

$$E_x^t = \frac{1}{\sqrt{2}} \left(T_{++}\ A + T_{-+}\ A + T_{+-}\ B + T_{--}\ B \right), \quad (2.7a)$$

$$E_y^t = \frac{i}{\sqrt{2}} \left(T_{++}\ A - T_{-+}\ A + T_{+-}\ B - T_{--}\ B \right). \quad (2.7b)$$

By equating Eqs. 2.3 and 2.7, we obtain the following equation set:

$$T_{xx} = \frac{1}{4} \left(T_{++} + T_{-+} + T_{+-} + T_{--} \right), \quad (2.8a)$$

$$T_{xy} = \frac{i}{4} \left(-T_{++} - T_{-+} + T_{+-} + T_{--} \right), \quad (2.8b)$$

$$T_{yx} = \frac{i}{4} \left(T_{++} - T_{-+} + T_{+-} - T_{--} \right), \quad (2.8c)$$

$$T_{yy} = -\frac{1}{4} \left(-T_{++} + T_{-+} + T_{+-} - T_{--} \right). \quad (2.8d)$$

Equation 2.8 forms a set of four equations and the number of unknowns is four; T_{++}, T_{-+}, T_{+-}, and T_{--}. Therefore, this equation set can be solved concurrently in order to determine the solutions. After simple algebraic steps, one can solve the equation set and the solutions are given by

$$T_{++} = \frac{1}{2} \left[(T_{xx} + T_{yy}) + i(T_{xy} - T_{yx}) \right], \quad (2.9a)$$

$$T_{+-} = \frac{1}{2} \left[(T_{xx} - T_{yy}) - i(T_{xy} + T_{yx}) \right], \quad (2.9b)$$

$$T_{-+} = \frac{1}{2} \left[(T_{xx} - T_{yy}) + i(T_{xy} + T_{yx}) \right], \quad (2.9c)$$

$$T_{--} = \frac{1}{2} \left[(T_{xx} + T_{yy}) - i(T_{xy} - T_{yx}) \right]. \quad (2.9d)$$

By using the circular transmission coefficients given in Eq. 2.9, we can define a transmission matrix for circularly polarized waves and, then, the incident and transmitted waves can be related by following a similar notation to Eq. 2.2 as follows:

$$\begin{pmatrix} E_+^t \\ E_-^t \end{pmatrix} = \begin{pmatrix} T_{++} & T_{+-} \\ T_{-+} & T_{--} \end{pmatrix} \begin{pmatrix} E_+^i \\ E_-^i \end{pmatrix}. \tag{2.10}$$

In fourfold rotational symmetric chiral structures, cross-polarization conversion for the circularly eigenwaves do not occur due to symmetry and reciprocity concerns and as a result, we have $T_{-+} = T_{+-} = 0$ for such structures. This implies that only an RCP (LCP) wave is transmitted when an RCP (LCP) wave is incident on the chiral structure. By setting the cross-polarized circular transmission coefficients as zero and using Eqs. 2.9(a) and 2.9(d), we obtain

$$T_{yy} = T_{xx}, \tag{2.11a}$$

$$T_{xy} = -T_{yx}. \tag{2.11b}$$

Then, T_{++} and T_{--} for fourfold rotational symmetric chiral structures are given by

$$T_{++} = \frac{1}{2}\left(T_{xx} - iT_{yx}\right), \tag{2.12a}$$

$$T_{--} = \frac{1}{2}\left(T_{xx} + iT_{yx}\right). \tag{2.12b}$$

It is noteworthy that, in Eq. 2.12, the terms are multiplied by $1/2$ due to normalization concerns and by doing so, we ensure that $|T_{++}|^2 + |T_{--}|^2 \leq 1$ is always satisfied.

2.3 Degree of Optical Activity and Circular Dichroism

In Sec. 2.1, we stated that chiral metamaterials have the peculiarity of rotating the polarization plane angle and modifying the ellipticity of the polarization ellipse of an incident wave. These features are named optical activity and circular dichroism, respectively. In this section, we aim to relate the degree of rotation of the polarization plane and the degree of circular dichroism to the circular transmission coefficients given in Eq. 2.12. For simplifying the calculations, without loss of generality, we assume that the incident plane wave is linearly polarized with an electric field vector in the x direction.

First of all, we define the complex linear transmission coefficients as follows:

$$T_{xx} = T_1 + iT_2 = C_1 e^{i\phi_1}, \tag{2.13a}$$

$$T_{yx} = T_3 + iT_4 = C_2 e^{i\phi_2}. \tag{2.13b}$$

Note that, in the general case, transmission coefficients are complex valued parameters since they carry both amplitude and phase information. Now, we can express the degree of rotation of the polarization plane in terms of the linear transmission coefficients as follows [16]:

$$\psi = \frac{1}{2}\tan^{-1}\left(\frac{2C_2/C_1\cos(\phi_2 - \phi_1)}{1 - C_2^2/C_1^2}\right). \tag{2.14}$$

By using Eq. 2.13 and simple complex calculus, we can easily arrive to the following expressions:

$$\cos\phi_1 = T_1/C_1, \tag{2.15a}$$

$$\sin\phi_1 = T_2/C_1, \tag{2.15b}$$

$$\cos\phi_2 = T_3/C_2, \tag{2.15c}$$

$$\sin\phi_2 = T_4/C_2. \tag{2.15d}$$

It can be shown that we obtain the following expression after combining Eqs.

2.14 and 2.15:

$$\psi = \frac{1}{2}\tan^{-1}\left(2\,\frac{T_1T_3 + T_2T_4}{C_1^2 - C_2^2}\right). \tag{2.16}$$

We use the trigonometric identity

$$\tan(\alpha - \beta) = \frac{\tan\alpha - \tan\beta}{1 + \tan\alpha\tan\beta} \tag{2.17}$$

for the purpose of expressing the argument of the inverse tangent function in Eq. 2.16 as a sum of the tangent of two functions. Accordingly, after simple algebraic steps, we observe that Eq. 2.17 gives the argument of the above mentioned function if the following assignments are made:

$$\tan\alpha = \frac{T_2 - T_3}{T_1 + T_4}, \tag{2.18a}$$

$$\tan\beta = \frac{T_2 + T_3}{T_1 - T_4}. \tag{2.18b}$$

Using the assignments given in Eq. 2.18, we can rewrite Eq. 2.16 as follows:

$$\psi = \frac{1}{2}\tan^{-1}\left\{\tan\left[\tan^{-1}\left(\frac{T_2 - T_3}{T_1 + T_4}\right) - \tan^{-1}\left(\frac{T_2 + T_3}{T_1 - T_4}\right)\right]\right\} \tag{2.19}$$

In the next step, we write the circular co-polarized transmission coefficients in terms of the linear ones by using Eq. 2.12 as follows:

$$T_{++} = T_1 + T_4 + i(T_2 - T_3), \tag{2.20a}$$

$$T_{--} = T_1 - T_4 + i(T_2 + T_3). \tag{2.20b}$$

From Eq. 2.20, it is simple to write the following expressions:

$$\tan\left[\arg\left(T_{++}\right)\right] = \frac{T_2 - T_3}{T_1 + T_4}, \tag{2.21a}$$

$$\tan\left[\arg\left(T_{--}\right)\right] = \frac{T_2 + T_3}{T_1 - T_4}. \tag{2.21b}$$

Finally, by using Eq. 2.21, we can perform a great simplification and rewrite Eq. 2.19 as follows:

$$\psi = \frac{1}{2}\left[\arg\left(T_{++}\right) - \arg\left(T_{--}\right)\right]. \tag{2.22}$$

Equation 2.22 is the most simplified expression for the degree of the rotation of the polarization plane of an incident wave for a fourfold rotational symmetric chiral metamaterial.

Now, we write the ellipticity of a transmitted wave for a linearly polarized incident wave as follows [16]:

$$\chi = \frac{1}{2}\sin^{-1}\left(\frac{2C_2/C_1\sin\left(\phi_2-\phi_1\right)}{1+C_2^2/C_1^2}\right). \tag{2.23}$$

By using the expressions given in Eqs. 2.13 and 2.15, we can rewrite Eq. 2.23 as follows:

$$\chi = \frac{1}{2}\sin^{-1}\left(2\,\frac{T_4T_1-T_3T_2}{C_1^2+C_2^2}\right). \tag{2.24}$$

After many tedious algebraic steps, which are not shown here for the purpose of preserving the compactness of the proof, it can be shown that

$$\frac{T_4T_1-T_3T_2}{C_1^2+C_2^2} = \frac{1}{2}\sin\left\{2\tan^{-1}\left[\frac{\sqrt{(T_1+T_4)^2+(T_2-T_3)^2}-\sqrt{(T_1-T_4)^2+(T_2+T_3)^2}}{\sqrt{(T_1+T_4)^2+(T_2-T_3)^2}+\sqrt{(T_1-T_4)^2+(T_2+T_3)^2}}\right]\right\}. \tag{2.25}$$

In the next step, we use Eq. 2.20 to write

$$|T_{++}| = \sqrt{(T_1+T_4)^2+(T_2-T_3)^2}, \tag{2.26a}$$

$$|T_{--}| = \sqrt{(T_1-T_4)^2+(T_2+T_3)^2}. \tag{2.26b}$$

By combining Eqs. 2.24, 2.25, and 2.26, we write the most simplified expression for ellipticity in terms of the co-polarized circular transmission coefficients as follows:

$$\chi = \tan^{-1}\left(\frac{|T_{++}|-|T_{--}|}{|T_{++}|+|T_{--}|}\right). \tag{2.27}$$

2.4 Linear to Circular Polarization Conversion

In this section, we demonstrate the design and characterization of a circular polarizer, which is a chiral metamaterial based fourfold rotational asymmetric structure that consists of linear and isotropic materials. This section is adapted from Ref. [17]. The proposed geometry here, which is depicted in Fig. 2.1, leads to the transmission of LCP and RCP waves for an x-polarized normally incident wave at different resonance frequencies. From an engineering point of view, the generation of circularly polarized waves can be important for antenna [18–20] and laser applications [21,22], remote sensors, and liquid crystal displays [23,24]. The proposed design is similar to those studied in Refs. [4, 25]; however, it is distinguished from them in that the sizes of all the split ring resonator (SRR) pairs are not the same. Specifically, we decreased the sizes of the electrically excited SRRs at the front side and therefore, the other element of the pair that is located at the back side. With the aid of this size reduction, we drive some of the SRR pairs in the resonance state and some of them in the off-resonance state.

2.4.1 Theoretical Background

The resonance frequency difference between the pairs with different dimensions enables the possibility of optimizing the transmission coefficients T_{xx} and T_{yx} such that the following two conditions are satisfied at the two lowest resonance frequencies:

$$|T_{xx}| = |T_{yx}|, \tag{2.28a}$$

$$\arg(T_{xx}) - \arg(T_{yx}) = \pm\pi/2. \tag{2.28b}$$

Note that the conditions given in Eq. 2.28 imply the conversion of an x-polarized incident wave to an RCP or LCP wave upon transmission depending on the sign of $\pi/2$ (+ or −) in Eq. 2.28(b).

We do not care about the transmission characteristics of the structure for a y-polarized incident wave, since the simultaneous satisfaction of the circular

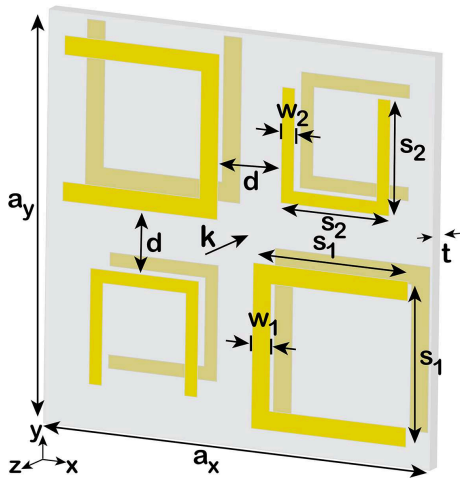

Figure 2.1: The unit cell of the proposed asymmetric chiral metamaterial based circular polarizer. The geometric parameters of the structure are given by $a_x = a_y = 15$ mm, $s_1 = 6$ mm, $s_2 = 4.2$ mm, $w_1 = 0.7$ mm, $w_2 = 0.5$ mm, $d = 2.6$ mm, and $t = 1.5$ mm. Reprinted with permission from [17]. Copyright 2011 by the Optical Society of America.

polarization conversion conditions for both x- and y-polarized incident waves is not possible. In Sec. 2.2, we stated that the satisfaction of $T_{yy} = T_{xx}$ and $T_{xy} = -T_{yx}$ is guaranteed for fourfold rotational symmetric chiral materials. While the former condition is enforced by Lorentz reciprocity [15], the latter is only enforced by the symmetry. Therefore, for fourfold rotational asymmetric chiral metamaterials, we have $T_{xy} \neq -T_{yx}$ in the general case. It will be evident in the next chapter that the obtaining of $T_{xy} \neq -T_{yx}$ gives rise to a phenomenon called *asymmetric transmission*. Furthermore, $T_{xy} \neq -T_{yx}$ implies that the cross-polarized circular transmission coefficients are nonzero.

After noting that $T_{+-} \neq 0$ and $T_{-+} \neq 0$ for fourfold asymmetric chiral structures, we realize that the eigenstates for such a structure are not circularly but elliptically polarized waves. This eigenstate combination is a peculiarity of such asymmetric structures and is the primary reason for the operation of the proposed design in this section. For instance, let us assume a structure with fourfold rotational symmetry and the eigenstates of this geometry are given by

$$i_1 = \frac{1}{\sqrt{2}} \begin{pmatrix} 1 \\ +i \end{pmatrix}, \quad i_2 = \frac{1}{\sqrt{2}} \begin{pmatrix} 1 \\ -i \end{pmatrix}. \tag{2.29}$$

An x-polarized incident wave can be expressed in terms of these eigenstates as follows:

$$\begin{pmatrix}1\\0\end{pmatrix} = \frac{1}{2}\begin{pmatrix}1\\+i\end{pmatrix} + \frac{1}{2}\begin{pmatrix}1\\-i\end{pmatrix} = \frac{1}{\sqrt{2}}i_1 + \frac{1}{\sqrt{2}}i_2. \tag{2.30}$$

Now, let us assume that the complex transmission coefficients for i_1 and i_2 are given as T_1 and T_2, respectively. Briefly, these transmission coefficients denote the relationship between the incident and transmitted circularly polarized (RCP and LCP) waves. Accordingly, the following equation needs to be satisfied for enabling the transmission of either an RCP or an LCP wave when the incident field is x-polarized:

$$\frac{1}{2}\begin{pmatrix}1\\\pm i\end{pmatrix} = \frac{1}{\sqrt{2}}T_1 i_1 + \frac{1}{\sqrt{2}}T_2 i_2. \tag{2.31}$$

Obviously, Eq. 2.31 is satisfied when $T_1 = 1$ and $T_2 = 0$, or $T_1 = 0$ and $T_2 = 1$. In other words, one of the circularly polarized components must be completely blocked, while the other one is completely transmitted. One can anticipate that it might be very difficult to create such a high transmission difference between the eigenstates.

Now, let us turn our attention to the asymmetric geometry where the eigenstates are elliptically polarized. For such a geometry, we can write the normalized eigenstates as follows:

$$i_1 = \frac{1}{m}\begin{pmatrix}1\\+\alpha e^{i\phi}\end{pmatrix}, \quad i_2 = \frac{1}{m}\begin{pmatrix}1\\-\alpha e^{i\phi}\end{pmatrix}, \tag{2.32}$$

where m is the normalization factor. An x-polarized wave can be expressed in terms of these eigenstates as follows:

$$\begin{pmatrix}1\\0\end{pmatrix} = \frac{1}{2}\begin{pmatrix}1\\+\alpha e^{i\phi}\end{pmatrix} + \frac{1}{2}\begin{pmatrix}1\\-\alpha e^{i\phi}\end{pmatrix} = \frac{m}{2}i_1 + \frac{m}{2}i_2. \tag{2.33}$$

Now, let us define T_1 and T_2 such that they denote the transmission coefficients for the eigenstates i_1 and i_2, respectively. The transmission of a circularly polarized wave for an x-polarized incidence implies the satisfaction of the following

equation:

$$\frac{1}{2}\begin{pmatrix}1\\ \pm i\end{pmatrix} = \frac{m}{2}T_1 i_1 + \frac{m}{2}T_2 i_2. \tag{2.34}$$

One can solve Eq. 2.34 for T_1 and T_2 to obtain the following:

$$T_1 = \frac{1}{2} + \frac{1}{2\alpha}\exp\left[-i(\phi \mp \frac{\pi}{2})\right], \tag{2.35a}$$

$$T_2 = \frac{1}{2} - \frac{1}{2\alpha}\exp\left[-i(\phi \mp \frac{\pi}{2})\right]. \tag{2.35b}$$

According to Eq. 2.35, the difference between the transmission coefficients of the eigenstates is given by

$$T_1 - T_2 = \frac{1}{\alpha}\exp\left[-i(\phi \mp \frac{\pi}{2})\right]. \tag{2.36}$$

Basically, Eq. 2.36 states that if $\alpha < 1$, conversion from x-polarization to circular polarization is not possible since we always have $T_1 \leq 1$ and $T_2 \leq 1$. However, if $\alpha > 1$, we see that $|T_1 - T_2| < 1$. For sufficiently large values of α, $|T_1 - T_2|$ becomes sufficiently small and the required value given in Eq. 2.36 can be achievable. To summarize, decreasing the required value of $|T_1 - T_2|$ by means of breaking the fourfold rotational symmetry and therefore, obtaining elliptically polarized eigenstates is the key achievement in designing a circular polarizer that transmits a circularly polarized wave when the incident wave is x-polarized.

2.4.2 Method

The geometry of the proposed chiral metamaterial is depicted in Fig. 2.1 and the geometrical parameters are provided in the caption of this figure. The unit cell consists of four double-layered U-shaped SRRs placed on both sides of the substrate. The SRRs on each side of the substrate are rotated by 90° with respect to each other. Each SRR forms a pair with the SRR on the other side of the substrate and each pair is composed of SRRs that are rotated by 90° with respect to their neighbors. As the substrate, we use a FR-4 board with a relative permittivity of 4 and a loss tangent of 0.025. Copper that is 30 μm thick is used

for structuring the metallic regions.

We start the analysis with numerical simulations of the proposed geometry by using CST Microwave Studio (Computer Simulation Technology AG, Germany), which is a commercial software program that is based on the finite integration method. In the simulations, we use the *periodic* boundary condition along the x- and y-axes. Boundary condition along the z-axis is set to *open* for the purpose of avoiding reflection from the ends of the simulation domain. The structure is illuminated by a plane wave that propagates in the $-z$ direction and the electric field vector of the incident wave is along the x-axis. At the resonance frequencies, 5.1 and 6.4 GHz, the electrical thickness of the structure, t/λ, is given by 0.024 and 0.03, respectively. The lateral periodicity of the structure is equal to 0.255λ at 5.1 GHz and 0.32λ at 6.4 GHz.

For the experimental analysis, we fabricated the structure with the dimension of 15 by 15 unit cells. The experiment is conducted using two standard gain horn antennas facing each other at a 50 cm distance. The structure is placed in the middle between the antennas. The antennas are aligned such that the directions of their main lobe maxima are orthogonal to the material plane. The transmission coefficient measurements are conducted by using an HP-8510C network analyzer. In order to characterize the transmission of the structure numerically and experimentally, the x and y components of the transmitted field are studied and the transmission coefficients T_{xx} and T_{yx} are evaluated.

2.4.3 Results and Discussion

In order to check the existence of any regimes where the circular polarization conversion conditions given in Eq. 2.28 are satisfied, we plot the numerical and experimental values of $|T_{yx}|/|T_{xx}|$ in Fig. 2.2(a), and the numerical and experimental values of the phase difference of the transmission coefficients, $\arg(T_{yx}) - \arg(T_{xx})$ in Fig. 2.2(b). The local maxima in Fig. 2.2(a) correspond to the frequencies where the magnetoelectric coupling between the front and back layers is maximal. Thanks to the existence of this strong coupling, large T_{yx} can be achieved.

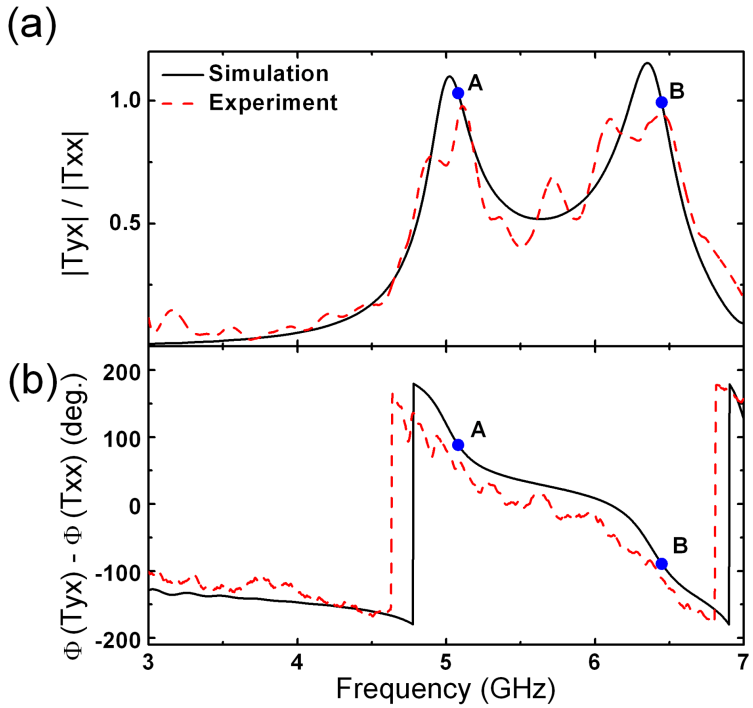

Figure 2.2: (a) Ratio of the magnitudes of T_{yx} and T_{xx}, and (b) phase difference between T_{yx} and T_{xx}. Reprinted with permission from [17]. Copyright 2011 by the Optical Society of America.

According to the numerical results given in Fig. 2.2, $|T_{yx}|/|T_{xx}|$ ratio is given by 1.03 at 5.1 GHz (point A) and 0.994 at 6.4 GHz (point B). By using the numerical results given in Fig. 2.2(b), we find that $\arg(T_{yx}) - \arg(T_{xx})$ is given by 89.8° and −89.2° at points A and B, respectively. The results imply the transmission of LCP and RCP waves at 5.1 and 6.4 GHz, respectively, when the incident plane wave is x-polarized. It is noteworthy that the experimental results agree closely with the numerical ones and therefore, the numerical results that suggest the existence of the circular polarizer regime are verified by means of experimental results.

We stated that $T_{xy} \neq T_{yx}$ due to the broken fourfold rotational symmetry. Consequently, for the proposed design, we have $T_{-+} \neq 0$ and $T_{+-} \neq 0$, see Eq. 2.9. Therefore, all four circular transmission coefficients, T_{++}, T_{-+}, T_{+-}, and T_{--}, are required in order to determine the response of the structure to an arbitrarily polarized incident wave. However, we anticipate that the structure would only

act as a circular polarizer for x-polarized normally incident waves. Therefore, we can safely assume $E_y^i = 0$ and, under this assumption, the significance of T_{xy} and T_{yy} obviously vanishes. At this point, we can define circular transformation coefficients C_+ and C_- for RCP and LCP waves, respectively. C_+ and C_- are newly defined parameter that account for the amplitudes and phases of the RCP and LCP components of a transmitted wave at the exit interface when the incident wave is x-polarized. Accordingly, the circular transformation coefficients can simply be calculated by [4]

$$C_\pm = \frac{1}{2}(T_{xx} \mp iT_{yx}). \tag{2.37}$$

It is very important to note that the coefficients calculated by Eq. 2.37 are only valid when the incident wave is x-polarized. As a consequence of the broken rotational symmetry, one should expect to obtain different transformation coefficients for different polarization plane angles of the incident wave. For instance, the circular transformation coefficients for a y-polarized incident wave can be calculated by using Eq. 2.9 as follows:

$$C_\pm = \frac{1}{2}(T_{yy} \pm iT_{xy}). \tag{2.38}$$

The numerically and experimentally obtained circular transformation spectra are given in Fig. 2.3. As stated before, these parameters symbolize the magnitudes and phases of the RCP and LCP components of the transmitted wave under the assumption that the incident field is x-polarized. It is noteworthy that, in Fig. 2.3, 0 dB is assumed to be equal to the amplitude of the electric field of the incident wave. This assumption implies that the maximum value of a transformation coefficient can be -3 dB. The numerical results given in Fig. 2.3(a) suggest that the minimum amplitude of the RCP of component of a transmitted wave is equal to -37 dB and achieved at 5.1 GHz. Similarly, minimum amplitude of the LCP component is given as -43 dB at 6.4 GHz. It can be seen that the presented experimental results in Fig. 2.3 agree remarkably well with the numerical ones.

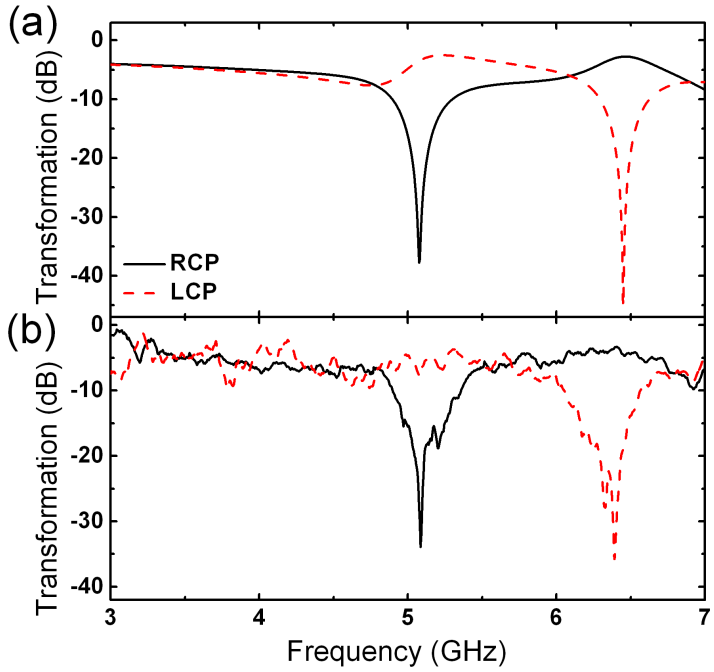

Figure 2.3: (a) Numerical and (b) experimental results for the circular transformation coefficients. Reprinted with permission from [17]. Copyright 2011 by the Optical Society of America.

The presented circular transformation spectra implies that the circular polarizer feature is achieved as a result of the significant differences between $|C_+|$ and $|C_-|$. For instance, at 5.1 GHz, the RCP component of the x-polarized incident wave is almost completely blocked by the structure while the LCP component is transmitted with an approximately unity transmission coefficient. A similar statement can be made for the behavior of the structure at 6.4 GHz. At this frequency, the LCP component of the incident wave is blocked and therefore, the transmitted wave is RCP.

In order to understand the effect of the introduced rotational asymmetry, we simulated the geometry where the dimensions of all the SRRs are given by s_1 and w_1. Note that, in this case, d is reduced to 1.5 mm since the periodicity of the unit cell is kept constant. For this structure, on the one hand, we observe that $|T_{xx}|$ is approximately -20 dB near the resonance frequencies. On the other hand, we see that $|T_{yx}|$ is approximately -6 dB. This observation implies that, for the fourfold rotational symmetric geometry, the value of $||C_+| - |C_-||$ is smaller than

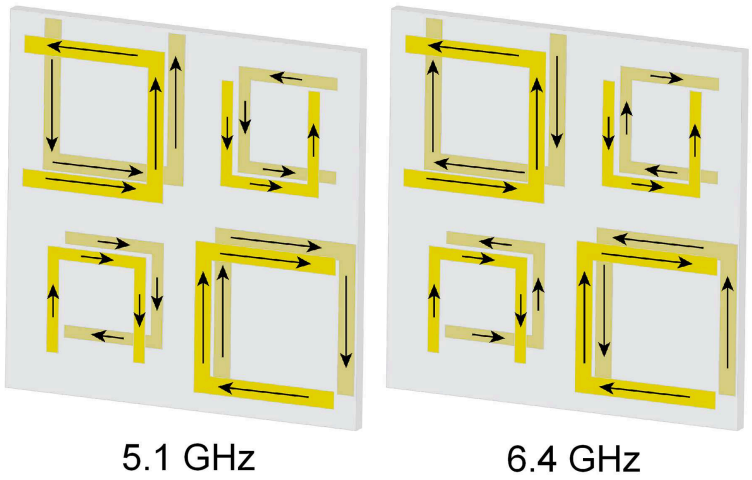

Figure 2.4: Directions of the surface currents on the SRRs, which are induced as a result of the coupling of the incident x-polarized wave to the SRRs, at 5.1 and 6.4 GHz. Reprinted with permission from [17]. Copyright 2011 by the Optical Society of America.

unity due to the fact that $|T_{xx}|$ and $|T_{yx}|$ cannot be equalized at the resonance frequencies. For the proposed asymmetric design, we see that $|T_{xx}|$ is increased to approximately -6.5 dB at the resonance frequencies with the aid of the decreased coupling of the incident light to the electrically excited SRRs, which is achieved by driving such SRRs in the off-resonance condition by decreasing their sizes.

For the purpose of understanding the physical nature of the resonances, we investigated the induced surface current distributions numerically at 5.1 and 6.4 GHz. The directions of the induced surface currents are shown in Fig. 2.4 by the arrows. Smaller arrows shown on the smaller SRRs indicate that the amplitude of the surface current is much smaller than that on the larger SRRs. In fact, this amplitude difference is well-anticipated since the smaller SRRs are driven in the off-resonance condition meaning that the coupling of the incident light to such SRRs is much weaker than the coupling to the larger ones. By means of driving the smaller SRRs in the off-resonance condition, we can decrease the coupling of the incident light to such SRRs and therefore, achieve a larger $|T_{xx}|$ at the resonance frequencies, which allows the equalization of $|T_{xx}|$ and $|T_{yx}|$ with a phase difference of $\pm\pi/2$. Furthermore, for mutually rotated SRR pairs, we know that the resonance levels are determined in line with the longitudinal magnetic to

magnetic dipole coupling [8]. The results shown in Fig. 2.4 reveal that the surface currents induced at the lower resonance frequency are in the same direction, which in turn results in parallel magnetic dipole moments for the pairs. At the higher resonance, we observe that the induced currents are in opposite directions and that conduces to antiparallel magnetic dipole moments.

We stated that we do not expect the proposed structure to operate as a circular polarizer for y-polarized incident waves since the rotational fourfold symmetry is broken and as a consequence, we obtain $T_{xy} \neq T_{yx}$, see Eqs. 2.37 and 2.38. In order to verify this intuition, we illuminated the structure with normally incident y-polarized waves. We observe that, at 5.1 GHz, $|T_{xy}|/|T_{yy}| = 0.44$ and $\arg(T_{xy}) - \arg(T_{yy}) = 105°$. These transmission coefficients imply the transmission of an elliptically polarized waves. At 6.4 GHz, we obtain $|T_{xy}|/|T_{yy}| = 0.39$ and $\arg(T_{xy}) - \arg(T_{yy}) = 5°$. Accordingly, we conclude that the proposed geometry does not operate as a circular polarizer for y-polarized incident waves.

2.5 Polarization Independent Cross-Polarization Conversion

In this section, we demonstrate the theoretical background, design, and characterization of a chiral metamaterial based 90° polarization rotator. This section is adapted from Ref. [26]. In designing an incident polarization angle insensitive cross-polarization converter, which also exhibits unity transmission and conversion efficiency, we benefit from the optical activity, which is provided by chirality, and the electromagnetic tunneling effect. A polarization rotator is known to rotate the polarization plane of an arbitrarily linearly polarized electromagnetic wave by a fixed angle without changing the ellipticity of the wave. Note that the ellipticity parameter is equal to 0° for linearly polarized waves. Traditional polarization rotators benefit from dextrorotatory and levorotatory crystals, the Faraday effect, anisotropic media, and twisted nematic liquid crystals [16]. However, the devices obtained by benefiting from these features are generally in a

thickness range that is comparable to the operation wavelength, which is a significant drawback for especially low frequency applications. The utilization of chiral metamaterials is a promising method to avoid the thickness problem. However, such structures can have their own drawbacks such as interference effects between the incident and reflected waves [27] and polarization sensitive response [6,28,29]. In the literature, several intelligently designed chiral structures have been proposed in order to overcome these problems [10,25,30,31]. However, these designs are not *transparent* to the incident fields, meaning that the transmission coefficient is not equal to unity.

Here, we demonstrate a three-layer chiral metamaterial, which has a thickness that is much smaller than the operation wavelength, and this structure rotates the polarization plane of incident linearly polarized waves by 90° irrespective of the incident polarization plane angle. The governing mechanism for the achievement of unity transmission efficiency is the electromagnetic tunneling phenomenon [32], which will be described in detail in the next subsection. The achievement of unity transmission by benefiting from this intriguing effect has been demonstrated for various configurations in the literature [29,33–35].

2.5.1 Electromagnetic Tunneling

The phenomenon of electromagnetic tunneling is governed by the findings of effective medium theory. Firstly, let us take a homogeneous layer B with a thickness of d_2 and a permittivity of $\epsilon_2 < 0$. This ϵ_2 setting allows only evanescent waves inside medium B. Now, let us take another homogeneous medium A with a thickness of d_1 and a permittivity of $\epsilon_1 > 0$. Assume that medium A is lossless. Next, let us consider the possibility of achieving *unity* transmission through the AB stacked composite geometry. Transfer matrix theory [36] is a great tool here, which is much simpler than the iterative approach given in Ref. [37]. We can

write the transfer matrix of medium A as follows:

$$T_1 = \begin{pmatrix} \cos(k_1 d_1) & -i\sin(k_1 d_1)\dfrac{w}{ck_1} \\ -i\sin(k_1 d_1)\dfrac{ck_1}{w} & \cos(k_1 d_1) \end{pmatrix}, \tag{2.39}$$

where k_1 is the wavenumber inside A and $k_1 = \sqrt{\epsilon_1}w/c$. In a similar fashion, the transfer matrix of medium B can be written as

$$T_2 = \begin{pmatrix} \cos(k_2 d_2) & -i\sin(k_2 d_2)\dfrac{w}{ck_2} \\ -i\sin(k_2 d_2)\dfrac{ck_2}{w} & \cos(k_2 d_2) \end{pmatrix}, \tag{2.40}$$

where $k_2 = \sqrt{\epsilon_2}w/c$. It is obvious that $\sqrt{\epsilon_2}$ is purely imaginary due to that fact that $\epsilon_2 < 0$ and therefore, k_2 is also purely imaginary. This fact does not modify the calculations and let us forget it until the end of the calculation. The overall transfer matrix of the stratified medium can be evaluated as $T = T_1 T_2$. When we do this matrix multiplication, we find the elements of T as follows:

$$T(1,1) = \cos(k_1 d_1)\cos(k_2 d_2) - \frac{k_2}{k_1}\sin(k_1 d_1)\sin(k_2 d_2), \tag{2.41a}$$

$$T(1,2) = -i\frac{w}{ck_1}\sin(k_1 d_1)\cos(k_2 d_2) - i\frac{w}{ck_2}\cos(k_1 d_1)\sin(k_2 d_2), \tag{2.41b}$$

$$T(2,1) = -i\frac{ck_1}{w}\sin(k_1 d_1)\cos(k_2 d_2) - i\frac{ck_2}{w}\cos(k_1 d_1)\sin(k_2 d_2), \tag{2.41c}$$

$$T(2,2) = \cos(k_1 d_1)\cos(k_2 d_2) - \frac{k_1}{k_2}\sin(k_1 d_1)\sin(k_2 d_2), \tag{2.41d}$$

where $T(i,j)$ denotes the element of the transfer matrix that is at the i^{th} row and the j^{th} column. Assuming that the composite medium AB is suspended in free-space, the reflection coefficient, r, and the transmission coefficient, t, can be calculated by solving the following matrix equation:

$$\begin{pmatrix} 1 \\ r \end{pmatrix} = \begin{pmatrix} 1 & 1 \\ -1 & 1 \end{pmatrix}^{-1} T^{-1} \begin{pmatrix} 1 & 1 \\ -1 & 1 \end{pmatrix} \begin{pmatrix} t \\ 0 \end{pmatrix}. \tag{2.42}$$

When the matrix inversion operations are performed, we arrive to the following equation:

$$\begin{pmatrix}1\\ r\end{pmatrix} = \frac{1}{2\det(T)}\begin{pmatrix}1 & -1\\ 1 & 1\end{pmatrix}\begin{pmatrix}T(2,2) & -T(1,2)\\ -T(2,1) & T(1,1)\end{pmatrix}\begin{pmatrix}1 & 1\\ -1 & 1\end{pmatrix}\begin{pmatrix}t\\ 0\end{pmatrix}. \tag{2.43}$$

It has been stated that we are looking into the possibility of the achievement of unity transmission by the utilization of the AB structure. Therefore, in Eq. 2.43, we set $r = 0$ and $t = 1$. After performing the matrix multiplication operations, the following equation is obtained:

$$\begin{pmatrix}1\\ 0\end{pmatrix} = \frac{1}{2\det(T)}\begin{pmatrix}T(1,1)+T(1,2)+T(2,1)+T(2,2)\\ -T(1,1)+T(1,2)-T(2,1)+T(2,2)\end{pmatrix}. \tag{2.44}$$

Equation 2.44 consists of two independent equations. We only consider the one that is relevant to the reflection coefficient, r, and write it as follows:

$$-T(1,1)+T(1,2)-T(2,1)+T(2,2) = 0. \tag{2.45}$$

After substituting the corresponding elements in Eq. 2.41 into Eq. 2.45, and rearranging and simplifying the terms, we obtain

$$\left(\frac{k_1}{k_0}-\frac{k_0}{k_1}\right)\tan(k_1d_1)+\left(\frac{k_2}{k_0}-\frac{k_0}{k_2}\right)\tan(k_2d_2) - i\left(\frac{k_2}{k_1}-\frac{k_1}{k_2}\right)\tan(k_1d_1)\tan(k_2d_2) = 0. \tag{2.46}$$

Now, we can remember that k_2 is purely imaginary. A real number α_2 can be defined such that $k_2 = i\alpha_2$. After replacing k_2 with $i\alpha_2$ and recalling that $\tan(ix) = i\tanh(x)$, the following condition for the achievement of unity transmission is obtained:

$$\left(\frac{k_1}{k_0}-\frac{k_0}{k_1}\right)\tan(k_1d_1)-\left(\frac{\alpha_2}{k_0}+\frac{k_0}{\alpha_2}\right)\tanh(\alpha_2d_2) + i\left(\frac{\alpha_2}{k_1}+\frac{k_1}{\alpha_2}\right)\tan(k_1d_1)\tanh(\alpha_2d_2) = 0. \tag{2.47}$$

It is noteworthy that Eq. 2.47 consists of two real terms and one imaginary term. The real terms can cancel each other if the parameters d_1 and d_2 are properly selected. However, the imaginary term can never be equalized to zero. Therefore, unity transmission cannot be achieved by using the AB structure. The reason is that the waves reflected from the interface between A and B cannot cancel each other as a consequence of the fact that A and B are in different phase planes.

We proved that unity transmission is not achievable in the AB structure. Now, let us consider the ABA structure and derive the corresponding unity transmission condition. This time, the overall transfer matrix T is given by $T = T_1T_2T_1$. We directly write the resulting elements of T without going into the details of the tedious algebraic steps. At the end, $T(1,1)$ is given by

$$T(1,1) = \cos(2k_1d_1)\cos(k_2d_2) - \frac{1}{2}\sin(2k_1d_1)\sin(k_2d_2)\left(\frac{k_2}{k_1} + \frac{k_1}{k_2}\right). \tag{2.48}$$

$T(1,2)$ can be expressed as

$$T(1,2) = -i\frac{w}{ck_1}\sin(2k_1d_1)\cos(k_2d_2) + i\frac{wk_2}{ck_1^2}\sin^2(k_1d_1)\sin(k_2d_2) - i\frac{w}{ck_2}\cos^2(k_1d_1)\sin(k_2d_2). \tag{2.49}$$

Similarly, one can find that $T(2,1)$ is given by

$$T(2,1) = -i\frac{ck_1}{w}\sin(2k_1d_1)\cos(k_2d_2) + i\frac{ck_1^2}{wk_2}\sin^2(k_1d_1)\sin(k_2d_2) - i\frac{ck_2}{w}\cos^2(k_1d_1)\sin(k_2d_2). \tag{2.50}$$

Finally, $T(2,2)$ can be written as follows:

$$T(2,2) = \cos(2k_1d_1)\cos(k_2d_2) - \frac{1}{2}\sin(2k_1d_1)\sin(k_2d_2)\left(\frac{k_2}{k_1} + \frac{k_1}{k_2}\right). \tag{2.51}$$

The condition for unity transmission through the ABA structure can be written

with the aid of Eq. 2.45 as follows:

$$\left(\frac{k_1}{k_0}-\frac{k_0}{k_1}\right)2\tan(k_1d_1)+\left(\frac{k_2}{k_0}-\frac{k_0}{k_2}\right)\tan(k_2d_2) + \left(\frac{k_0k_2}{k_1^2}-\frac{k_1^2}{k_0k_2}\right)\tan^2(k_1d_1)\tan(k_2d_2)=0. \quad (2.52)$$

In the final step, we replace k_2 with $i\alpha_2$ and Eq. 2.52 becomes

$$\left(\frac{k_1}{k_0}-\frac{k_0}{k_1}\right)2\tan(k_1d_1)-\left(\frac{\alpha_2}{k_0}+\frac{k_0}{\alpha_2}\right)\tanh(\alpha_2d_2) - \left(\frac{k_0\alpha_2}{k_1^2}+\frac{k_1^2}{k_0\alpha_2}\right)\tan^2(k_1d_1)\tanh(\alpha_2d_2)=0. \quad (2.53)$$

Interestingly, all the terms in Eq. 2.53 are purely real and therefore, Eq. 2.53 can be satisfied by the proper selection of d_1 and d_2. The achievement of unity transmission through an ABA system, where B is normally opaque, is called *electromagnetic tunneling*. It is also noteworthy that the electromagnetic tunneling effect is not based on a resonance. It is a very interesting phenomenon where B does not allow propagating waves, but a unity transmission can be achieved with the aid of enhanced magnetic fields at the A/B interfaces; see Ref. [32] for the magnetic field distribution inside the ABA structure.

2.5.2 Theoretical Background

In order to determine the fundamental design methodology for the achievement of a polarization insensitive 90° polarization rotator, we first evaluate the required transmission matrix. First of all, we assume that the incident wave is linearly polarized with a polarization plane angle of θ, where θ is defined with respect to the x-axis. Using Jones calculus, one can relate the incident and transmitted fields for the desired structure by using the following equation:

$$\begin{pmatrix}\cos(\theta+\pi/2)\\ \sin(\theta+\pi/2)\end{pmatrix}=\begin{pmatrix}T_{xx} & T_{xy}\\ T_{yx} & T_{yy}\end{pmatrix}\begin{pmatrix}\cos(\theta)\\ \sin(\theta)\end{pmatrix}. \quad (2.54)$$

By using simple trigonometric identities, Eq. 2.54 can be rewritten as follows:

$$\begin{pmatrix} -\sin(\theta) \\ \cos(\theta) \end{pmatrix} = \begin{pmatrix} T_{xx} & T_{xy} \\ T_{yx} & T_{yy} \end{pmatrix} \begin{pmatrix} \cos(\theta) \\ \sin(\theta) \end{pmatrix}. \tag{2.55}$$

The solution of Eq. 2.55 yields $T_{xx} = 0$, $T_{xy} = -1$, $T_{yx} = 1$, and $T_{yy} = 0$. It is obvious that the realization of a strong optical activity is required in order to obtain the desired operation regime. Therefore, we envision that the utilization of a chiral metamaterial is required for the purpose of achieving strong optical activity in a compact performance. Next, we calculate the eigenvalues of the desired transmission matrix by using the following equation [15]:

$$\kappa_{1,2} = \frac{1}{2}\left[(T_{xx} + T_{yy}) \pm \sqrt{(T_{xx} - T_{yy})^2 + 4T_{xy}T_{yx}}\right]. \tag{2.56}$$

By substituting the corresponding elements of the desired transmission matrix, we obtain $\kappa_{1,2} = \pm i$. Using these eigenvalues, we can write the normalized eigenbasis matrix as follows:

$$\hat{\Lambda} = \frac{1}{\sqrt{2}} \begin{pmatrix} 1 & 1 \\ +i & -i \end{pmatrix}. \tag{2.57}$$

It immediately follows that the egienbasis matrix given in Eq. 2.57 corresponds to the following normalized eigenstates:

$$i_1 = \frac{1}{\sqrt{2}} \begin{pmatrix} 1 \\ +i \end{pmatrix}, \quad i_2 = \frac{1}{\sqrt{2}} \begin{pmatrix} 1 \\ -i \end{pmatrix}. \tag{2.58}$$

Equation 2.58 states that a geometry with counter-rotating circularly polarized eigenstates is required in order to achieve the desired polarization rotation characteristics. By using Eq. 2.9, we can transform the linear transmission matrix to the circular one and the resultant transmission matrix is given by

$$T_{circ} = \begin{pmatrix} T_{++} & T_{+-} \\ T_{-+} & T_{--} \end{pmatrix} = \begin{pmatrix} -i & 0 \\ 0 & +i \end{pmatrix}. \tag{2.59}$$

In Eq. 2.59, the cross-polarized circular transmission coefficients, T_{-+} and T_{+-}, are equal to zero. As we have stated in Sec. 2.2, this necessitates the utilization of

a *fourfold rotational symmetric* structure. Therefore, we know that the designed structure must satisfy this symmetry requirement. Furthermore, $T_{++} = -i$ and $T_{--} = +i$ implies that, upon propagation, the structure should advance the phase of RCP waves by 90° while lagging the phase of LCP waves by 90°. Finally, $|T_{++}| = |T_{--}| = 1$ means the transmission of the circularly polarized eigenstates with a unity transmission coefficient. This shows that the electromagnetic tunneling effect should be a counterpart of the proposed geometry.

2.5.3 Method

In the proposed design, an ABA stacking scheme is realized for the purpose of obtaining the electromagnetic tunneling regime described in Sec. 2.5.1. Note that a fourfold rotational symmetric A layer exhibits the same permittivity for RCP and LCP waves and therefore, can be characterized by using a single parameter. For layer A, we use four rotated SRR geometry proposed in Ref. [4]. It is not mandatory to use this structure; one can design a different symmetric geometry that satisfies the effective permittivity requirement for the electromagnetic tunneling. Layer B should exhibit a negative effective permittivity in order to achieve the tunneling effect. Therefore, we select B as a subwavelength mesh. For the formation of the composite geometry, the mesh is placed between the two layers and we do not leave any air gap between the layers. The composite geometry and the stacking scheme, the photograph of A, and the photograph of B are shown in Figs. 2.5(a)–2.5(c), respectively. As the substrates, we use two teflon layers with a thickness of 1.2 mm, a relative dielectric constant of 2.1, and a loss tangent of 2×10^{-4}. For the metallic regions, we use copper that is 20 μm thick. Layer A is printed on the teflon substrate and its total thickness is equal to 1.22 mm. For experimental purposes, on the one hand, layer B is printed on the back side of one of the A layers. On the other hand, layer B is considered to be a stand-alone structure with a thickness of 20 μm in the theoretical consideration. As it will be evident in the next section, the operation frequency of the structure is 7 GHz. Correspondingly, the electrical thickness of the composite structure is given by $\lambda/21$. This electrical thickness shows that a giant optical activity can be achieved

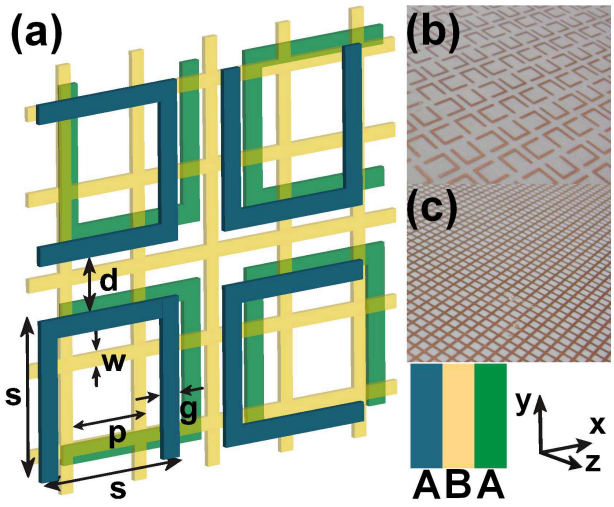

Figure 2.5: (a) Visual representation of the three-layer structure without teflon substrates. The color of each layer is different and the stacking scheme with respect to the colors is presented on the bottom-right corner. Photographs of the experimental sample for (b) layer A and (c) layer B. For layer A, the geometrical parameters are given by $s = 6$ mm, $g = 0.7$ mm, and $d = 2$ mm. For layer B, the geometrical parameters are given by $w = 0.5$ mm and $p = 3.2$ mm. These parameters imply that the lateral periodicity is equal to 16 mm in both x and y directions. Reprinted with permission from [26]. Copyright 2012, American Institute of Physics.

in an ultrathin and compact structure. Furthermore, the lateral periodicity of the structure is equal to 0.37λ, which implies the obtaining of diffraction-free reflection and transmission regimes.

We start the numerical analysis of the proposed structure by running simulations using CST Microwave Studio, which is a commercially available simulation software program that is based on the finite integration method. Periodic boundary condition is applied along the x- and y-axes while open boundary condition is selected for the z-axis. Normally incident plane waves propagating in the $+z$ direction are utilized for exciting the structure. For the purposes of experimental characterization, we fabricate the structure with a dimension of 18 by 18 unit cells. The transmission coefficients are measured with the aid of two standard gain horn antennas; one being the transmitter and the other one being the receiver. Measurements are performed by using an Anritsu 37369A network analyzer.

2.5.4 Results and Discussion

We provide the numerical and experimental linear transmission coefficients in Figs. 2.6(a) and 2.6(b), respectively.. As a result of the fourfold rotational symmetry, we automatically obtain $T_{yy} = T_{xx}$ and $T_{xy} = -T_{yx}$ as stated in Sec. 2.2. Therefore, we discuss here only T_{xx} and T_{yx} in order to simplify the discussion without loss of generality. Numerical linear transmission coefficients shown in Fig. 2.6(a) show that there are two dips for $|T_{xx}|$. On the one hand, at the lower frequency dip at 7 GHz, we observe that $|T_{xx}| = -42$ dB. On the other hand, we obtain $|T_{xx}| = -60$ dB at the higher frequency dip at 7.5 GHz. The cross-polarized transmission coefficient is given by -0.04 dB and -17.5 dB at the lower and higher frequency dips, respectively.

In this context, we define the cross-polarization conversion efficiency as the ratio of the difference between the power of the cross- and co-polarized transmitted components, and the total incident power. Mathematically, cross-polarization conversion efficiency can be expressed as follows:

$$C_{\text{eff}} = 100 \, \frac{|T_{yx}|^2 - |T_{xx}|^2}{|E_{\text{inc}}|^2}, \tag{2.60}$$

where E_{inc} denotes the electric field of the incident wave. Accordingly, we calculate that $C_{\text{eff}} = 99\%$ and $C_{\text{eff}} = 2\%$ at 7 and 7.5 GHz, respectively. Experimental linear transmission results shown in Fig. 2.6(b) suggest that $|T_{xx}|$ is given by -31 dB and -32 dB at 7 and 7.5 GHz, respectively. At these frequencies, we observe that $|T_{yx}|$ is equal to -0.3 dB and -21 dB. The utilization of Eq. 2.60 on the experimental results yields a C_{eff} of 93% and 1% at 7 and 7.5 GHz, respectively. Since we target the achievement of maximum power transmission through the structure, the frequency of interest becomes 7 GHz. Due to much larger power transfer compared to 7.5 GHz, we achieve a much larger cross-polarization conversion efficiency at 7 GHz. We envision that the achievement of $|T_{yx}| = -0.04$ dB at 7 GHz is closely related to the enabling of the electromagnetic tunneling at this frequency. We will verify this intuition in the subsequent part by benefiting from the effective medium and transfer matrix theories. Although we obtain

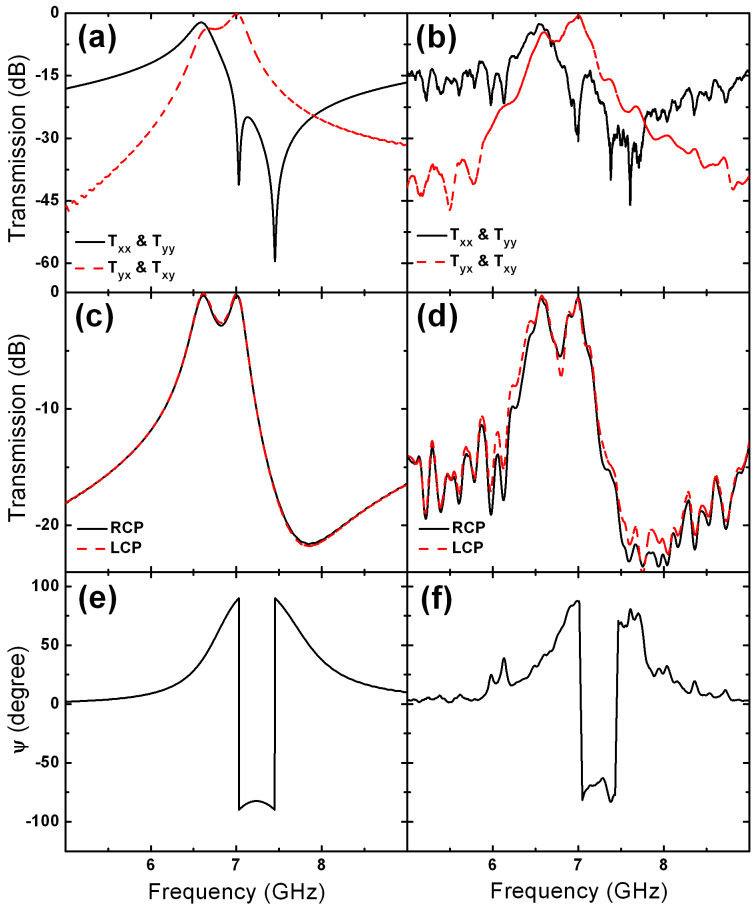

Figure 2.6: (a) Numerical and (b) experimental linear transmission coefficients, and (c) numerical and (d) experimental circular transmission coefficients. Plot (e) and (f) show the numerical and experimental polarization plane rotation angles, respectively. Reprinted with permission from [26]. Copyright 2012, American Institute of Physics.

smaller experimental efficiencies compared to the numerical ones, the experimental results are in good agreement with the numerical ones and therefore, verify the theoretical and numerical predictions.

It has been stated that, under fourfold rotational symmetry assumption, circular transmission coefficients T_{++} and T_{--} can be calculated by using Eq. 2.12. Furthermore, the cross-polarized circular transmission coefficients T_{-+} and T_{+-} are equal to zero. We calculate $|T_{++}|$ and $|T_{--}|$ accordingly and show the corresponding numerical and experimental results in Figs. 2.6(c) and 2.6(d), respectively. Two peaks are observed for the transmission coefficients and their origins

will be investigated subsequently with the aid of the transfer matrix theory. On the one hand, at 7 GHz, we obtain $|T_{++}| = -0.05$ dB and $|T_{--}| = -0.03$ dB from the numerical results. On the other hand, the experimental results suggest that $|T_{++}| = -0.36$ dB and $|T_{--}| = -0.26$ dB at 7 GHz. It is noteworthy that the low loss tangent of the teflon substrate results in small absorption and therefore, $|T_{++}| \simeq |T_{--}|$.

Afterwards, the degree of polarization rotation ψ and the degree of ellipticity χ are calculated by using Eqs. 2.22 and 2.27, respectively. The resultant numerical and experimental spectra of ψ are provided in Figs. 2.6(e) and 2.6(f), respectively. As an implication of the usage of a substrate with a very low loss tangent, the ellipticities of the transmitted waves are approximately equal to 0°. The numerical results suggest that, at 7 GHz, $\psi = 90.1°$ and $\chi = -0.5°$. According to the experimental results, $\psi = 88.9°$ and $\chi = -1.5°$. Therefore, it is both numerically and experimentally verified that the polarization plane angle of the transmitted waves are rotated by 90° and the linearity of the polarization curve is preserved upon transmission.

For the purpose of describing the transmission characteristics of the proposed design theoretically, we employ the effective medium and transfer matrix theories. After simulating individual A and B layers, we retrieve the complex circular transmission coefficients. In the next step, we determine the corresponding effective permittivity and effective thickness of each layer by regenerating the magnitude and phase components of the transmission coefficients by using homogeneous layers. Accordingly, we calculate $\epsilon_{\mathrm{A}}^{\mathrm{eff}} = 1 + 172.7/(7.55^2 - f^2)$ and $\epsilon_{\mathrm{B}}^{\mathrm{eff}} = 1.94 - 47.2^2/f^2$, where f denotes the frequency of the incident wave. Moreover, the effective thicknesses are obtained as $d_{\mathrm{A}}^{\mathrm{eff}} = 1.22$ mm and $d_{\mathrm{B}}^{\mathrm{eff}} = 1.65$ mm. Since the individual A and B layers are achiral, they exhibit the same effective permittivity for RCP and LCP waves. When combined with the lossless substrate assumption, this observation enables us to use the same effective permittivity values for the two circularly polarized eigenstates.

After the retrieval of the effective permittivities and thicknesses, transmission and reflection coefficients for the ABA composite structure can be calculated by

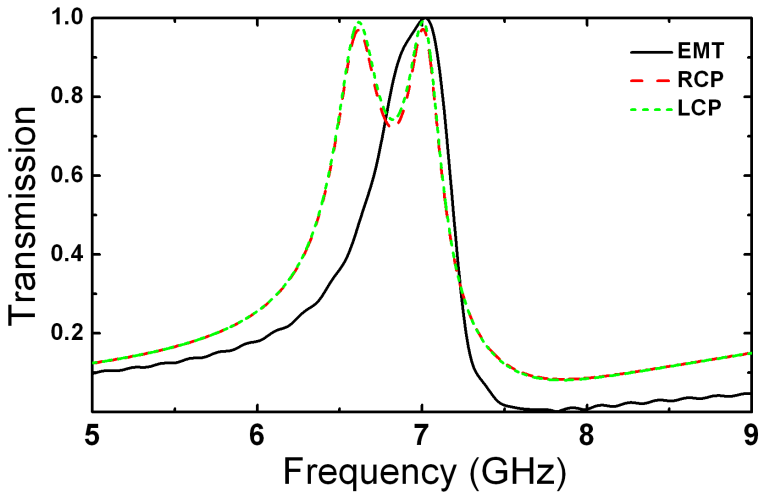

Figure 2.7: Comparison of the numerical circular transmission coefficients with the theoretically predicted transmission coefficient using transfer matrix theory. Reprinted with permission from [26]. Copyright 2012, American Institute of Physics.

reorganizing Eq. 2.43 as follows:

$$t = \frac{2\det(T)}{T(1,1)+T(1,2)+T(2,1)+T(2,2)}, \tag{2.61a}$$

$$r = \frac{t}{2\det(T)}\left[-T(1,1)+T(1,2)-T(2,1)+T(2,2)\right]. \tag{2.61b}$$

Note that $T(1,1)$, $T(1,2)$, $T(2,1)$, and $T(2,2)$ should be directly taken from Eqs. 2.48, 2.49, 2.50, and 2.51, respectively. The spectrum of the magnitude of the calculated transmission coefficient according to Eq. 2.61(a) is shown in Fig. 2.7 along with the numerical $|T_{++}|$ and $|T_{--}|$ spectra. According to Fig. 2.7, the transmission peak at 7 GHz, which is numerically and experimentally verified, is reproduced by the transfer matrix calculations. Therefore, it is verified that this peak is a result of the electromagnetic tunneling effect.

The transmission peak at 7 GHz is not reproduced by the transfer matrix theory, see Fig. 2.7. As a result, we envision that this peak is not relevant to the effective medium description of the composite metamaterial. It should be the result of another mechanism. We predict that this peak is governed by the extraordinary transmission phenomenon [38]. Extraordinary transmission

phenomenon originates from the fact that bound surface modes that lie below the light line can be excited owing to the additional wavevector that is supplied by the periodicity of a surface. In the simulations, we added a very small space, 0.3 mm, between the consecutive A and B layers to see the evolution of the transmission peaks. On the one hand, when this space is added, the peak at 6.5 GHz disappears, which shows that this peak is strongly dependent on the interfaces between the A and B layers. On the other hand, the peak at 7 GHz still conforms the transfer matrix predictions. Therefore, we conclude that the peak at 6.5 GHz is most likely to be an extraordinary transmission relevant transmission peak.

Chapter 3

One-Way Spoof Surface Plasmons and Diodelike Beaming

3.1 Introduction

Surface plasmon (SP) inspired extraordinary transmission (ET) through subwavelength apertures in corrugated metallic slabs has been a subject of extensive study since its first demonstration in 1998 [38]. While classical SPs represent the collective oscillation of a conductor's electron plasma at a conductor/dielectric interface at optical frequencies, their low frequency analogs, spoof or designer SPs, can be obtained even at microwave frequencies by adding corrugations to a metallic slab, or patterning it with subwavelength holes [40, 41]. On the other hand, a wider variety of SP relevant operation regimes can be realized at optical frequencies using structures with corrugations [42]. It is known that corrugations placed around a sole subwavelength hole or slit on the incidence side can yield a dramatic enhancement of transmission due to the excitation of SPs by means of enabling the matching of the wavevector of an incident wave to that of a supported surface mode [43–45]. In turn, *beaming*, i.e., localization of the transmitted beam(s) within desired angular regions of the exit half-space can be achieved owing to

placing properly designed corrugations at the exit interface [44–48].

Asymmetric or unidirectional SPs that appear while Lorentz reciprocity remains probably belong to the most interesting regimes obtainable in metallic gratings. They can be obtained if the conditions of SP excitation at the two sides (left and right) and/or interfaces (front and back) differ. In Refs. [49–51], excitation of unidirectional, i.e. rightward or leftward propagating SPs, has been demonstrated at a corrugated slit-free interface, that has been possible owing to a proper choice of the corrugation and/or incident beam parameters. In Refs. [52] and [53], it is shown that SPs in the structures containing a subwavelength slit can be excited asymmetrically, i.e., on the left and right sides with respect to the slit, or on one of them. In this case, transmission through such a slit is a necessary counterpart of the resulting unidirectional transmission mechanism.

The metallic gratings with a subwavelength slit and identical corrugations on the left and right sides, but differing corrugations at the front- and back-side interfaces can also enable unidirectional excitation of spoof SPs and, thus, strongly asymmetric transmission [54, 55]. To obtain such an asymmetry, p-polarized incident waves are required. On the other hand, for such gratings, the SP assisted ET phenomenon has not been observed for s-polarized incident waves. However, the diode-like asymmetric beaming regime, i.e., suppression of transmission over the entire range of the observation angle for one of the two propagation directions, requires rather strong tilting. This looks disadvantageous from the point of view of the integration of such structures to optical and microwave circuits. One-way ET connected with nonreciprocal spoof SPs has been studied in Ref. [56] for a patterned metallic surface sandwiched between two magneto-optical dielectric layers. However, in contrast to Refs. [49–55], magnetization is required in this mechanism.

Being a rather general phenomenon, asymmetric transmission is often considered in the context of partial emulation of a diode-like response without using anisotropic or nonlinear constituents. Instead, only isotropic, linear, and passive materials are required. The diffraction relevant asymmetric transmission can be obtained in nonsymmetric photonic [57–59] and sonic [60] crystals, and

nonsymmetric gratings that contain ultralow-index material layers [61]. In turn, the polarization conversion relevant mechanism is associated, first of all, with subwavelength and resonator based chiral metamaterials. By using such artificial materials, it has been shown that asymmetry in transmission can be obtained for circularly [62–64] and linearly [65,66] polarized incident waves. In particular, an ultrathin structure for the achievement of diode-like transmission for incident and outgoing plane waves at the price of extremely strong cross-polarization conversion has recently been suggested [66]. However, due to its periodic nature in the transverse plane, the field intensity of a transmitted wave through this structure is not dependent on the observation angle in the far-field. To the best of our knowledge, the studies in Refs. [56–66] have not been connected with the beaming regime.

In this chapter, we will first theoretically show that the achievement of bound surface modes, which lie below the light line, is possible in one-dimensional periodic groove and two-dimensional periodic hole geometries. Next, we will briefly discuss the underlying physical mechanism responsible for the ET and beaming phenomena. We will finalize the chapter by demonstrating the one-way excitation of spoof SPs in a composite structure that consists of a metallic grating with a subwavelength slit and a 90° polarization rotator. It will be evident that the one-way spoof SP excitation results in a reversible diodelike beaming regime.

3.2 Spoof Surface Plasmons

We have stated that the excitation of SPs on the surface of a perfect electric conductor (PEC) is not achievable since the resultant mode profile is highly delocalized. However, it has been shown that spoof or designer SPs can be excited on the surface of a PEC if the surface is properly perforated. This section is adapted from Ref. [67], which is a great paper demonstrating the theoretical origin of spoof SPs by benefiting from the effective medium theory.

3.2.1 One-Dimensional Array of Vertical Grooves

First, we assume a one-dimensional PEC structure that is composed of periodic vertical grooves and ridges. The periodicity of the structure in the x direction is given by d. The width of the grooves and the height of the ridges are given by a and h, respectively. The structure is assumed to be infinitely periodic along the x-axis. Furthermore, the structure is infinitely long along the y-axis. Here, we are interested in the possibility of achieving a bound and propagating (along the x-axis) surface mode. First of all, assume that this structure is illuminated by an obliquely incident p-polarized plane wave such that the magnetic field is along the y-axis. Therefore, the incident wave has electric field components along both the x- and the z-axes. We can then write the corresponding normalized electric field vector of the incident wave in the following form:

$$\mathbf{E}_{\text{inc}} = \hat{\mathbf{x}}\frac{1}{\sqrt{d}}e^{ik_x x}e^{ik_z z} - \hat{\mathbf{z}}\frac{1}{\sqrt{d}}\frac{k_x}{k_z}e^{ik_x x}e^{ik_z z}, \tag{3.1}$$

where $k_0 = w/c$, $k_x = k_0 \sin\theta$, and $k_z = \sqrt{k_0^2 - k_x^2}$. Here, θ denotes the angle between $\mathbf{k}_0$ and the surface normal, i.e., $-z$ direction. Correspondingly, we can express the normalized magnetic field vector as

$$\mathbf{H}_{\text{inc}} = \hat{\mathbf{y}}\frac{1}{\sqrt{d}}\frac{k_0}{k_z}e^{ik_x x}e^{ik_z z}. \tag{3.2}$$

As a result of the periodicity of the groove structure, the reflected waves are expected to be associated with diffraction orders. Accordingly, we can write the electric field vector of the reflected wave that is related to the n^{th} diffraction order as follows:

$$\mathbf{E}_{\text{ref}}^{(n)} = \hat{\mathbf{x}}\frac{1}{\sqrt{d}}e^{ik_x^{(n)}x}e^{-ik_z^{(n)}z} + \hat{\mathbf{z}}\frac{1}{\sqrt{d}}\frac{k_x^{(n)}}{k_z^{(n)}}e^{ik_x^{(n)}x}e^{-ik_z^{(n)}z}, \tag{3.3}$$

where $k_x^{(n)}$ denotes the lateral wavenumber of the n^{th} order reflected wave and $k_x^{(n)} = k_x + 2\pi n/d$, $n = -\infty, ..., -1, 0, 1, ..., \infty$. Consequently, we obtain $k_z^{(n)} = \sqrt{k_0^2 - (k_x^{(n)})^2}$. By using a similar approach, we can express the magnetic field

vectors of the reflected waves as

$$\mathbf{H}_{\text{ref}}^{(n)} = -\hat{\mathbf{y}}\frac{1}{\sqrt{d}}\frac{k_0}{k_z^{(n)}}e^{ik_x^{(n)}x}e^{-ik_z^{(n)}z}. \tag{3.4}$$

At this stage, we assume that the width of the grooves, a, is much smaller than the wavelength of the incident light, λ_0. In other words, the cut-off frequencies of all the TM_n modes, where $n \neq 0$, are assumed to be below $f = c/\lambda_0$. As a consequence, only the fundamental TM_0 mode, which does not have a cut-off frequency, can propagate inside the grooves. Note that this fundamental mode is essentially a TEM mode with electric and magnetic field vectors along the x- and y-axes, respectively. Under this assumption, we can express the electric field of the fundamental TM mode inside the grooves as

$$\mathbf{E}_{\text{TM}}^{\pm} = \hat{\mathbf{x}}\frac{1}{\sqrt{a}}e^{\pm ik_0 z}, \tag{3.5}$$

where $+$ and $-$ signs denote the $+z$ (forward) and $-z$ (backward) propagating waves. In a similar fashion, the magnetic field of this mode is written as follows:

$$\mathbf{H}_{\text{TM}}^{\pm} = \pm\hat{\mathbf{y}}\frac{1}{\sqrt{a}}e^{\pm ik_0 z} \tag{3.6}$$

Now, let us define the region, which is free-space, where the incident and reflected waves propagate as region I. In addition, the region consisting of the groove structure is called region II. The total field in region I is equal to the vectorial summation of the incident wave and reflected diffraction orders, and is written as

$$\mathbf{E}_{\text{I}} = \mathbf{E}_{\text{inc}} + \sum_{n=-\infty}^{+\infty} \rho_n \mathbf{E}_{\text{ref}}^{(n)}, \tag{3.7}$$

where ρ_n denotes the reflection coefficient of a particular diffraction order. Similarly, the total magnetic field in region I is given by

$$\mathbf{H}_{\text{I}} = \mathbf{H}_{\text{inc}} + \sum_{n=-\infty}^{+\infty} \rho_n \mathbf{H}_{\text{ref}}^{(n)}. \tag{3.8}$$

In region II, the total electric field is the vectorial summation of forward and

backward propagating waves. The coefficients of these modes are expectedly equal in magnitude due to complete reflection from the groove/PEC interface at $z = h$, but different in phase. Therefore, we express the total electric field in region II as

$$\mathbf{E}_{\mathrm{II}} = C_{+}E^{+}_{\mathrm{TM}} + C_{-}E^{-}_{\mathrm{TM}}, \tag{3.9}$$

where C_+ and C_- denote the coefficients of the forward and backward propagating waves. Similarly, the total magnetic field in region II is given by

$$\mathbf{H}_{\mathrm{II}} = C_{+}H^{+}_{\mathrm{TM}} + C_{-}H^{-}_{\mathrm{TM}}. \tag{3.10}$$

Now that we have written the total electric and magnetic fields in regions I and II, we can match the boundary conditions for the purpose of determining ρ_n. We have four boundary conditions to satisfy: (i) $\hat{\mathbf{n}} \times \mathbf{E}_{\mathrm{I}} = 0$ at $z = 0$ on the ridges, (ii) $\hat{\mathbf{n}} \times (\mathbf{E}_{\mathrm{I}} - \mathbf{E}_{\mathrm{II}}) = 0$ at $z = 0$ on the grooves, (iii) $\hat{\mathbf{n}} \times (\mathbf{H}_{\mathrm{I}} - \mathbf{H}_{\mathrm{II}}) = 0$ at $z = 0$ on the grooves, and (iv) $\hat{\mathbf{n}} \times \mathbf{E}_{\mathrm{II}} = 0$ at $z = h$ inside the groove. Afterwards, it requires simple algebra to satisfy these boundary conditions by using Eqs. 3.7, 3.8, 3.9, and 3.10. As a result, we obtain

$$\rho_n = -\delta_{n,0} - \frac{2i\tan(k_0 h)S_0 S_n k_0/k_z}{1 - i\tan(k_0 h)\sum\limits_{n=-\infty}^{+\infty} S_n^2 k_0/k_z^{(n)}}, \tag{3.11}$$

where S_n is the overlap integral between the n^{th} reflection order and the fundamental TM mode and is given by

$$S_n = \frac{1}{\sqrt{ad}}\int\limits_{-a/2}^{a/2} e^{ik_x^{(n)}x}dx = \sqrt{\frac{a}{d}}\frac{\sin(k_x^{(n)}a/2)}{k_x^{(n)}a/2}. \tag{3.12}$$

In Eq. 3.11, $\delta_{n,0}$ is the Kronecker delta function that is defined as

$$\delta_{n,0} = \begin{cases} 1, & \text{if } n = 0 \\ 0, & \text{if } n \neq 0 \end{cases}. \tag{3.13}$$

Next, let us recall our initial assumption that suggests $a \ll \lambda_0$. Under this

assumption, we can safely assume that $\rho_n = 0$ for $n \neq 0$ due to the obtaining of an imaginary propagation constant for the reflected diffraction orders in this case. Hence, we find that the overall reflection coefficient, ρ, is equal to ρ_0 and given by

$$\rho = -\frac{1 + iS_0^2 \tan(k_0 h) k_0/k_z}{1 - iS_0^2 \tan(k_0 h) k_0/k_z}. \tag{3.14}$$

The value of w that corresponds to a certain k_x value can be calculated by using the divergences of ρ that is given in Eq. 3.14. As a result, the dispersion relation for such a geometry can be written as

$$iS_0^2 \tan(k_0 h) k_0/k_z = 1. \tag{3.15}$$

If we only consider the bound modes for which $k_x > k_0$ and k_z is purely imaginary, we can write $k_z = i\sqrt{k_x^2 - k_0^2}$. Correspondingly, Eq. 3.15 can be written in a more compact form as follows:

$$\frac{a}{d} \frac{\sin^2(k_x a/2)}{(k_x a/2)^2} \tan(k_0 h) = \frac{\sqrt{k_x^2 - k_0^2}}{k_0}. \tag{3.16}$$

For the purpose of providing an example, we plot w versus k_x for $a/d = 0.5$ and $h/d = 0.25$ in Fig. 3.1. One can easily see that the resultant dispersion curve is very similar to that for unperforated lossy metals at optical frequencies [68]. It is known that SPs can be excited at metal/dielectric interfaces as a result of the achievement of such a dispersion curve where some modes lie below the light line. The same is also valid for perforated PECs at much lower frequencies. In such geometries, bound surface modes that decay exponentially in the $-z$ direction and propagate along the x-axis can be excited owing to the additional lateral wavevector $G = 2\pi n/d$ obtained due to the periodic nature of the structure.

One can also show that the one-dimensional periodic vertical groove structure discussed here can be analyzed within the framework of the effective medium theory. By doing so, one obtains an anisotropic effective medium with $\epsilon_x^{\text{eff}} = d/a$, $\epsilon_y^{\text{eff}} = \epsilon_z^{\text{eff}} = \infty$, $\mu_x^{\text{eff}} = 1$, and $\mu_y^{\text{eff}} = \mu_z^{\text{eff}} = a/d$. The dispersion relation for such

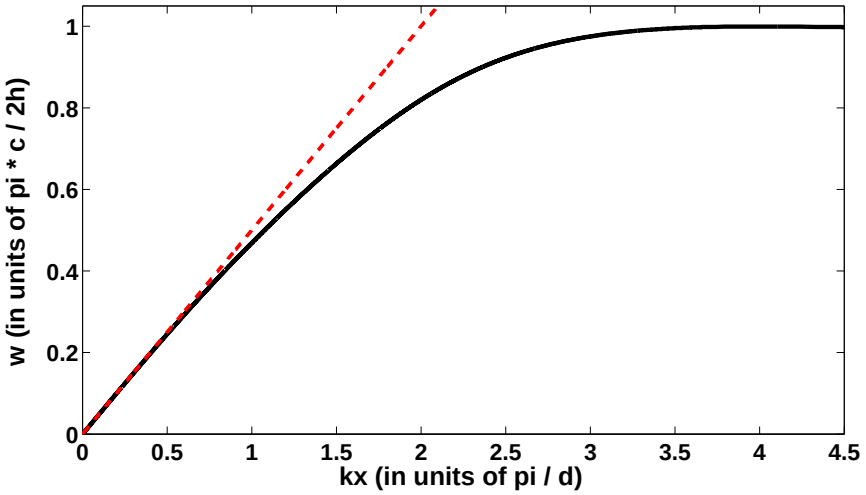

Figure 3.1: The dispersion relation $w(k_x)$ of the bound surface states ($k_x > k_0$), which are supported by the one-dimensional array of grooves, as obtained from Eq. 3.16. Geometrical parameters are taken as $a/d = 0.5$ and $h/d = 0.25$. The red dashed line shows the light line $k = w/c$.

an effective medium is given by [67]

$$\frac{a}{d}\tan(k_0 h) = \frac{\sqrt{k_x^2 - k_0^2}}{k_0}. \tag{3.17}$$

Note that

$$\lim_{k_x a \to 0} \frac{\sin^2(k_x a/2)}{(k_x a/2)^2} = 1 \tag{3.18}$$

and therefore, Eqs.3.16 and 3.17 are approximately equal when $k_x a \ll 1$.

To summarize, SPs cannot be excited at a PEC/dielectric interface. However, one can perforate the metal surface in the shape of periodic vertical grooves and by doing so, a dispersion relation that is similar to that of lossy metals at optical frequencies can be realized. Thus, the excitation of bound surface modes, which are called spoof SPs, can be enabled in such geometries.

3.2.2 Two-Dimensional Array of Vertical Holes

Secondly, we consider a geometry where infinitely periodic holes with a side length of a are drilled into a semi-infinite PEC and the periodicity of the holes are given by d along both x- and y-axes. We assume that the structure starts at $z = 0$ and is infinitely long in the $+z$ direction. Furthermore, we have free-space for $z < 0$. Finally, the holes are assumed to be filled with a dielectric material with a relative permittivity of ϵ_h. Here, we are interested in the possibility of obtaining bound modes at the PEC/free-space interface. Similar to what is done in Sec. 3.2.1, we will first derive the total reflection coefficient and, then, arrive to the dispersion relation by evaluating the divergences of the reflection coefficient.

We first start by writing the normalized electric and magnetic field components of the incident TM wave. The corresponding normalized **E** and **H** vectors are expressed as follows:

$$\mathbf{E}_{\text{inc}} = \hat{\mathbf{x}}\frac{1}{d}e^{ik_x x}e^{ik_z z} - \hat{\mathbf{z}}\frac{1}{d}\frac{k_x}{k_z}e^{ik_x x}e^{ik_z z}, \tag{3.19a}$$

$$\mathbf{H}_{\text{inc}} = \hat{\mathbf{y}}\frac{1}{d}\frac{k_0}{k_z}e^{ik_x x}e^{ik_z z}. \tag{3.19b}$$

In Sec. 3.2.1, we first wrote the reflected wave as the vectorial summation of infinitely many diffraction orders, then, we assumed $a \ll \lambda$, and we finally stated that only the first diffraction order is propagating whereas all the higher ones are evanescent. As a result, it is assumed that the total reflection coefficient is equal to the reflection coefficient of the zeroth diffraction order. In this analysis, we directly assume that the reflected wave is composed of only the zeroth diffraction order. Hence, the electric and magnetic field components of the reflected wave can be written as

$$\mathbf{E}_{\text{ref}} = \hat{\mathbf{x}}\frac{1}{d}e^{ik_x x}e^{-ik_z z} + \hat{\mathbf{z}}\frac{1}{d}\frac{k_x}{k_z}e^{ik_x x}e^{-ik_z z}, \tag{3.20a}$$

$$\mathbf{H}_{\text{ref}} = -\hat{\mathbf{y}}\frac{1}{d}\frac{k_0}{k_z}e^{ik_x x}e^{-ik_z z}. \tag{3.20b}$$

The assumption of $a \ll \lambda$ implies that only the fundamental TE mode propagates inside the holes. This is a fair approximation since the slowest decaying mode is

the fundamental one. By considering the boundary condition, which states that the tangential electric field must be zero at a PEC surface, one can easily prove that the lateral wavenumber of the TE_n mode is given by $\pm n\pi/a$. Afterwards, we can write the electric and magnetic field vectors for the fundamental TE mode inside the holes as follows:

$$\mathbf{E}_{\mathrm{TE}} = \hat{\mathbf{x}}\frac{\sqrt{2}}{a}e^{iq_z z}\sin\left(\frac{\pi y}{a}\right), \tag{3.21a}$$

$$\mathbf{H}_{\mathrm{TE}} = -\hat{\mathbf{y}}\frac{\sqrt{2}}{a}\frac{q_z}{k_0}e^{iq_z z}\sin\left(\frac{\pi y}{a}\right) - \hat{\mathbf{z}}\frac{\sqrt{2}}{a}\frac{i\pi}{ak_0}e^{iq_z z}\sin\left(\frac{\pi y}{a}\right), \tag{3.21b}$$

where q_z is the propagation constant of the fundamental TE mode and is given by $q_z = \sqrt{\epsilon_h k_0^2 - \pi^2/a^2}$.

Now, we can express the field distribution in region I ($z < 0$) as the vectorial summation of the incident and reflected fields and accordingly, we have

$$\mathbf{E}_{\mathrm{I}} = \mathbf{E}_{\mathrm{inc}} + \rho\mathbf{E}_{\mathrm{ref}}, \tag{3.22a}$$

$$\mathbf{H}_{\mathrm{I}} = \mathbf{H}_{\mathrm{inc}} + \rho\mathbf{H}_{\mathrm{ref}}. \tag{3.22b}$$

When writing the field distribution in region II ($z > 0$), we need to remember that the holes are assumed to be infinitely long and therefore, it is not expected to observe backward propagating waves inside the holes since there is not a mechanism to cause reflection. Accordingly, we write

$$\mathbf{E}_{\mathrm{II}} = \tau\mathbf{E}_{\mathrm{TE}}, \tag{3.23a}$$

$$\mathbf{H}_{\mathrm{II}} = \tau\mathbf{H}_{\mathrm{TE}}, \tag{3.23b}$$

where τ is the transmission coefficient. We perform the application operation of the boundary conditions as stated in Sec. 3.2.1. It can easily be shown that the resultant reflection coefficient is given by

$$\rho = \frac{k_0^2 S_0^2 - q_z k_z}{k_0^2 S_0^2 + q_z k_z}, \tag{3.24}$$

where S_0 is the overlap integral of the incident field and the fundamental TE

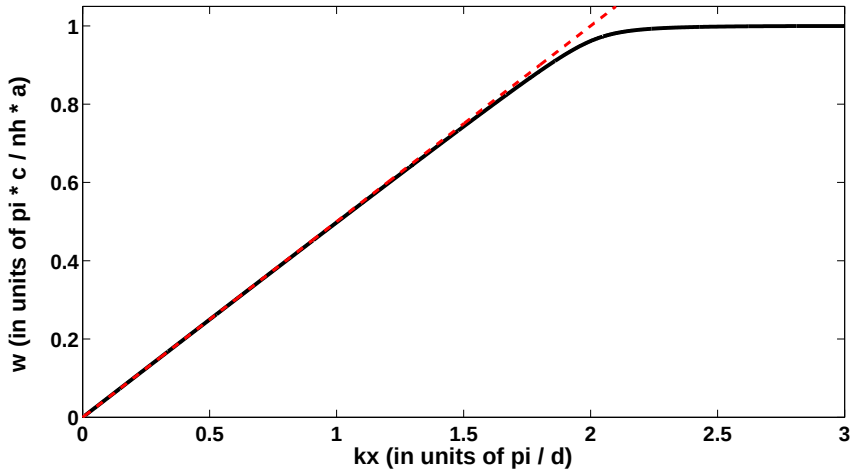

Figure 3.2: The dispersion relation $w(k_x)$ of the bound surface states ($k_x > k_0$), which are supported by the two-dimensional array of holes, as obtained from Eq. 3.27. Geometrical parameters are taken as $a/d = 0.5$ and $\epsilon_h = n_h^2 = 1$. The red dashed line shows the light line $k = w/c$.

mode along one period and is given by

$$S_0 = \frac{\sqrt{2}}{ad} \int_{-a/2}^{a/2} e^{ik_x x} dx \int_0^a \sin\left(\frac{\pi y}{a}\right) dy = \frac{2\sqrt{2}}{\pi d} \frac{\sin\left(k_x a/2\right)}{k_x a/2}. \tag{3.25}$$

The dispersion relation $w(k_x)$ can be obtained by considering the divergences of Eq. 3.24 and correspondingly, we obtain

$$k_0^2 S_0^2 = -q_z k_z. \tag{3.26}$$

By expanding S_0, q_z, and k_z, we can write the dispersion relation as follows:

$$\frac{\sqrt{k_x^2 - k_0^2}}{k_0^2} = \frac{8a^2}{\pi^2 d^2 \sqrt{(\pi/a)^2 - \epsilon_h k_0^2}} \frac{\sin^2(k_x a/2)}{(k_x a/2)^2}. \tag{3.27}$$

In order to provide an example, we solve Eq. 3.27 for $a/d = 0.5$ and $\epsilon_h = n_h^2 = 1$ and the result is shown in Fig. 3.2. One can see that the slope of the curve changes abruptly whereas the slope of the curve shown in Fig. 3.1 changes more smoothly. This observation implies that bound surface modes can be achieved

only in the close vicinity of $w = \pi c/(n_h a)$ for the two-dimensional hole structure. In other words, the condition $k_x > k_0$ is only achieved in a narrowband region that is in the close neighborhood of $w = \pi c/(n_h a)$. On the other hand, $k_x > k_0$ is achieved in a broader frequency range for the one-dimensional groove structure, see Fig. 3.1. As a result, one can intuitively expect the spoof SP resonance for the one-dimensional groove geometry to be much broader than that for the two-dimensional hole geometry. Another difference is that the most strongly bound (confined) modes are obtained at $w = \pi c/(2h)$ and $w = \pi c/(n_h a)$ for the one-dimensional groove and two-dimensional hole geometries, respectively.

One can also show that the two-dimensional and semi-infinite periodic vertical hole structure discussed here can be analyzed within the framework of the effective medium theory. By doing so, one obtains an anisotropic effective medium with

$$\epsilon_x^{\text{eff}} = \epsilon_y^{\text{eff}} = \frac{\epsilon_h}{S_0^2}\left(1 - \frac{\pi^2 c^2}{a^2 \epsilon_h w^2}\right), \tag{3.28}$$

$\epsilon_z^{\text{eff}} = \infty$, $\mu_x^{\text{eff}} = \mu_y^{\text{eff}} = S_0^2$, and $\mu_z^{\text{eff}} = \infty$. The dispersion relation obtained for such an effective medium coincides with the one given in Eq. 3.27. Note that the condition $a \ll \lambda$ must be satisfied for the effective medium approximation to be sensible.

3.3 Extraordinary Transmission and Beaming

In 1944, Bethe theoretically studied the diffraction of electromagnetic radiation by a circular subwavelength hole milled into an infinitely thin perfectly conducting medium [69]. He found that the transmission coefficient for a normally incident plane wave scales by $(a/\lambda)^4$, where a denotes the radius of the hole. The predictions made by Bethe are perfectly correct; however, some other scenarios such as the presence of sufficiently close periodic subwavelength holes or the presence of periodic corrugations around the subwavelength hole are not considered. Moreover, Bethe predicts that the transmitted wave should be strongly diffracted in almost all angles upon transmission. The reason behind the strongly attenuated

transmission is that the subwavelength hole geometry does not support any propagating modes if $a/\lambda \ll 1$ and the incident wave has to tunnel through the hole while being attenuated exponentially.

One can use other geometries for the aperture in order to modify the characteristics of the waveguide created by the aperture. It is known that a single coaxial aperture [70] or an annular aperture array [71] can allow TEM modes that do not exhibit a cut-off frequency and, therefore, be used for the achievement of enhanced transmission. However, we are more interested here in the possibility of using (spoof) SPs for transmission enhancement. It is well-known that the achievement of enhanced transmission through a subwavelength circular or rectangular aperture can be made possible by structuring the metallic screen in a periodic manner. Owing to this structuring operation, the excitation of (spoof) SPs can be made possible and thereby, the electric field can be very strongly enhanced around the aperture. The structuring operation, of course, cannot result in allowed propagating modes; however, it can increase the magnitude of the field significantly and this enhancement results in enhanced transmission. Generally, the phase matching requirements imposed by the dispersion relation of (spoof) SPs requires a certain geometry for the achievement of enhanced transmission at a particular wavelength. The corrugations must be designed such that the frequency of strongest (spoof) SP excitation must correspond to the desired frequency of enhanced transmission. It is very interesting that a normalized-to-area transmission coefficient that is larger than unity can be achieved in such structures. In other words, the transmitted power through the subwavelength aperture can be larger than that incident on the aperture. This occurs because the corrugations behave like an antenna at the (spoof) SP excitation wavelength and thus, a large power can be collected from a broad area and directed to the aperture. This ET phenomenon was first demonstrated by Ebbesen in 1998 [38] and has been a subject of intense attention ever since.

The anticipated wavelengths of enhanced transmission can be evaluated by considering the phase matching requirements. Assume that we have a two-dimensional periodic lattice of square holes with a periodicity of a_0. Then, the wavevector of a p-polarized incident wave is converted to the following one due

to the periodicity of the geometry [72]:

$$\mathbf{k} = \hat{\mathbf{x}} k_0 \sin(\theta) \pm \hat{\mathbf{x}} n \frac{2\pi}{a_0} \pm \hat{\mathbf{y}} m \frac{2\pi}{a_0}, \tag{3.29}$$

where n and m are integers. Therefore, at normal incidence, the following relation should hold in order to enable the excitation of (spoof) SPs:

$$k_{\mathrm{SP}} = \frac{2\pi}{a_0} \sqrt{n^2 + m^2}, \tag{3.30}$$

where k_{SP} is the (spoof) SP wavevector obtained by solving the corresponding dispersion relation. For instance, we know that the SP dispersion relation at optical frequencies is given by [68]

$$k_{\mathrm{SP}} = \frac{w}{c} \left(\frac{\epsilon_1 \epsilon_2}{\epsilon_1 + \epsilon_2} \right), \tag{3.31}$$

where ϵ_1 and ϵ_2 denote the dielectric constants of the surrounding dielectric and the metal, respectively. One can obtain the following SP excitation condition in a two-dimensional square hole geometry by combining Eqs. 3.30 and 3.31:

$$\sqrt{n^2 + m^2} \lambda = a_0 \left(\frac{\epsilon_1 \epsilon_2}{\epsilon_1 + \epsilon_2} \right). \tag{3.32}$$

One can rearrange Eq. 3.32 to obtain the wavelength of the strongest SP excitation for a certain two-dimensional hole geometry. The result is given by

$$\lambda_{\mathrm{SP}} = \frac{a_0}{\sqrt{n^2 + m^2}} n_{\mathrm{SP}}, \tag{3.33}$$

where

$$n_{\mathrm{SP}} = \left(\frac{\epsilon_1 \epsilon_2}{\epsilon_1 + \epsilon_2} \right). \tag{3.34}$$

Note that n_{SP} can be defined as in Eq. 3.34 since one can write $k_{\mathrm{SP}} = w n_{\mathrm{SP}}/c$ [compare to Eq. 3.31].

The same analysis can be made for one-dimensional periodic groove geometries. In this case, the wavevector of a p-polarized incident wave is converted to

the following one due to periodicity:

$$k_x = k_0 \sin(\theta) \pm n\frac{2\pi}{b_0}, \tag{3.35}$$

where b_0 denotes the period of the corrugations. At normal incidence, the following condition should be satisfied for (spoof) SP excitation:

$$k_{\mathrm{SP}} = n\frac{2\pi}{b_0}. \tag{3.36}$$

At optical frequencies, SP excitation condition can be written by using Eqs. 3.31 and 3.34 as follows:

$$\lambda_{\mathrm{SP}} = \frac{b_0}{n} n_{\mathrm{SP}}. \tag{3.37}$$

We have stated that corrugations placed on the input interface can enable the excitation of (spoof) SPs and result in enhanced transmission through subwavelength apertures below the fundamental mode cut-off frequency. Similarly, the spatial profile of the transmitted light can be controlled by patterning the output interface properly. These corrugations at the output interface do not modify the wavelengths of (spoof) SP resonances. However, one can achieve a highly directional emission with a narrow beaming angle. This beaming property was first demonstrated in Ref. [44] for both one-dimensional slit and two-dimensional hole apertures. The beaming phenomenon is theoretically analyzed in Ref. [73] and the reader is referred to inspect that paper for a further insight. It was shown that beaming properties originate from the formation of EM surface resonances. These resonances arise due to the combination of single groove cavity modes, which are sensitive to the groove height and width, and the coupling between indentations [73]. In other words, the beaming effect arises from tight-binding-like coupling between localized groove modes and the interference of their diffracted wave patterns [68]. It is very promising in terms of possible applications that the wavelength and direction of beaming can be controlled by selecting the geometrical parameters accordingly.

3.4 One-way reciprocal Spoof Surface Plasmons and Relevant Reversible Diodelike Beaming

In this section, we propose a new reciprocal mechanism, which enables the unidirectional excitation of SPPs in a composite geometry and as a result, the diodelike beaming effect. In contrast to earlier studies that are based on asymmetric beaming, our mechanism does not require the tilting of the structure, i.e., the desired effect can be achieved by normally incident waves. Moreover, the incident waves can be either s or p polarized. The proposed structure also exhibits the reversibility of the direction of strong transmission. For example, it will be evident that transmission is strong for one of the incidence directions for s polarization while it is strong for the reverse direction for p polarization.

In order to realize the desired one-way spoof SPP excitation, one-way ET, and diodelike beaming effect, we envision that two counterparts are required: a symmetric metallic grating with a subwavelength mesh, and a *unity* conversion efficiency and chiral metamaterial based 90° polarization rotator. We designed the metallic grating such that the frequency of strongest transmission coincides with the operation frequency of the rotator. The rotator exhibits a unity transmission and cross-polarization conversion efficiency at the operation frequency. At the end, we find that the most promising regimes are those realized within a thickness that is smaller than one free-space wavelength.

3.4.1 Theoretical Background and Design

In this subsection, we will first present the general idea and the projected operation principle required for the realization of the desired effect. Then, we will discuss the choice of the structure components. Finally, we will analyze the beaming effect in the absence and presence of the rotator.

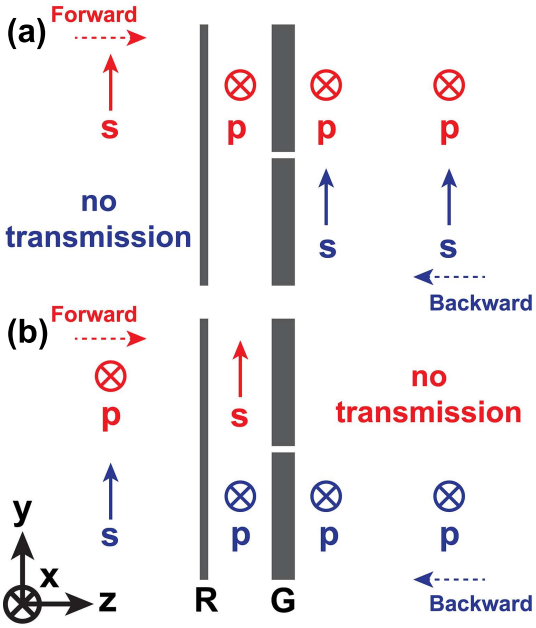

Figure 3.3: Demonstration of the projected operation principle of the proposed composite structure for (a) s- and (b) p-polarized incident waves. The polarization rotator and the metallic grating are denoted by R and G, respectively. The solid arrows and the crosses show the orientations of the electric field vector for s- and p-polarized waves, respectively. A dashed arrow indicates the propagation direction of a wave with the same color, i.e. forward or backward. Reprinted with permission from [39]. Copyright 2013 by the American Physical Society.

3.4.1.1 General idea

We envision that the one-way transmission feature, which is relevant to the transmission characteristics of the polarization rotator, allows one obtaining the one-way excitation of spoof SPs and thus, relevant unidirectional ET and beaming, i.e., those existing only for one of the two opposite normal incidence directions for the same polarization state (s or p). Accordingly, we target transmitting as much power as possible for the illumination from one side, whereas the transmitted power should be approximately zero for the illumination from the opposite direction, provided that the polarization state is the same. For the sake of definiteness, we refer to the transmission at the incidence from the rotator side as the forward transmission. The backward transmission corresponds to the incidence from the opposite (grating) side.

The general idea of this diode-like transmission mechanism is schematically illustrated in Fig. 3.3. The resulting structure does not show spatial symmetry in the z-direction. An s-polarized wave incident on the polarization rotator can be converted to p-polarization and transmitted through the subwavelength slit with the assistance of spoof SPs, see Fig. 3.3(a). In turn, an s-polarized wave that is directly impinged on the grating side is reflected since spoof SP modes are not supported for this polarization state.

A p-polarized wave incident on the polarization rotator is converted to s-polarization and, therefore, cannot be transmitted through the subwavelength slit, see Fig. 3.3(b). On the contrary, a p-polarized wave impinged on the grating from the opposite side is transmitted and, afterwards, should be converted to the s-polarization with the assistance of the polarization rotator. Furthermore, Fig. 3.3 shows that the direction of strong transmission can be reversed by simply changing the polarization of the incident light from s to p and vice versa.

In fact, the underlying logic is similar to a big extent to a Faraday-rotator based isolator, a nonreciprocal and widely used device [16]. However, in contrast to it, the reciprocal structure presented in this paper enables diode-like asymmetric transmission in the beaming regime for s- and p-polarized incident waves and, furthermore, at a relatively small thickness of the composite structure, while no magnetization is required. On the other hand, it should be noted that a Faraday isolator can operate when the incident light is unpolarized, while the composite structure presented in this paper operates for particular polarization states of the incident light.

Next, let us briefly discuss the conditions required for the obtaining of the desired directional selectivity for linearly polarized incident waves. First of all, we take,

$$f_{SP} = f_{PR}, \tag{3.38}$$

where f_{SP} and f_{PR} denote the spoof SP and the cross-polarization conversion resonance frequencies, respectively. Since the distance between the grating and the rotator, d, can be chosen in the proposed designs so that $d \ll \lambda_{PR}$ (see

Sec. 3.4.2), coupling is expected to occur due to the interaction of the near-fields of the structures and the resonance frequency of the composite structure, $f_{CS} \neq f_{SP} = f_{PR}$, in the general case. However, the use of Eq. 3.38 is quite well justified because SP resonances are wide and that gives some freedom in the choice of f_{SP} and, therefore, in the metallic grating design. Hence, a proper choice of f_{PR} is the most important.

Despite exhibiting optical activity, the metamaterial based polarization rotator is a reciprocal structure, assuming that only linear and reciprocal materials are going to be used. Assuming propagation in the $+z$ direction, operation of the polarization rotator can be qualitatively characterized in the plane-wave framework by using the Jones matrix formalism as follows:

$$\begin{pmatrix} E_p^f \\ E_s^f \end{pmatrix} = \begin{pmatrix} T_{pp} & T_{ps} \\ T_{sp} & T_{ss} \end{pmatrix} \begin{pmatrix} E_{pi}^f \\ E_{si}^f \end{pmatrix}, \tag{3.39}$$

where E_{pi}^f and E_{si}^f are the p– and s–polarized components of the forward propagating incident electric field that correspond to x and y directions, respectively; T_{pp} and T_{ss} are the co-polarization transmission coefficients, and T_{ps} and T_{sp} are the cross-polarization transmission coefficients. Lorentz reciprocity requires that, for incident waves propagating in the $-z$ direction, the transmitted electric field is expressed as [15]:

$$\begin{pmatrix} E_p^b \\ E_s^b \end{pmatrix} = \begin{pmatrix} T_{pp} & -T_{sp} \\ -T_{ps} & T_{ss} \end{pmatrix} \begin{pmatrix} E_{pi}^b \\ E_{si}^b \end{pmatrix}. \tag{3.40}$$

For an idealized 90° polarization rotator, we have $T_{pp} = T_{ss} = 0$ and $T_{sp} = -T_{ps} = 1$ [26].

The metallic grating with a subwavelength slit exhibits polarization selectivity and a reciprocal response for normally incident waves. The latter means the reception of the same electric field if the transmitter antenna becomes the receiver and vice versa. Thus, the composite structure should also be reciprocal. Then, one may expect that $|t_{pp}^f| = |t_{pp}^b|$, $|t_{ss}^f| = |t_{ss}^b|$, $|t_{sp}^f| = |t_{ps}^b|$, and $|t_{ps}^f| = |t_{sp}^b|$, where t_{ij} denotes the received electric field when the transmitter antenna emits

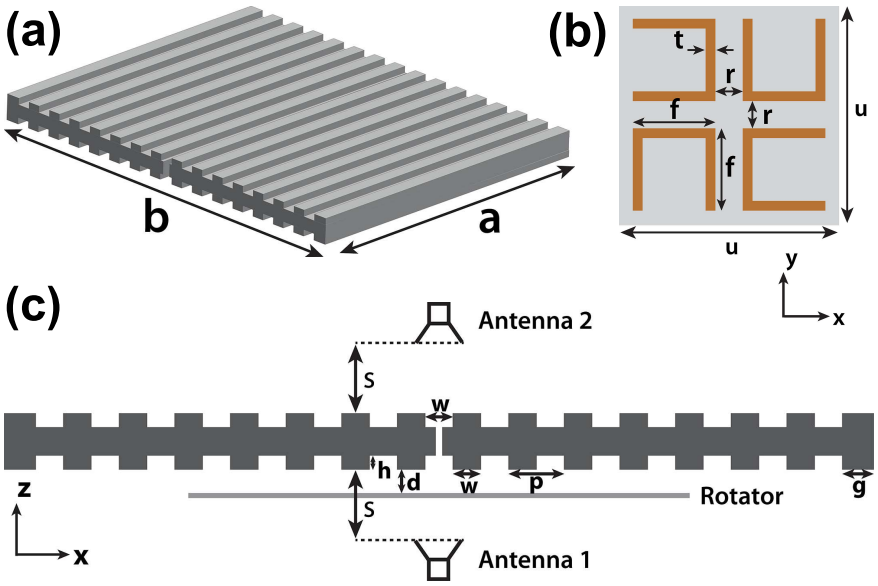

Figure 3.4: (a) Isometric view of the metallic grating with a subwavelength slit, (b) front layer of the polarization rotator, and (c) schematic of the experimental setup. In plot (c), the distance between the antennas and the grating, S, is not drawn to scale. Reprinted with permission from [39]. Copyright 2013 by the American Physical Society.

j-polarized radiation and the receiver antenna receives i-polarized radiation, and, here, it is assumed that the antennas are aligned such that their main lobe maxima lie in the $\pm z$ directions. Note that this does not imply the transmitted waves for forward and backward incidence cases have identical spatial field profiles. The possible differences between them belongs to the basic features of the structures with the broken spatial inversion symmetry, which are associated with asymmetric transmission. In Sec. 3.4.2.1, this feature will be demonstrated by using the experimental $|t_{ij}|$ spectra.

3.4.1.2 Choice of Structure Components

We utilize the chiral metamaterial based ultrathin 90° polarization rotator from Ref. [26], which perfectly fulfils the above mentioned requirements. It exhibits the unity transmission of the circularly polarized eigenwaves with a phase difference of π, so that, contrary to Ref. [66], there is no sensitivity on the angle of

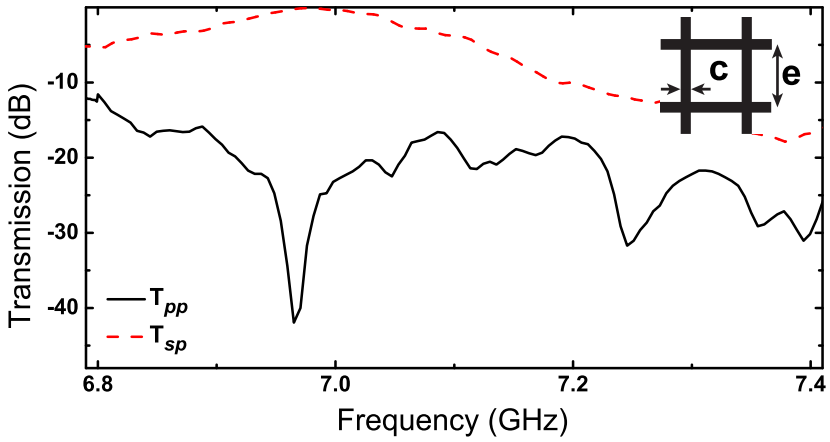

Figure 3.5: Magnitudes of the experimental linear transmission coefficients for the polarization rotator. The maximum of $|T_{sp}|$ is observed at 6.98 GHz. The inset shows the geometry of the subwavelength mesh sandwiched between the front and back layers of the rotator. Reprinted with permission from [39]. Copyright 2013 by the American Physical Society.

rotation of the polarization plane as long as the wavevector, $\mathbf{k}$, of the incident wave is orthogonal to the material plane. The polarization rotator consists of three layers. A unit cell of each of the two resonant layers is composed of four mutually rotated U-shaped split ring resonators. The third layer, a subwavelength mesh that exhibits a negative effective permittivity, is placed between the resonant layers and allows for the obtaining of unity transmission due to the electromagnetic tunneling effect, see Sec. 2.5. The two-dimensional metallic grating is assumed to have the same corrugations at front- and back-side interfaces and a single subwavelength slit at the center. To design a proper metallic grating, one of the early suggested performances can simply be rescaled for the purpose of satisfying Eq. 3.38.

Figure 3.4 shows the grating geometry, a unit cell of one of the two resonant layers of the polarization rotator and the experiment setup. The utilized geometrical parameters for the grating are the following: $a = 400$ mm, $b = 500$ mm, $w = 16$ mm, $p = 32$ mm, $h = 8$ mm, and $g = 18$ mm. The width and the length of the slit are given as 4 mm and 16 mm, respectively. For the front layer of the polarization rotator, which is depicted in Fig. 3.4(b), we take $t = 0.7$ mm, $f = 6$ mm, $r = 2$ mm, and $u = 16$ mm. The back layer is obtained by rotating the

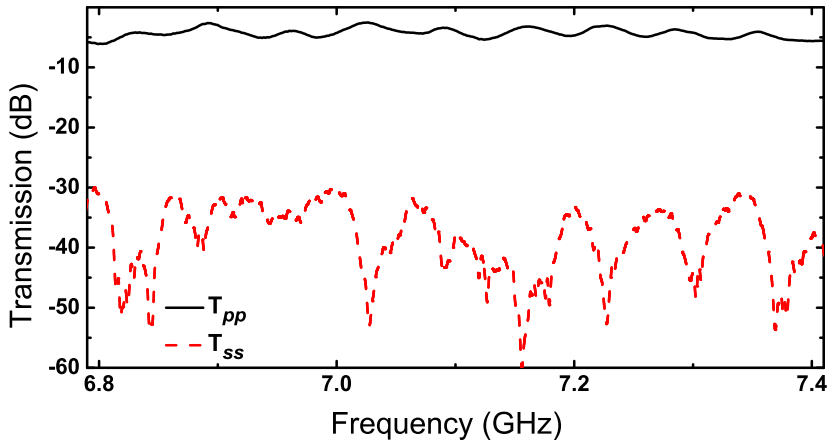

Figure 3.6: Magnitudes of the experimental linear co-polarized transmission coefficients of the metallic grating with a single subwavelength slit. Reprinted with permission from [39]. Copyright 2013 by the American Physical Society.

individual split-ring resonators of the front layer by 90° and as a result, a chiral structure with fourfold rotational symmetry is obtained. A subwavelength mesh that exhibits negative effective permittivity throughout a wide frequency range is sandwiched between the front and the back layers. Its unit cell is depicted at the inset of Fig. 3.5. The geometrical parameters for the mesh are given by $c = 0.5$ mm and $e = 3.2$ mm. Figure 3.4(c) shows the schematic of the experimental setup together with the geometrical parameters of the metallic grating with the subwavelength slit. The distance between the metallic grating and the horn antennas is set to $S = 400$ mm in the experiments.

The structures were positioned in a symmetric configuration between the antennas. The transmission coefficient measurements were performed by using an Anritsu 37369A network analyzer. For the purposes of the experimental study, we used the polarization rotator with the dimension of 18 by 18 unit cells. In Fig. 3.5, we provide the magnitudes of the experimental linear transmission coefficients for the polarization rotator, namely $|T_{pp}|$ (co-polarized component) and $|T_{sp}|$ (cross-polarized component). For the two other linear transmission coefficients, we have $T_{ss} = T_{pp}$ and $T_{ps} = -T_{sp}$ as mentioned in Sec. 3.4.1.1. According to Fig. 3, $f_{PR} \simeq 6.98$ GHz. The structure exhibits a cross-polarization conversion efficiency of 98% at this frequency.

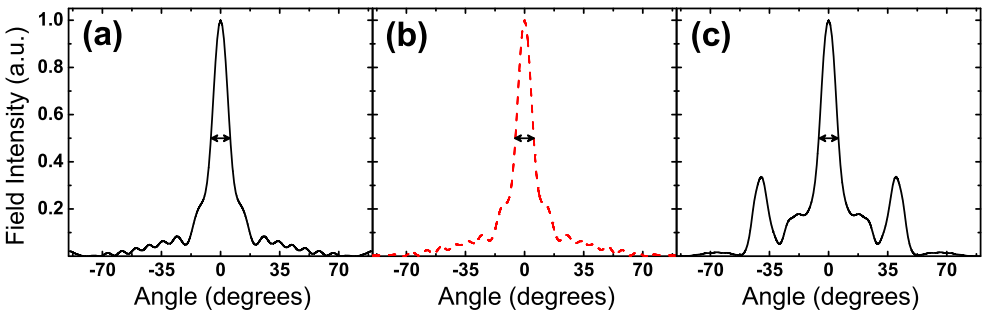

Figure 3.7: Angular distribution of electric field intensity for $d = 5$ mm at a 400 mm radial distance in the vicinity of $f = 7$ GHz for (a) the metallic grating with the subwavelength slit alone, and the composite structure at (b) forward and (c) backward illumination. Black solid and red dashed lines indicate that the incident wave is p-polarized and s-polarized, respectively. The presented results correspond to the p-, p-, and s-polarized components of the outgoing waves in (a), (b), and (c), respectively. Full-widths at half-maxima are denoted by the horizontal arrows in (a), (b), and (c). Reprinted with permission from [39]. Copyright 2013 by the American Physical Society.

In the next step, the metallic grating that contains a single subwavelength slit has been characterized experimentally. Figure 3.6 presents the linear co-polarized transmission coefficients, T_{pp} and T_{ss}. The cross-polarization transmission coefficients, T_{sp} and T_{ps}, are zero due to the lack of optical activity and, thus, are not shown. At the chosen operation frequency, $f = f_{PR} = 6.98$ GHz, $|T_{pp}| \simeq -3.5$ dB. On the other hand, $|T_{ss}| < -30$ dB throughout the frequency range of the measurement, so that the extinction ratio is better than 25 dB in the vicinity of 7 GHz. The simulation results, see Sec. 3.4.1.3, indicate that the electric field is strongly enhanced at the center of the subwavelength slit and that results in a strong coupling between spoof SPs at the front and the back sides. This results in the appearance of ET and beaming, which are known to be absent in case of a corrugation free slab.

3.4.1.3 Beaming with and without Rotator

Extensive numerical simulations (Computer Simulation Technology Microwave Studio) for $d = 5$ mm and normally incident waves in the vicinity of $f = 7$ GHz have been carried out in order to study the beaming behavior of the transmitted

co-polarized field component for the grating and cross-polarized field components for the composite structure.

Assuming that the origin of the xz-plane is located at the center of the subwavelength slit, the radial distance of the points of investigation was set to 400 mm. The examples of angular distributions of electric field intensities with respect to the observation angle are shown in Fig. 3.7. For the grating alone, the well-pronounced ET in the beaming regime is observed for a p-polarized normally incident wave, see Fig. 3.7(a). In line with the obtained results, the full-width at half-maximum (FWHM) is obtained as approximately 12°. The intensity distribution is symmetric with respect to 0° as a consequence of the symmetry with respect to the slit. In turn, transmission is expected to vanish for s-polarized incident waves due to the lack of a surface mode for this polarization state, compare to Fig. 3.6. Implied by the symmetry with respect to the xy-plane at $z = 0$, i.e., the center of the slit, transmission properties do not depend on whether the forward or the backward transmission case is considered.

Afterwards, the composite structure, which contains the rotator and the metallic grating, has been investigated for normally incident waves. The beaming regime is achievable now when the incident s-polarized wave propagates in the forward direction, i.e., it is impinged directly on the polarization rotator. This results in the appearance of an outgoing wave with a dominant p-polarized component, $|t^f_{ps}|$. Fig. 3.7(b) presents the angular intensity distribution of the transmitted p-polarized component for an s-polarized incidence in the forward direction. It is noteworthy that in spite of the fact that the incident wave traverses the rotator first, the wave is transmitted to the far-field through the subwavelength slit. Thus, the resultant spatial features are mainly determined by the spoof SPs at the exit interface that is in coincidence with the theory of gratings with subwavelength slits. As expected, it is very similar to what is shown in Fig. 3.7(a). The symmetry with respect to 0° is observed also in this case, while FWHM $\simeq$ 12°. For s-polarized backward propagating waves, numerical results (not shown) suggest that the transmission vanishes since spoof SPs cannot be excited at the input side of the metallic grating.

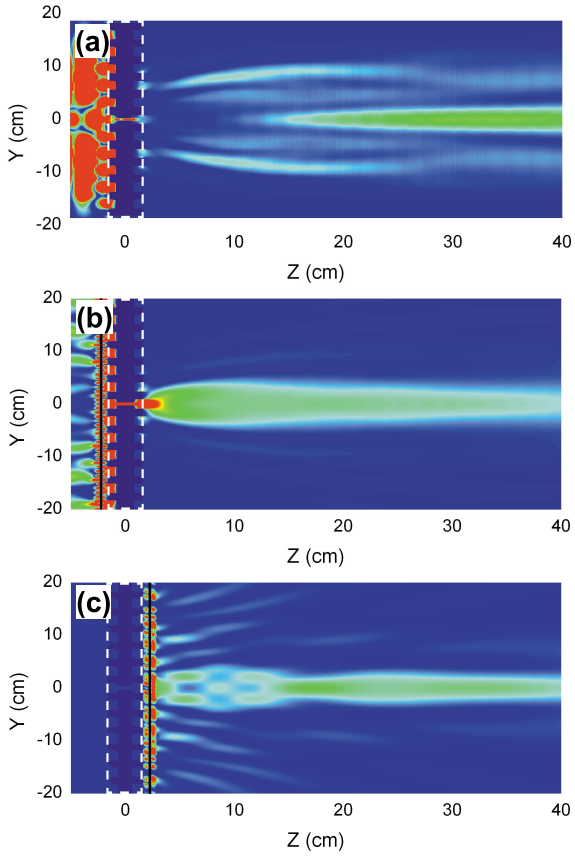

Figure 3.8: Field intensity distributions of p-polarized components for (a) the only grating for p-polarized incidence, (b) the composite structure for s-polarized forward propagating waves, and (c) field intensity distribution of the s-polarized component for p-polarized backward propagating waves. The grating with a subwavelength slit is enclosed in a dashed white rectangle and the position of the rotator is shown by a black line. Reprinted with permission from [39]. Copyright 2013 by the American Physical Society.

Now let us consider the case when the composite structure is illuminated by a p-polarized wave that propagates in the backward direction, being impinged normally on the metallic grating. In this case, the beaming regime is preserved even though the transmission to the farfield is performed by the polarization rotator, yielding an outgoing wave with a dominant s-polarized component, $|t^b_{sp}|$. Fig. 3.7(c) shows the angular distribution of the intensity of the transmitted s-polarized component. It is noteworthy that the propagating waves between the polarization rotator and the metallic grating are generally not plane waves with flat phasefronts. However, also in this case, the chiral structure provides the

desired rotation while the beaming effect is preserved. In this case, similar to the previous angular distributions, we obtain FWHM $\simeq 12^{\circ}$. It should be noted that, in the backward propagation case, simulation results (not shown here) suggest a nonsymmetric angular distribution with respect to 0° for the nonsymmetric placement of the rotator with respect to the yz-plane at $x = 0$. In the backward illumination case, the symmetric placement of the rotator is a significant factor for the obtaining of a symmetric angular distribution, since the outgoing waves are transmitted to the farfield by the rotator. Furthermore, we observe from the simulation results (not shown here) that transmission vanishes for a p-polarized incident wave propagating in the forward direction.

In addition to the angular intensity distributions, we provide the spatial intensity distribution inside the simulation domain, for the same cases shown in Fig. 3.7, in Fig. 3.8 for the purpose of stressing the observed beaming effect. Namely, Fig. 3.8(a), (b), and (c) show the intensity distribution of p-polarized outgoing waves for p-polarized incidence for only grating, p-polarized outgoing waves for s-polarized incidence for the forward propagation, and s-polarized outgoing waves for p-polarized incidence for the backward propagation cases, respectively. In Figs. 3.7 and 3.8, the intensity distributions for the following cases are not shown since the transmission is found to be negligibly small: (i)s- polarized incidence for only grating, (ii)p-polarized incidence for the forward propagation, and (iii)s-polarized incidence for the backward propagation. The existence of low transmission for these cases is going to be verified by using the experimental results in the next section.

According to Figs. 3.7 and 3.8, if a cross-polarized wave is transmitted at s-polarized incidence for forward propagation and p-polarized incidence for backward propagation, the transmission occurs in the beaming regime, i.e., the transmitted beam is localized within desired angular regions of the exit half-space. It is expected that the diode-like operation in the beaming regime will be obtained by combining this observation with the satisfaction of the following conditions at

the operating frequency:

$$|t^f_{ij}| \ll |t^f_{ps}|, \text{ where } (i,j) \neq (p,s). \tag{3.41a}$$

$$|t^b_{ij}| \ll |t^b_{sp}|, \text{ where } (i,j) \neq (s,p). \tag{3.41b}$$

In addition, Figs. 3.7 and 3.8 show that beaming can appear for both forward and backward illumination in the presence of the polarization rotator, but at different polarization states of the incident wave. Indeed, according to Fig. 3.3, the studied mechanism shows the reversibility of the direction of the diode-like asymmetric transmission, which is implied by Lorentz reciprocity, can be an advantage for practical applications, and may not be present in nonreciprocal systems. Importantly, in this paper, it is demonstrated in the beaming regime. It is seen that the transmission direction of the composite structure can be reversed by a simple change of the incident polarization from s- to p-polarization and vice versa.

3.4.2 Experimental results and discussion

3.4.2.1 Experimental Transmission Results

An extended experimental study has been performed in order to validate the expected asymmetry in transmission at normal incidence, see the experiment layout shown in Fig. 3.4(c). Consideration is restricted here to the zero observation angle, which corresponds to the main plane wave component of the angular spectrum of the outgoing beam. As it will be shown subsequently, variation of d allows for controlling the spectra of $|t_{ij}|$.

Figure 3.9 presents the forward transmission spectra, $|t^f_{ij}|$. The measurements have been conducted for four values of d as shown in the legend of Fig. 3.9(a). Two typical cases can be distinguished. For large d, i.e., $d = 100$ mm, the dip of $|t^f_{pp}|$ is located at $f = f_{PR} = 6.98$ GHz, see Fig. 3.9(a). For small d, $d \ll \lambda_{PR}$, the local minimum of $|t^f_{pp}|$ is shifted to approximately 7.05 GHz. In the latter

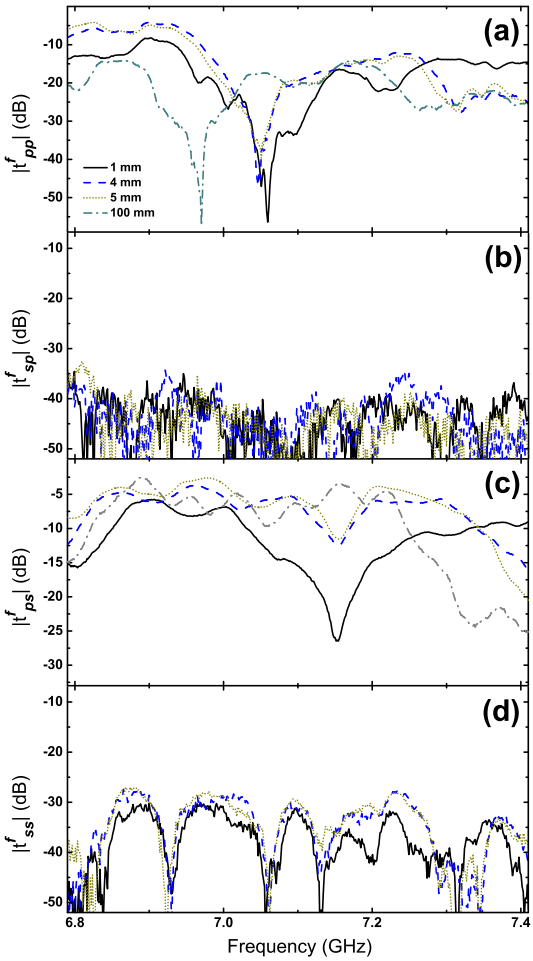

Figure 3.9: Experimental (a),(d) co-polarized and (b), (c) cross-polarized $|t^f_{ij}|$ spectra. The investigated d values are given in the legend of plot (a). Reprinted with permission from [39]. Copyright 2013 by the American Physical Society.

case, the interaction of the evanescent waves created by the resonant rotator and the exponentially decaying (in the z direction) spoof SP field at the metal/air interface takes place, leading to the upshift of the resonance frequency. In fact, this indicates the creation of a coupled resonance mode when the distance between these two structures is smaller than the decay lengths of the evanescent fields. It is seen that the shift of the dip in $|t^f_{pp}|$ is significant even when d is decreased from 5 mm to 1 mm. In the former case, the grating and the rotator are not near-field coupled since $d \simeq 2.3\ \lambda_{PR}$ and thus, the resonance is found at f_{PR}. As expected, both $|t^f_{sp}|$ and $|t^f_{ss}|$ are very small throughout the frequency range of

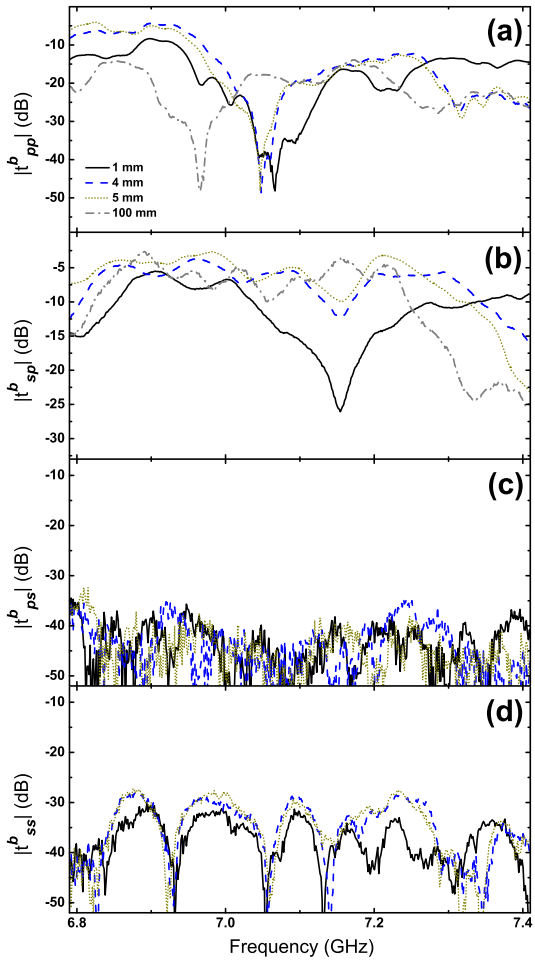

Figure 3.10: Experimental (a),(d) co-polarized and (b), (c) cross-polarized $|t^b_{ij}|$ spectra. The investigated d values are given in the legend of plot (a). Reprinted with permission from [39]. Copyright 2013 by the American Physical Society.

the measurements, see Figs. 3.9(b) and 3.9(d).

According to Fig. 3.9(c), the cross-polarization conversion (from s- to p-polarization) is strong in a wide frequency range, while ET of the p-polarized wave, which is created by the polarization rotator, is well pronounced. The spectrum of $|t^f_{ps}|$ exhibits maxima in the range that includes the vicinity of 6.98 GHz. In reducing the distance between the grating and the rotator, the near-field coupling effects become more pronounced and a transmission dip appears at $f \simeq$ 7.15 GHz. As seen in Fig. 3.9(c), the dip originating due to the near-field coupling is the most significant when $d = 1$ mm. In this case, the cross-polarization

conversion almost disappears.

The experimental backward transmission spectra, $|t^b_{ij}|$, are shown in Fig. 3.10. According to the presented results, the reciprocity assumption for the composite structure is validated, which states that $|t^f_{pp}| = |t^b_{pp}|$, $|t^f_{ss}| = |t^b_{ss}|$, $|t^f_{sp}| = |t^b_{ps}|$, and $|t^f_{ps}| = |t^b_{sp}|$, see the discussion in Sec. 3.4.1.1. Among the possible reasons of the very small differences between the corresponding $|t^f_{ij}|$ and $|t^b_{ij}|$ spectra, one should mention the diffraction effects from the sharp edges, multi-reflections inside the experiment region, and human related alignment errors, such as the possible small displacement of an antenna between the $|t^f_{ij}|$ and $|t^b_{ij}|$ measurements.

The obtained results together show that the conditions given in Eq. 3.41, which are required for the obtaining of the diode-like beaming feature, are satisfied in the regimes where $|t^f_{pp}| \ll |t^f_{ps}|$ (Fig. 3.9) and $|t^b_{pp}| \ll |t^b_{sp}|$ (Fig. 3.10), as occurs in the vicinity of $f = 6.98$ GHz for $d = 100$ mm and in the vicinity of $f \simeq 7.05$ GHz for $d \ll \lambda_{PR}$. Hence, in the above mentioned regimes, the reversibility feature of the composite structure is apparent such that the transmission only occurs at p-polarization for s-polarized incident waves in the forward direction and at s-polarization for p-polarized incident waves in the backward direction.

3.4.2.2 Choice of Operation Frequency

As follows from the transmission results shown in Figs. 3.9 and 3.10, the obtaining of maximal cross-polarized components ($|t^f_{ps}|$ and $|t^b_{sp}|$), on the one hand, and minimal co-polarized components ($|t^f_{pp}|$ and $|t^b_{pp}|$), which is necessary to obtain the desired cross-polarization conversion in transmission, on the other hand, do not necessarily occur at the same frequency as a consequence of near-field coupling for $d \ll \lambda_{PR}$. In other words, the maximum axial ratio and the maximum cross-polarized transmission do not occur at the same frequency for such d values. Thus, the operation frequency should be properly selected on the compromise basis. For the sake of definiteness, we use the data in Fig. 3.10, which correspond to the backward transmission case. First, the axial ratio $|t^b_{sp}|/|t^b_{pp}|$ must be evaluated. Using the obtained result of this evaluation, a figure-of-merit (FOM) can be

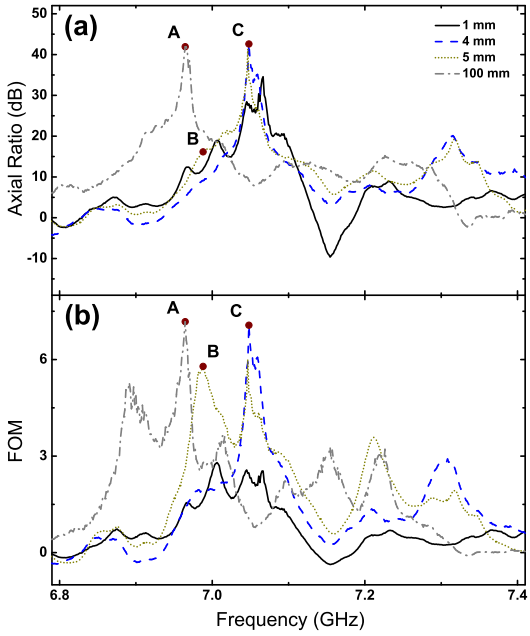

Figure 3.11: (a) Experimental axial ratio of the transmitted waves and (b) the FOM parameter obtained from Eq. (3.42). Reprinted with permission from [39]. Copyright 2013 by the American Physical Society.

introduced as follows:

$$\mathrm{FOM} = -\frac{\log_{10}\left(|t^b_{sp}|/|t^b_{pp}|\right)}{\log_{10}\left(|t^b_{sp}|\right)}. \tag{3.42}$$

Particularly, a larger FOM is achieved for the same axial ratio, but larger cross-polarized transmission. Similarly, we obtain a larger FOM for the same cross-polarized transmission, but larger axial ratio. Furthermore, the defined FOM parameter can be considered as a measure of the forward-to-backward transmission ratio (FBTR). Specifically, in the cases where $|t^b_{pp}| \ll |t^b_{sp}|$ (or $|t^f_{pp}| \ll |t^f_{ps}|$), one would expect obtaining a large FOM value. Considering the regimes, in which $|t^f_{pp}|$ and $|t^b_{pp}|$ are negligibly small, we obtain the following:

$$\mathrm{FBTR}^s \simeq |t^f_{ps}|/|t^b_{ps}|, \tag{3.43a}$$

$$\mathrm{FBTR}^p \simeq |t^b_{sp}|/|t^f_{sp}|, \tag{3.43b}$$

where the superscript of FBTR denotes the polarization state of the incident wave. For instance, using Eq. 3.43, we obtain $\mathrm{FBTR}^s \simeq \mathrm{FBTR}^p \simeq 40$ dB for $d = 5$ mm and 6.95 GHz $\leq f \leq$ 7.08 GHz.

According to the discussion in the previous paragraph, the FOM parameter may serve as a measure of optimization. If desired, FOM for the forward transmission case can be evaluated by replacing $|t^b_{sp}|$ with $|t^f_{ps}|$ and $|t^b_{pp}|$ with $|t^f_{pp}|$ in Eq. 3.42. As an implication of Lorentz reciprocity, the two FOM spectra are expected to be equal within the tolerance of experimental errors.

Figure 3.11 shows the evaluated axial ratio together with the FOM calculated according to the aforementioned definition. The three best pronounced peaks in the FOM spectra are denoted by A, B, and C. They are located at 6.98 GHz, 6.99 GHz, and 7.05 GHz, respectively. The first peak denoted by A corresponds to the vanishing co-polarized transmission that occurs at $f = f_{PR}$ and for $d = 100$ mm, i.e., when near-field coupling between the grating and the rotator is not present. The main disadvantage of this case is the large electrical thickness of the composite structure, which is now approximately 3.1λ. The peak denoted by B ($d = 5$ mm) corresponds to the maximum cross-polarized transmission among all the d values. On the other hand, the axial ratio is approximately 16 dB in this case, so that it might provide a reasonable compromise between strong cross-polarized transmission and large axial ratio. It is noteworthy that at the peak B in Fig. 3.11, $|t^b_{sp}| = -2.8$ dB. The remaining peak, denoted by C ($d = 4$ mm), corresponds to the resonance that is strongly shifted due to the creation of a coupled resonance mode. In this case, an axial ratio of 42 dB is achieved, i.e., it is rather close to that for the peak A, whereas $|t^b_{sp}| \simeq -6$ dB. Accordingly, $|t^{b,5mm}_{sp}|/|t^{b,4mm}_{sp}| \simeq 1.45$. A decision in favor of one of the three operation frequencies should depend on the requirements on concrete performance. For the peaks B and C, the electrical thickness of the composite structure is approximately 0.92λ and 0.90λ, respectively. Thus, the reversible diode-like beaming can be achieved in a compact performance that is thinner than one free-space wavelength.

Chapter 4

Asymmetric Transmission Using Chiral Metamaterials

4.1 Introduction

Simultaneous breaking of time reversal and spatial inversion symmetries has been considered as necessary for nonreciprocal transmission in volumetric structures, enabling the obtaining of $w(\mathbf{k}) \neq w(-\mathbf{k})$ while involving anisotropic constituents [74, 75]. The possibility of nonreciprocal light propagation owing to the symmetry of the parity-time operator has also been studied, for example, in two-channel structures with a properly chosen symmetry of the complex refractive index [76]. At the same time, there were attempts to achieve asymmetric but still reciprocal transmission while using conventional isotropic, linear and low-loss/lossless materials. Among them, the asymmetric transmission of linearly polarized waves in diffractive nonsymmetrical volumetric gratings based on photonic [57] and sonic [60] crystals, or made of ultralow-index materials [61], and in nonsymmetrical metallic gratings supporting surface plasmons [29, 55] should be mentioned. The asymmetric transmission of circularly polarized waves has

been demonstrated at normal incidence in thin structures composed of meta-atoms [62–64, 77]. A thin structure composed of three-dimensional meta-atoms without any rotational symmetry has been suggested that allows asymmetric transmission for an arbitrary, also linear, polarization of the incident electromagnetic wave [65].

In this chapter, we first briefly discuss the subject of reciprocity in bianisotropic media and derive the condition required for a reciprocal response. Then, we briefly discuss the phenomenon of asymmetric transmission. Next, we show the achievement of asymmetric transmission and incident polarization plane angle dependent polarization rotation in an asymmetric metamaterial. We finalize the chapter by demonstrating the achievement of diodelike strongly asymmetric transmission in a tri-layer metamaterial structure.

4.2 Reciprocity in Bianisotropic Media

Understanding the origin of the asymmetric transmission phenomenon requires a fundamental understanding of reciprocity in bianisotropic media. First of all, the constitutive relations inside a bianisotropic medium can be written as follows [78]:

$$\begin{pmatrix} c\mathbf{D} \\ \mathbf{H} \end{pmatrix} = \begin{pmatrix} \bar{P} & \bar{L} \\ \bar{M} & \bar{Q} \end{pmatrix} \begin{pmatrix} \mathbf{E} \\ c\mathbf{B} \end{pmatrix}, \tag{4.1}$$

where c is the speed of light. In Eq. 4.1, $\mathbf{E}$, $\mathbf{H}$, $\mathbf{D}$, and $\mathbf{B}$ denote the field vectors. The elements $\bar{P}$, $\bar{L}$, $\bar{M}$, and $\bar{Q}$ are matrices with dimensions equal to that of admittance. By rearranging the terms of Eq. 4.1, one can easily express $\mathbf{D}$ and $\mathbf{B}$ as follows:

$$\mathbf{D} = \frac{1}{c}\left(\bar{P} - \bar{L}\cdot\bar{Q}^{-1}\cdot\bar{M}\right)\cdot\mathbf{E} + \frac{1}{c}\bar{L}\cdot\bar{Q}^{-1}\cdot\mathbf{H}, \tag{4.2a}$$

$$\mathbf{B} = -\frac{1}{c}\bar{Q}^{-1}\cdot\bar{M}\cdot\mathbf{E} + \frac{1}{c}\bar{Q}^{-1}\cdot\mathbf{H}. \tag{4.2b}$$

For the sake of simplicity, we can write $\mathbf{D}$ and $\mathbf{B}$ vectors as

$$\mathbf{D} = \bar{\epsilon} \cdot \mathbf{E} + \bar{\varsigma} \cdot \mathbf{H}, \tag{4.3a}$$

$$\mathbf{B} = \bar{\upsilon} \cdot \mathbf{E} + \bar{\mu} \cdot \mathbf{H}. \tag{4.3b}$$

In Eq. 4.3, $\bar{\epsilon}$, $\bar{\varsigma}$, $\bar{\upsilon}$, and $\bar{\mu}$ can be evaluated as follows:

$$\bar{\epsilon} = \frac{1}{c}\left(\bar{P} - \bar{L} \cdot \bar{Q}^{-1} \cdot \bar{M}\right), \tag{4.4a}$$

$$\bar{\varsigma} = \frac{1}{c}\bar{L} \cdot \bar{Q}^{-1}, \tag{4.4b}$$

$$\bar{\upsilon} = -\frac{1}{c}\bar{Q}^{-1} \cdot \bar{M}, \tag{4.4c}$$

$$\bar{\mu} = \frac{1}{c}\bar{Q}^{-1}. \tag{4.4d}$$

Using Eq. 4.3 and the following two Maxwell equations for time-harmonic waves

$$\nabla \times \mathbf{E} = -jw\mathbf{B}, \tag{4.5a}$$

$$\nabla \times \mathbf{H} = jw\mathbf{D} + \mathbf{J}, \tag{4.5b}$$

we can write

$$\nabla \times \mathbf{E} = -jw\bar{\upsilon} \cdot \mathbf{E} - jw\bar{\mu} \cdot \mathbf{H}, \tag{4.6a}$$

$$\nabla \times \mathbf{H} = jw\bar{\epsilon} \cdot \mathbf{E} + jw\bar{\varsigma} \cdot \mathbf{H} + \mathbf{J}. \tag{4.6b}$$

In the reaction theorem, assuming the magnetic current density is zero, the reaction terms are defined as follows [37]:

$$<a, b> = \int_V \mathbf{E}_a \cdot \mathbf{J}_b \; dV, \tag{4.7a}$$

$$<b, a> = \int_V \mathbf{E}_b \cdot \mathbf{J}_a \; dV. \tag{4.7b}$$

In Eq. 4.7, $<a, b>$ relates the reaction (coupling) of the field $\mathbf{E}_a$, which is produced by the source $\mathbf{J}_a$, to the source $\mathbf{J}_b$, which produces the field $\mathbf{E}_b$. Similarly, $<b, a>$ relates the reaction (coupling) of the field $\mathbf{E}_b$, which is produced by the

source $\mathbf{J}_b$, to the source $\mathbf{J}_a$, which produces the field $\mathbf{E}_a$. Lorentz reciprocity theorem states that

$$<a, b> = <b, a> \tag{4.8}$$

in isotropic media. Additionally, Eq. 4.8 is also valid for anisotropic media with symmetrical $\bar{\epsilon}$ and $\bar{\mu}$ tensors [37]. However, it is absolutely not valid for bianisotropic media. In order to obtain a reciprocity relation for bianisotropic media, one first needs to define a complementary medium.

From this point on, we will benefit from the theoretical paper written by Kong and Cheng [79] until the end of this section. In that paper, the corresponding complementary medium is characterized by the following constitutive relations:

$$\mathbf{D}^c = \bar{\epsilon}^T \cdot \mathbf{E}^c - \bar{\upsilon}^T \cdot \mathbf{H}^c, \tag{4.9a}$$

$$\mathbf{B}^c = -\bar{\varsigma}^T \cdot \mathbf{E}^c + \bar{\mu}^T \cdot \mathbf{H}^c. \tag{4.9b}$$

Compared to Eq. 4.3, the following changes are observed in Eq. 4.9: $\bar{\epsilon} \rightarrow \bar{\epsilon}^T$, $\bar{\varsigma} \rightarrow -\bar{\upsilon}^T$, $\bar{\upsilon} \rightarrow -\bar{\varsigma}^T$, and $\bar{\mu} \rightarrow \bar{\mu}^T$. Note that the letter c in the superscripts denotes that the corresponding field is defined inside the complementary medium. Correspondingly, the reaction terms for the complementary medium can be defined in a similar way to Eq. 4.7 as follows:

$$<a, b>^c = \int_V \mathbf{E}_a^c \cdot \mathbf{J}_b \, dV, \tag{4.10a}$$

$$<b, a>^c = \int_V \mathbf{E}_b^c \cdot \mathbf{J}_a \, dV. \tag{4.10b}$$

Furthermore, by combining Eqs. 4.5 and 4.9, we can write

$$\nabla \times \mathbf{E}^c = jw\bar{\varsigma}^T \cdot \mathbf{E}^c - jw\bar{\mu}^T \cdot \mathbf{H}^c, \tag{4.11a}$$

$$\nabla \times \mathbf{H}^c = jw\bar{\epsilon}^T \cdot \mathbf{E}^c - jw\bar{\upsilon}^T \cdot \mathbf{H}^c + \mathbf{J}. \tag{4.11b}$$

Now, firstly, we will take the dot product of every term in Eq. 4.6(a) with $\mathbf{H}_a^c$. We will use the fields created by $\mathbf{J}_b$, namely $\mathbf{E}_b$ and $\mathbf{H}_b$. The resultant equation

is given by

$$\mathbf{H}_a^c \cdot \nabla \times \mathbf{E}_b = -jw\mathbf{H}_a^c \cdot \bar{\upsilon} \cdot \mathbf{E}_b - jw\mathbf{H}_a^c \cdot \bar{\mu} \cdot \mathbf{H}_b. \tag{4.12}$$

If we now take Eq. 4.11(b) for $\mathbf{E}_a^c$ and $\mathbf{H}_a^c$, and multiply every term by $\mathbf{E}_b$ from the left, the following is obtained:

$$\mathbf{E}_b \cdot \nabla \times \mathbf{H}_a^c = jw\mathbf{E}_b \cdot \bar{\epsilon}^T \cdot \mathbf{E}_a^c - jw\mathbf{E}_b \cdot \bar{\upsilon}^T \cdot \mathbf{H}_a^c + \mathbf{E}_b \cdot \mathbf{J}_a. \tag{4.13}$$

Subtracting Eq. 6.78 from Eq. 6.79 yields

$$\nabla \cdot (\mathbf{H}_a^c \times \mathbf{E}_b) = jw(\mathbf{E}_a^c \cdot \bar{\epsilon} \cdot \mathbf{E}_b + \mathbf{H}_a^c \cdot \bar{\mu} \cdot \mathbf{H}_b) + \mathbf{E}_b \cdot \mathbf{J}_a. \tag{4.14}$$

It is noteworthy that we use the vector identities $\mathbf{B} \cdot (\nabla \times \mathbf{A}) - \mathbf{A} \cdot (\nabla \times \mathbf{B}) = \nabla \cdot (\mathbf{A} \times \mathbf{B})$ and $\mathbf{A} \cdot \bar{x} \cdot \mathbf{B} = \mathbf{B} \cdot \bar{x}^T \cdot \mathbf{A}$ in order to arrive to Eq. 4.14.

Similar to what is done previously, we first take Eq. 4.11(a) for $\mathbf{E}_a^c$ and $\mathbf{H}_a^c$, and multiply every term by $\mathbf{H}_b$ from the left. As a result, we obtain the following relation:

$$\mathbf{H}_b \cdot \nabla \times \mathbf{E}_a^c = jw\mathbf{E}_a^c \cdot \bar{\varsigma} \cdot \mathbf{H}_b - jw\mathbf{H}_a^c \cdot \bar{\mu} \cdot \mathbf{H}_b. \tag{4.15}$$

Taking Eq. 4.6(b) for $\mathbf{E}_b$ and $\mathbf{H}_b$, and multiplying every term by $\mathbf{E}_a^c$ from the left yields

$$\mathbf{E}_a^c \cdot \nabla \times \mathbf{H}_b = jw\mathbf{E}_a^c \cdot \bar{\epsilon} \cdot \mathbf{E}_b + jw\mathbf{E}_a^c \cdot \bar{\varsigma} \cdot \mathbf{H}_b + \mathbf{E}_a^c \cdot \mathbf{J}_b. \tag{4.16}$$

By subtracting Eq. 4.15 from Eq. 4.16, we obtain

$$\nabla \cdot (\mathbf{H}_b \times \mathbf{E}_a^c) = jw(\mathbf{E}_a^c \cdot \bar{\epsilon} \cdot \mathbf{E}_b + \mathbf{H}_a^c \cdot \bar{\mu} \cdot \mathbf{H}_b) + \mathbf{E}_a^c \cdot \mathbf{J}_b. \tag{4.17}$$

Next, we subtract Eq. 4.14 from Eq. 4.17 and obtain

$$\mathbf{E}_a^c \cdot \mathbf{J}_b - \mathbf{E}_b \cdot \mathbf{J}_a = \nabla \cdot (\mathbf{H}_b \times \mathbf{E}_a^c - \mathbf{H}_a^c \times \mathbf{E}_b). \tag{4.18}$$

By taking the volume integral of both sides and employing the divergence theorem, we can rewrite Eq. 4.18 in the following form:

$$\int_V (\mathbf{E}_a^c \cdot \mathbf{J}_b - \mathbf{E}_b \cdot \mathbf{J}_a)\, dV = \oint_S (\mathbf{H}_b \times \mathbf{E}_a^c - \mathbf{H}_a^c \times \mathbf{E}_b) \cdot d\mathbf{S}. \tag{4.19}$$

The right-hand side of Eq. 4.19 is equal to zero if the bounding surface S goes to infinity or the volume V is enclosed in a PEC. In such cases, by using Eqs. 4.7 and 4.10, we are left with

$$<b, a> = <a, b>^{c} \tag{4.20}$$

Finally, by interchanging a and b in Eq. 4.19, one can easily show that

$$<a, b> = <b, a>^{c}. \tag{4.21}$$

Note that Eqs. 4.20 and 4.21 states that the classical reciprocity, which is shown in Eq. 4.8, does not hold for bianisotropic structures. Instead, the reaction of one set of sources on another in a bianisotropic medium is equal to the reaction of the latter set on the former in a complementary medium [79].

Now, assume that we have two infinitely large current sheets (sources) creating perfect plane waves. We place a bianisotropic medium between these sources. The forward propagating electric field created by source 1 traverses the medium and creates a reaction current on source 2. Now, the reciprocity theorem presented here states that the bianisotropic medium behaves as its complementary one when the incident field is backward propagating. Thereby, the reaction current induced on source 1 is similar to that induced on source 2.

According to Eq. 4.6(a), the initial $\mathbf{E}$ field is rotated upon propagation due to the term $-jw\bar{v} \cdot \mathbf{E}$. In a similar manner, the initial $\mathbf{H}$ field is rotated due to the term $jw\bar{\varsigma} \cdot \mathbf{H}$, see Eq. 4.6(b). These terms are the origin of the optical activity observed in bianisotropic media. On the other hand, Eq. 4.11 states that the rotations of the initial $\mathbf{E}$ and $\mathbf{H}$ fields are due to the terms $jw\bar{\varsigma}^{T} \cdot \mathbf{E}^{c}$ and $-jw\bar{v}^{T} \cdot \mathbf{H}^{c}$ in the complementary medium. Note that the cross-coupling terms are interchanged, transposed, and multiplied by -1. Along with the discussion in the previous paragraph, this observation implies that, if the linear transmission matrix for forward propagation is given by

$$T_{lin}^{f} = \begin{pmatrix} T_{xx} & T_{xy} \\ T_{yx} & T_{yy} \end{pmatrix}, \tag{4.22}$$

then, the linear transmission matrix for backward propagation is

$$T^b_{lin} = \begin{pmatrix} T_{xx} & -T_{yx} \\ -T_{xy} & T_{yy} \end{pmatrix}. \tag{4.23}$$

This relationship between T^f and T^b is observed in all chiral metamaterials that are composed of linear and reciprocal constituents [15]. Using Eqs. 2.9, 4.22, and 4.23, it can easily be shown that, if the forward circular transmission matrix is defined as

$$T^f_{circ} = \begin{pmatrix} T_{++} & T_{+-} \\ T_{-+} & T_{--} \end{pmatrix}, \tag{4.24}$$

reciprocity imposes that the backward one is

$$T^b_{circ} = \begin{pmatrix} T_{++} & T_{-+} \\ T_{+-} & T_{--} \end{pmatrix}. \tag{4.25}$$

4.3 Asymmetric Transmission

We have shown in Eqs. 4.22 and 4.23 that the cross-coupling terms in the linear transmission matrix are interchanged for forward and backward transmission matrices. This difference between T^f_{lin} and T^b_{lin} is crucial for the achievement of asymmetric transmission. Briefly, one can define asymmetric transmission as the difference of the transmitted powers for backward and forward propagating incident waves. Note that the polarization states of the two waves must be identical.

Now, let us assume an x-polarized forward propagating incident wave with a unity electric field amplitude. Obviously, the transmitted wave in this case is expressed as $(T_{xx}; T_{yx})$. The transmitted power is equal to $P^f = |T_{xx}|^2 + |T_{yx}|^2$ since the orthogonal electric fields in the x and y directions cannot interfere with each other. Similarly, for a backward propagating x-polarized incident wave, we have $(T_{xx}; -T_{xy})$ and the transmitted power is given by $P^b = |T_{xx}|^2 + |T_{xy}|^2$. The difference between the transmitted powers, i.e., degree of asymmetric transmission, is given by

$$\Delta_{lin} = P^f - P^b = |T_{yx}|^2 - |T_{xy}|^2. \tag{4.26}$$

In a similar manner, one can easily calculate that

$$\Delta_{circ} = P^f - P^b = |T_{-+}|^2 - |T_{+-}|^2 \tag{4.27}$$

in the case of illumination by forward and backward propagating RCP waves. If the cross-polarized terms of a transmission matrix in a particular base are not equal, this may result in $\Delta \neq 0$ and asymmetric transmission can be observed.

Note that in the general case $\Delta_{circ} \neq \Delta_{lin}$ and the degree of asymmetric transmission should be calculated separately for every incident wave polarization state. One can observe a significant asymmetric transmission for one incident wave polarization state, whereas asymmetric transmission may not exist for another state. It is very counterintuitive that a transmission contrast resulting from the asymmetric transmission phenomenon can be achieved in a reciprocal medium. Note that asymmetric transmission is a completely reciprocal effect.

4.4 Polarization Angle Dependent Rotation

It was recently shown that a carefully designed metamaterial reflector can be utilized in order to rotate the polarization of a wave [27]. However, due to the reflection based operation, the reflected wave and the incoming wave interfere, which causes the design to be inconvenient for practical applications. Consequently, transmission based polarization rotators have been proposed [10, 29, 81]. Those structures exhibit remarkable polarization rotation efficiencies in the vicinity of their operation frequencies. However, for rotationally asymmetric structures operating as polarization rotators, transmitted waves are elliptically polarized for certain polarization angles [29]. On the other hand, for rotationally symmetric polarization rotators, the amount of rotation is independent of the polarization angle of the incident wave [10]. In order to overcome these limitations, in the

present section, we study the potential of an electrically thin polarization rotator, whose rotatory power is polarization dependent, i.e., the linear transmission coefficients are dependent on the polarization angle of the incoming wave. As a consequence, the proposed chiral metamaterial (CMM) also exhibits an asymmetric transmission of linearly polarized waves at 6.2 GHz. Asymmetric transmission of electromagnetic waves is an optical phenomenon that has been studied for different structures in several studies [62, 64, 65, 77]. Using the theoretical calculations, we obtained four polarization angles for which the transmission of the structure is symmetric. In order to have linearly polarized eigenwaves for the CMM, we optimized the phases of the transmitted waves, so that any linearly polarized wave can be transmitted as a linearly polarized wave.

Such a design can be utilized in order to dynamically control the polarization-mode dispersion (PMD) in optical communication systems [82], modify the polarization of a laser output arbitrarily and dynamically, obtain an arbitrary linear polarization from a steady antenna and scan certain polarization directions in order to characterize the response of a certain material to different incident polarizations. The proposed CMM can be integrated into a rotating stage to easily obtain the desired polarization state by simple rotation of the stage with respect to the analytical description provided in the subsequent sections. In addition, the proposed CMM can be stacked while avoiding the coupling effects [83] in order to obtain a larger rotation than one layer can provide.

4.4.1 Proposed Geometry

In order to obtain asymmetric transmission and incident wave polarization angle dependent polarization rotation, the CMM structure that is composed of four U-shaped split ring resonator (SRR) pairs is a good candidate [4, 25, 84]. It is possible to introduce asymmetry by altering the dimensions of certain SRR pairs. As a result, illuminating the structure by an incident wave polarized in a certain direction is not equivalent to illuminating the structure from the opposite direction by a wave with the same polarization state. The introduction of such an asymmetry also breaks the fourfold rotational C_4 symmetry. Thus, circularly

polarized waves are not eigenwaves of the proposed design. This fact can be used as an advantage for the purpose of creating polarization angle dependent rotation. As a consequence of the broken C_4 symmetry, orthogonal electric field components (x and y components in this context) of an incident wave encounter different transmission coefficients, both in terms of magnitude and phase. This discrepancy between the transmission coefficients can be optimized to yield a linearly polarized transmitted wave whose polarization angle is a function of the polarization angle of the linearly polarized incident wave. In this study, we demonstrate the results of this optimization numerically and experimentally. Afterwards, a closed form relationship is derived that relates the polarization rotation introduced by the CMM to the polarization angle of the incident wave.

The unit cell of the proposed CMM structure is depicted in Fig. 4.1. It is an asymmetric version of the structure that has been studied in Refs. [4, 25, 84]. In a previous study, it has been demonstrated that a similar variant of this design operates as a circular polarizer for incident waves that are linearly polarized in the x-direction [17]. For the circular polarizer, the coupling between the meta-atoms has been optimized in order to provide maximum wave ellipticity in the vicinity of the resonance frequencies as to ensure that the transmitted wave is circularly polarized. Conversely, the design goal in this study is minimizing the transmitted wave ellipticity as to rotate a linearly polarized incident wave without distorting the linearity of the polarization.

The following geometrical parameters for the unit cell are used in the simulations and experiments: $a_x = a_y = 13.6$ mm, $s_1 = 6$ mm, $s_2 = 4.8$ mm, $w_1 = 0.7$ mm, $w_2 = 0.55$ mm, $d = 1.4$ mm, and $t = 1.5$ mm. A FR-4 board with a relative permittivity of 4 and a dielectric loss tangent of 0.025 is utilized as the substrate. For the metallic parts, copper that is 30 μm thick is used. As it will be presented subsequently, the operating frequency of the CMM is 6.2 GHz. At this frequency, the structure is electrically thin with $t/\lambda \approx 0.031$. In addition, the periodicity in the transverse plane is electrically small at 6.2 GHz, since $a_x = a_y$ corresponds to 0.281λ.

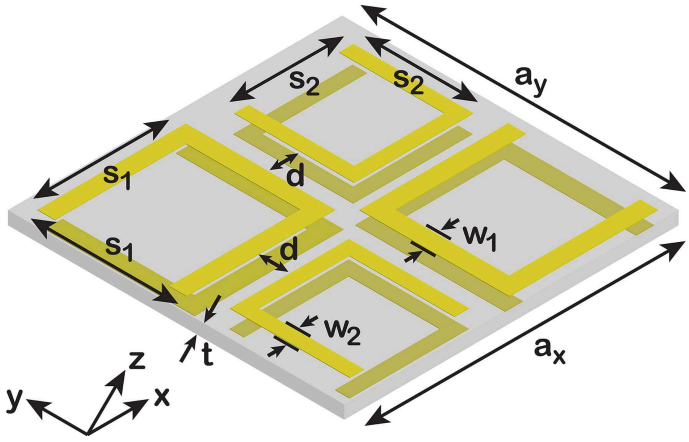

Figure 4.1: Geometry of the simulated and fabricated chiral metamaterial unit cell. Reprinted with permission from [80]. Copyright 2011 by the Optical Society of America.

4.4.2 Numerical Results

We initiated the analysis with numerical simulations of the proposed CMM unit cell using CST Microwave Studio (Computer Simulation Technology AG, Germany), which is a commercially available software that utilizes the finite integration method. During the simulations, boundary conditions along the x and y directions are adjusted to be periodic in order to obtain periodicity in the transverse plane. The boundary condition along the z direction is selected to be absorbing. In order to characterize the response of the CMM, the structure is illuminated by plane waves propagating in the z direction. Assuming the linearity of the CMM, linear transmission coefficients T_{xx} and T_{yx} are obtained from the simulations when the incident wave is x-polarized. Similarly, for a y-polarized incident wave, linear transmission coefficients T_{xy} and T_{yy} are obtained. The magnitudes of the four linear transmission coefficients are shown in Figs. 4.2(a) and 4.2(b). The mutual phase differences between T_{xx} and T_{yx}, and T_{yy} and T_{xy} are shown in Fig. 4.2(c).

Using Fig. 4.2, it is observed that the CMM creates an electric field that is orthogonal to the incident field, since the cross-coupling terms T_{xy} and T_{yx} are non-zero. In addition, the simulation results reveal that T_{xx} and T_{yy} are equal in terms of magnitude and phase (phase not shown here). In other words,

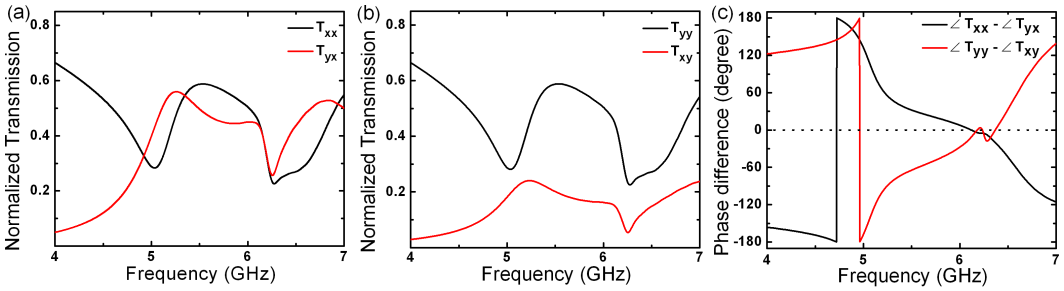

Figure 4.2: Magnitudes of the linear transmission coefficients when the CMM is illuminated by (a) x-polarized and (b) y-polarized incident waves. (c) The mutual phase differences between the transmission coefficients. Reprinted with permission from [80]. Copyright 2011 by the Optical Society of America.

the transmitted x-polarization due to an x-polarized incidence is equal in terms of magnitude and phase to the transmitted y-polarization due to a y-polarized incidence. Conversely, it is noticed that the transmitted y-polarization due to an x-polarized incidence is strongly different than the transmission of the x-polarization due to a y-polarized incidence. Using these observations, it can be deduced that this CMM configuration creates polarization angle dependent chirality.

The asymmetric transmission of the structure is also explicable using the linear transmission coefficients. Due to the geometry, illuminating the structure by a plane wave polarized in the y-direction and propagating in the z direction is equivalent to illumination by a plane wave polarized in the x-direction and propagating in the $+z$ direction. The two waves encounter the same transmission coefficients with respect to their polarization direction, e.g., T_{xx} becomes T_{yy} and T_{yx} becomes T_{xy}. Thus, the transmission of the CMM is asymmetric.

Figure 4.2(c) shows the mutual phase differences between T_{xx} and T_{yx}, and T_{yy} and T_{xy}. At 6.2 GHz, which is the operating frequency of the device, the mutual phase differences are approximately equal to 0°, in turn demonstrating that at this frequency optical activity is observed. Although the mutual phase differences are 0°, the phases of all the elements must be equal in order to avoid the transmission of elliptically polarized wave. We investigated the numerical results and observed that at 6.2 GHz, the phases of all linear transmission coefficients are equalized.

As a result, combining the two orthogonal cases, linearly polarized waves are eigenwaves of the CMM at 6.2 GHz and are transmitted with a polarization rotation.

Thereafter, circular transformation coefficients [17] are calculated using

$$C_x^{\pm} = T_{xx} \mp iT_{yx}, \qquad C_y^{\pm} = T_{yy} \pm iT_{xy} \tag{4.28}$$

for the two separate incident polarizations. In order to characterize the polarization of the transmitted wave, the polarization azimuth rotation angle θ is calculated using the formula

$$\theta_{x,y} = \arg(C_{x,y}^{+}) - \arg(C_{x,y}^{-}) \tag{4.29}$$

and the ellipticity of the transmitted wave, which is defined as

$$\eta_{x,y} = \tan^{-1}\left(\frac{|C_{x,y}^{+}| - |C_{x,y}^{-}|}{|C_{x,y}^{+}| + |C_{x,y}^{-}|}\right) \tag{4.30}$$

is determined. The results retrieved from the simulations for the polarization rotations and the transmitted wave ellipticities are shown in Fig. 4.3. In Fig. 4.3(a), it is observed that the ellipticities of the transmitted waves for x-polarized and y-polarized incident fields are approximately equal to zero at 6.2 GHz, which corresponds to pure optical activity at this frequency. The corresponding azimuth polarization rotation angles for x-polarized and y-polarized incident fields are shown in Fig. 4.3(b).

According to the results given in Fig. 4.3(b), an incident wave that is linearly polarized in the x direction is rotated by 46° at 6.2 GHz, whereas a y-polarized incident wave is rotated by 15° at the same frequency. Due to different rotations for x and y polarizations, each incident polarization angle encounters a different rotation. The relationship between the incident polarization angle and the resulting polarization rotation can be derived by performing simple geometrical calculations based on the rotation values provided above. However, for simplicity, we will employ the transfer matrix formulation subsequently for determining this relation.

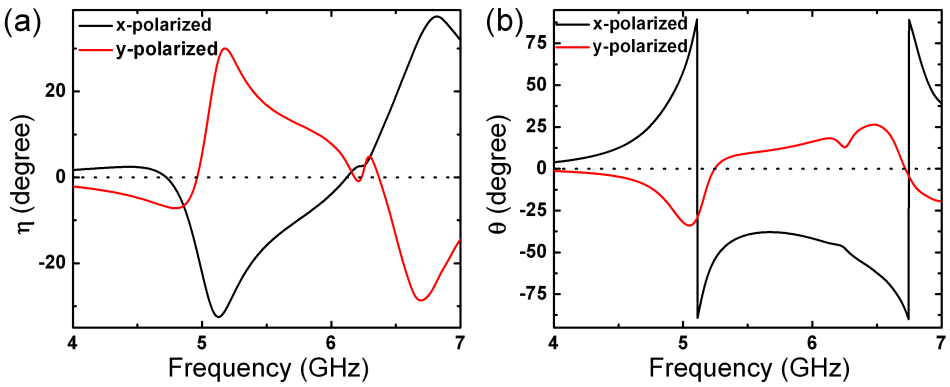

Figure 4.3: (a) Ellipticities and (b) polarization azimuth rotation angles of the transmitted waves for x-polarized and y-polarized illumination. Reprinted with permission from [80]. Copyright 2011 by the Optical Society of America.

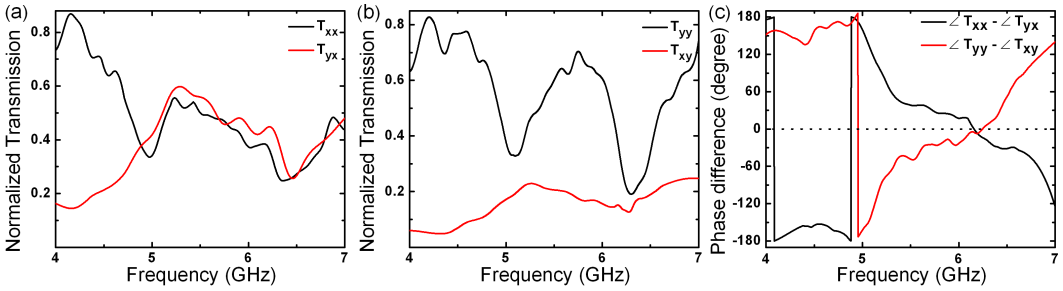

Figure 4.4: (a) Experimental magnitudes of T_{xx} and T_{yx}, and (b) T_{xy} and T_{yy}. (c) Mutual phase differences obtained from the experiments. Reprinted with permission from [80]. Copyright 2011 by the Optical Society of America.

4.4.3 Experimental Results

In order to characterize the behavior of the CMM and examine the validity of the simulation results, we performed experiments. We fabricated the structure with a dimension of 16 by 16 unit cells. The experiment is conducted using two standard horn antennas facing each other at a 60 cm distance. The structure is placed in the middle between the antennas. The transmission coefficients are measured using an HP-8510C network analyzer (Agilent Technologies, USA).

The x and y components of the transmitted fields due to x- and y-polarized incident waves are measured for characterization. Phase information is also obtained from the network analyzer in order to calculate the rotation and ellipticity

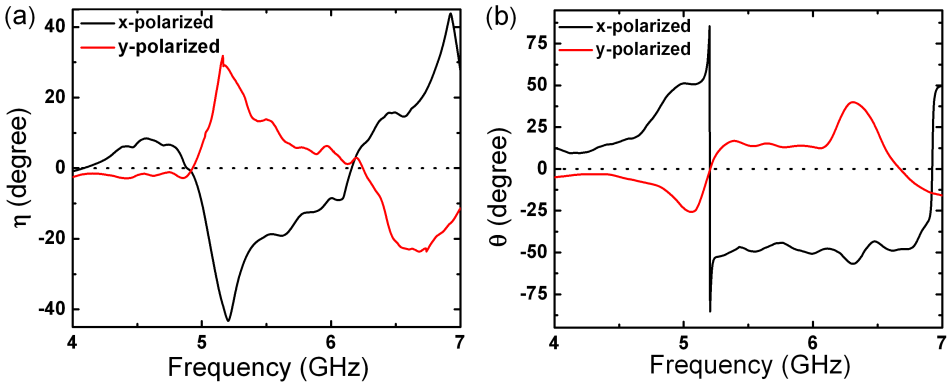

Figure 4.5: (a) Experimental ellipticies and (b) polarization rotations of the transmitted waves due to x- and y-polarized incident waves. Reprinted with permission from [80]. Copyright 2011 by the Optical Society of America.

for the transmitted waves. The experimental magnitudes of T_{xx}, T_{xy}, T_{yx}, and T_{yy} are shown in Fig. 4.4, as well as the phase differences between T_{xx} and T_{yx}, and T_{yy} and T_{xy}. In Fig. 4.2(c), the phase differences are approximately equal to 0° at 6.2GHz. For the experiment results, at 6.2 GHz we obtain $-6°$ for the phase difference between T_{xx} and T_{yx} and $-7°$ for the T_{yy} and T_{xy} case. Throughout the scanned frequency range, the experiment results agree closely with the simulations.

In addition to the transmission results, we extracted the ellipticity and polarization rotation information from the measurement data. These results are shown in Fig. 4.5, which is the experimental analog of Fig. 4.3. At 6.2 GHz, the ellipticity of a transmitted wave due to an x-polarized incidence is 4.2°. Similarly, for a y-polarized incident wave, the ellipticity of the transmitted wave is 2.9°. These results are very close to the numerical results, where both ellipticities are approximately equal to 0°. Subsequently, we examine the experimental results for polarization rotation. Experiment results indicate that the amount of rotation is 49° for an x-polarized incident wave at 6.2 GHz. This value differs by 3° from the simulation results, which indicates a good agreement. However, we obtain a 26° rotation for a y-polarized wave at the same frequency. Numerical results provided 15° rotation for a y-polarized field, which differs by 11° from the experiment result. These discrepancies can be attributed to the inaccuracies

in the fabrication stage, multi-reflections in the experiment setup, diffraction effects from the sharp edges of the CMM structure, probable misalignments, and non-zero cross-polarization response of the antennas. In addition, the resonance frequencies slightly shift to higher frequencies in the experiments. The possible reasons are the variance of the dielectric permittivity of the FR-4, experiment inaccuracies, and simulation inaccuracies, i.e., mesh size affects the resonance frequencies. Overall, we conclude that the agreement between the numerical and experiment results is good and the operation of the CMM is verified experimentally.

4.4.4 Formulation

Assuming that the CMM structure is a two-input and two-output system, where the fields associated with the x and y directions represent the two inputs and the two outputs of the system, a transmission matrix T, with the elements T_{xx}, T_{xy}, T_{yx}, and T_{yy} can be defined so that the following relation holds

$$\begin{pmatrix} E_{xd} \\ E_{yd} \end{pmatrix} = \begin{pmatrix} T_{xx} & T_{xy} \\ T_{yx} & T_{yy} \end{pmatrix} \begin{pmatrix} E_{x0} \\ E_{y0} \end{pmatrix}, \tag{4.31}$$

where E_{xd} and E_{yd} are the transmitted fields along the x and y directions, respectively. Similarly, E_{x0} and E_{y0} represent the electric field components of the incident field along the x and y directions. In linear equation form, Eq. 4.31 can be rewritten as the follows:

$$E_{xd} = T_{xx}E_{x0} + T_{xy}E_{y0}, \tag{4.32a}$$

$$E_{yd} = T_{yx}E_{x0} + T_{yy}E_{y0}. \tag{4.32b}$$

Subsequent to the calculation of transmitted x and y components for an arbitrary input to the system, the polarization angle of the transmitted wave is calculated as

$$\phi = \tan^{-1}\left(\frac{T_{yx}E_{x0} + T_{yy}E_{y0}}{T_{xx}E_{x0} + T_{xy}E_{y0}}\right). \tag{4.33}$$

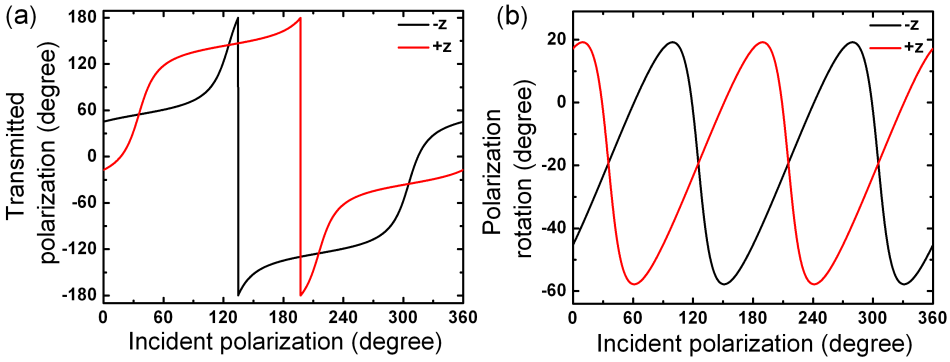

Figure 4.6: (a) Polarization angles of the transmitted linearly polarized waves with respect to the polarization angle of the incident wave, at 6.2 GHz, for the z and $+z$ propagating waves. (b) Introduced polarization rotation to the z and $+z$ propagating waves with respect to the incident polarization angle, at 6.2 GHz. Reprinted with permission from [80]. Copyright 2011 by the Optical Society of America.

In order to relate the transmitted polarization angle to the incident polarization angle, without loss of generality, we assume that the magnitude of the incoming wave is unity in all cases. Under this assumption, Eq. 4.33 is modified as

$$\phi = \tan^{-1}\left(\frac{T_{yx}\cos\varphi + T_{yy}\sin\varphi}{T_{xx}\cos\varphi + T_{xy}\sin\varphi}\right), \tag{4.34}$$

where φ denotes the polarization angle of the incident wave. It is noteworthy that the inverse tangent is a multi-valued function that requires special attention. The quadrant where ϕ lies depends on the signs of the numerator and denominator of Eq. 4.34. Finally, the corresponding polarization rotation is defined as

$$\theta = \varphi - \phi. \tag{4.35}$$

Then, to calculate the polarization rotation introduced by the CMM at 6.2 GHz, we constructed the transmission matrices using the simulation results for waves propagating in the z and $+z$ directions. Thereby, the asymmetric transmission of the design would be demonstrated simultaneously with the incident polarization angle dependent polarization rotation. For an incident wave propagating in the z direction, the elements of the transmission matrix are given as $T_{xx} = 0.3568$, $T_{xy} = 0.1104$, $T_{yx} = 0.3599$, and $T_{yy} = 0.3568$. In general, these elements are

complex quantities carrying phase information. However, in this case we omit the phases of the elements, since the simulation and experiment results prove that all the elements are in-phase. Thus, using only the magnitude information is sufficient. Similarly, for a $+z$ propagating wave, the transmission matrix elements are given as $T_{xx} = 0.3568$, $T_{xy} = 0.3599$, $T_{yx} = 0.1104$, and $T_{yy} = 0.3568$. The two transmission matrices demonstrate the asymmetric transmission of the structure, since T_{xy} and T_{yx} values are not equal for the $+z$ and z cases. Figure 4.6(a) shows the calculated polarization angle of the transmitted wave, using Eq. 4.34, due to incident waves linearly polarized from 0° to 360° and propagating in the $-z$ and $+z$ directions. The corresponding polarization rotation calculated using Eq. 4.35 is presented in Fig. 4.6(b).

As it is apparent in Fig. 4.6(a), at several angles, $-z$ and $+z$ propagating waves are transmitted symmetrically, with the same polarization. Equating ϕ given by Eq. 4.34 for the above-mentioned transmission matrices, we obtain the following transcendental equation to calculate these angles:

$$\tan^{-1}\left(\frac{0.3599\cos\varphi + 0.3568\sin\varphi}{0.3568\cos\varphi + 0.1104\sin\varphi}\right) = \tan^{-1}\left(\frac{-0.1104\cos\varphi + 0.3568\sin\varphi}{0.3568\cos\varphi - 0.3599\sin\varphi}\right). \tag{4.36}$$

Numerical solution for Eq. 4.36 yields $\varphi = 35.3°$, $125.3°$, $215.3°$, and $305.3°$. Figure 4.6(b) presents θ as a function of ϕ, which is calculated using Eqs. 4.34 and 4.35.

It is seen that the proposed CMM is reciprocal, i.e., it shows the same θ for the waves propagating in the $-z$ and $+z$ directions, which are linearly polarized at the angles those are being equal to the solutions of Eq. 4.36. In turn, for polarization angles, which do not satisfy Eq. 4.36, the transmission is asymmetric, i.e., different for waves propagating in the $-z$ and $+z$ directions. In both cases, linearly polarized waves are eigenwaves for both directions.

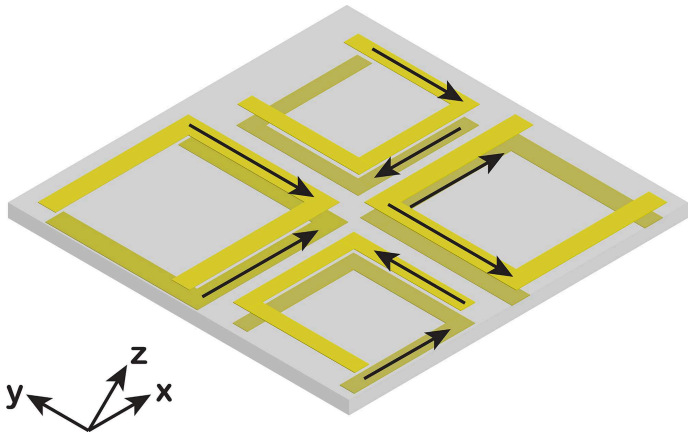

Figure 4.7: Directions of the induced surface currents due to x-polarized plane waves propagating in the z and $+z$ directions at 6.2 GHz. Reprinted with permission from [80]. Copyright 2011 by the Optical Society of America.

4.4.5 Surface Currents

In order to explain the asymmetric transmission, we investigated the induced surface currents at 6.2 GHz, when the CMM is excited by x-polarized waves propagating in the z and $+z$ directions. The simulation results indicate that the directions of the induced surface currents are identical for both excitations. The directions of the surface currents are shown in Fig. 4.7.

As the next step, we have simulated a single SRR pair, where one SRR is rotated by 90° with respect to the other. We observed that coupling from the x polarization to the y polarization decreases when the electric field vector of the incident wave is parallel to the slit of the SRR that is closer to the source. However, rotating the pair by 90°, while keeping the electric field vector direction constant, does not change the transmission of the x polarization. In the case where each SRR pair has the same dimensions, rotation does not affect the transmission coefficients. In the asymmetric case, rotation decreases coupling from x polarization to y-polarization, whereas the transmission of the x-polarization is not changed. When the structure is rotated, smaller SRR pairs are not at the resonance since their resonance frequencies are larger. In addition, according to the simulation results, larger SRR pairs begin to produce less y polarization compared to the previous case. Thus, illuminating the structure by an x-polarized

wave is not equivalent to illumination by a y-polarized wave. It should also be denoted that due to the geometry of the CMM, illuminating the structure by a y-polarized wave propagating in the z direction is equivalent to illuminating it by an x-polarized wave propagating in the $+z$ direction. Hence, as a result of different transmission coefficients for the x and y polarized waves, the transmission of the structure is asymmetric.

4.5 Diodelike Asymmetric Transmission

In this section, we propose a new, ultrathin, three-layer structure made of isotropic and linear materials, which enables a diode-like asymmetric transmission of certain linearly polarized, normally incident waves. Nearly total transmission is demonstrated in cross-polarization regime in one direction, while the transmission in the opposite direction at the same polarization of the incident wave is blocked. Possible applications include microwave and optical isolation, integrated photonic circuits, ultrafast information processing, and optical interconnects [85]. To our knowledge, diodelike asymmetric transmission of linearly polarized waves at normal incidence has not been observed before. In fact, it requires the diagonal components and one of the off-diagonal components of the Jones matrix to be zero, while the only non-zero element must be approximately unity for maximum efficiency. These requirements are not easily achievable, also in a chiral structure, without the support of additional physical mechanisms, in our case the utilization of elliptical eigenstates and the tunneling of electromagnetic waves.

4.5.1 General Idea

The exploited physical mechanism is based on the combination of the coupling of electric and magnetic fields in mutually rotated split ring resonator (SRR)

pairs [8] and electromagnetic wave tunneling through a metallic subwavelength mesh [32]. Tunneling is an exciting phenomenon that utilizes the potential of nonpropagating waves in transmission. Unlike the previous experience of utilizing the tunneling effect [32], we perform an ABC stacking type instead of an ABA type. Layers A and C are, in fact, the same layers which are rotated by $\pm\pi/2$ with respect to each other. Layer B is a subwavelength mesh that acts as a negative permittivity medium throughout the interested frequency range independent of the polarization. Because of the inclusion of layer B, the phase difference between the transmission coefficients of the eigenwaves of the ABC stack may be properly optimized, yielding a strong modification in the transmission, i.e. enhancement of one of the two off-diagonal (cross-polarized) components of the Jones matrix (T_{xy}) and suppression of all the others (T_{xx}, T_{xy}, T_{yy}). As a result, strongly asymmetric, diode-like transmission takes place for the incident waves that are linearly polarized in the x or y directions. Similar to Refs. [62–65,77], asymmetric transmission in the suggested structure is a completely reciprocal phenomenon.

One of the main ideas behind the proposed design is choosing two layers, which do not exhibit C_4 symmetry, as Layer A and C. In addition, these layers must be chosen such that they exhibit strong optical activity when brought together. Accordingly, we choose the separate layers of the metamaterial structure given in Ref. [80] as Layer A and C.

Adopting the Jones matrix formalism, we relate the electric field amplitudes of incident (I_x, I_y) and transmitted (T_x, T_y) fields [65], for the $+z$ (forward) propagation as follows:

$$\begin{pmatrix} T_x^f \\ T_y^f \end{pmatrix} = \begin{pmatrix} T_{xx}^f & T_{xy}^f \\ T_{yx}^f & T_{yy}^f \end{pmatrix} \begin{pmatrix} I_x^f \\ I_y^f \end{pmatrix} = \begin{pmatrix} \delta & \gamma \\ \beta & \delta \end{pmatrix} \begin{pmatrix} I_x^f \\ I_y^f \end{pmatrix}. \tag{4.37}$$

Then, for the $-z$ (backward) propagation, we have

$$\begin{pmatrix} T_x^b \\ T_y^b \end{pmatrix} = \begin{pmatrix} \delta & -\beta \\ -\gamma & \delta \end{pmatrix} \begin{pmatrix} I_x^b \\ I_y^b \end{pmatrix}. \tag{4.38}$$

According to Eqs. 4.37 and 4.38, if $I_y^f = I_y^b = 0$ (x-polarized incident wave) and

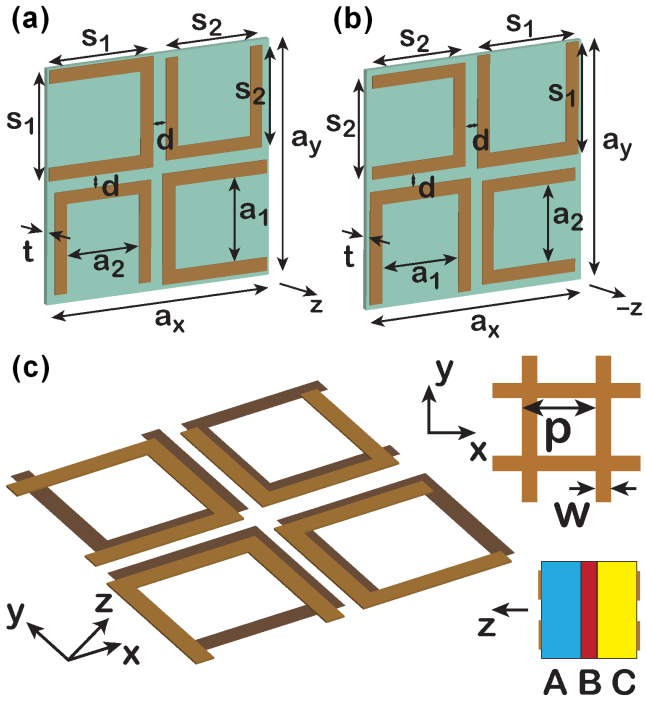

Figure 4.8: Geometries of (a) layer A and (b) layer C. (c) Arrangement of A and C with respect to each other along with the mesh geometry and the stacking scheme. Reprinted with permission from [66]. Copyright 2013 by the American Physical Society.

$\delta = 0$, all transmitted energy corresponds to the nondiagonal (cross-polarized) elements, leading to a strongly asymmetric transmission if these elements are significantly different in magnitude. Diodelike asymmetric transmission also occurs when $I_x^f = I_x^b = 0$. However, in this case, the direction of the strong transmission should be reversed. Next, we will demonstrate that almost all the incident wave energy can be converted to that of the cross-polarized transmitted wave for one of the incidence directions, while it is largely reflected for the opposite direction, so that a diodelike behavior occurs. In the ideal case, one must obtain $\gamma = 1$ and $\beta = 0$. For the purposes of this study, we seek for the regimes with $\gamma \approx 1$ and $\beta \ll \gamma$.

4.5.2 Method

The unit cell of the proposed structure that is assumed to be periodic in the transverse plane is depicted in Fig. 4.8. It is composed of three distinct layers that are referred to as Layer A, B and C. Fig. 4.8(a) and 4.8(b) shows Layer A and Layer C, respectively. They both contain four U-shaped SRRs and show the lack of C_4 symmetry due to the involvement of the SRRs of different dimensions. The arrangement of layers A and C, and the scheme of stacking are presented in Fig. 4.8(c) together with the geometry of Layer B. In the arrangement of A and C, the SRRs of the same dimensions are paired together. Layer B is positioned symmetrically between A and C. The geometric parameters for Layer B are given by $w = 0.5$ mm and $p = 2.56$ mm. The geometric parameters of both layers A and C are given by $s_1 = 6$ mm, $a_1 = 4.6$ mm, $s_2 = 5.52$ mm, $a_2 = 4.23$ mm, $d = 0.64$ mm, $t = 1$ mm and $a_x = a_y = 12.8$ mm. Teflon dielectric substrates with a relative dielectric permittivity of 2.1 and a loss tangent of 0.0002 are utilized for the layers A and C. Layer B is considered to be a stand-alone metallic structure with a thickness of 20 μm. The metal utilized for the structure of the SRRs and the mesh is copper with a 20 μm thickness. The total thickness of the structure is 2.06 mm, which corresponds to $\lambda/21$ at 7 GHz while $a_x/\lambda \approx 0.3$.

We started the analysis with numerical simulations using CST Microwave Studio (Computer Simulation Technology, AG, Germany), by using periodic boundary conditions along the x and y directions and an open boundary condition for the z direction, while the excitation source is an x-polarized plane wave. Then, in order to experimentally verify the diodelike transmission, we fabricated the structure with the dimension of 23 by 23 unit cells. The experiment was conducted using two standard horn antennas facing each other at a 50 cm distance. The sample is positioned in the middle between the antennas. The transmission coefficient measurements are performed using an HP-8510C network analyzer (Agilent Technologies, USA). For the experimental characterization of the structure, the transmitted fields for the forward and backward propagating incident waves are studied in terms of the transmission coefficients T_{xx} and T_{yx}.

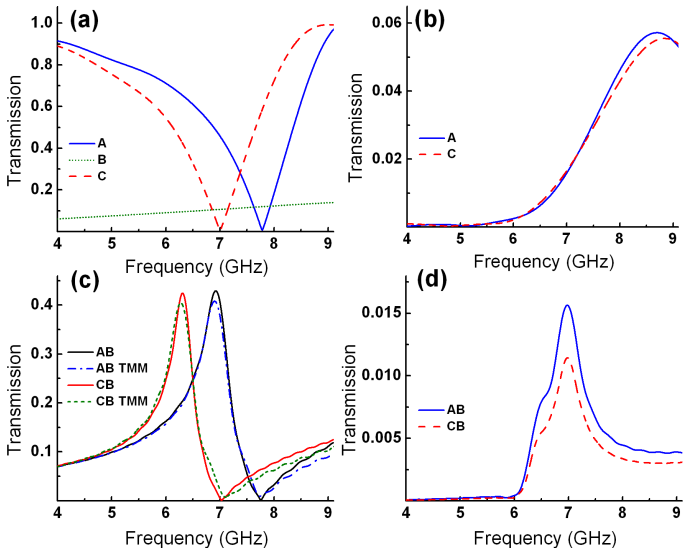

Figure 4.9: $|T_{xx}|$ for (a) separate and (c) double layers, and $|T_{yx}|$ for the same (b) separate and (d) double layers. Reprinted with permission from [66]. Copyright 2013 by the American Physical Society.

4.5.3 Results and Discussion

As the first step, we studied the responses of the single layers, A, B, and C. Figures 4.9(a) and 4.9(b) show $|T_{xx}|$ and $|T_{yx}|$, respectively. We see in Fig. 4.9(a) that Layer A is resonant at 7.7 GHz whereas the resonance frequency is 7 GHz for Layer C. Field distributions (not shown) reveal that at the resonance frequency, the responses of the layers are governed by the SRRs that have slits parallel to the direction of the electric field. In the case of Layer C, such SRRs are larger which implies that their resonance frequency is lower. Figure 4.9(b) shows that the $|T_{yx}|$ values of layers A and C show maxima at around 8.5 GHz. However, $|T_{yx}|$ does not exceed 0.06, indicating that the coupling between electric and magnetic fields in the transverse plane is relatively weak. The small difference in $|T_{yx}|$ values for layers A and C is caused by the weak symmetry breaking of the substrate [86].

The numerical results of the AB and CB cases are presented in Fig. 4.9(c) for $|T_{xx}|$ and in Fig. 4.9(d) for $|T_{yx}|$. Using Fig. 4.9(c), we observe transmission bands at 6.2 GHz and 7 GHz for the AB and CB cases, respectively. Moreover, the frequencies of zero transmissions are not modified by adding Layer B. Noting that $|T_{yx}|$ is negligible compared to $|T_{xx}|$ in these cases, we can approximately model

the transmission of AB and CB utilizing the transfer matrix method (TMM), while assuming the eigenwaves to be linearly polarized, i.e., similarly to Ref. [32]. Using the effective medium theory (EMT), for x-polarized incident waves, we characterize the separate layers as homogenous dielectric slabs with $\epsilon_{\mathrm{A}} = 5.67 + 252/(7.78^2 - f^2)$, $\epsilon_{\mathrm{B}} = 3.65 - 55.7^2/f^2$, and $\epsilon_{\mathrm{C}} = 6.33 + 286/(7^2 - f^2)$ where f is the frequency in GHz. The effective thickness required to reproduce the simulated magnitude and phase values is 1.22 mm for layers A and C, and 1.5 mm for layer B. The results obtained from the TMM calculations are shown in Fig. 4.9(c) and are in excellent agreement with the simulations. At the same time, we observe a peak at 7 GHz for $|T_{yx}|$; see Fig. 4.9(d). In order to theoretically describe $|T_{yx}|$ using EMT, one should determine the elliptically polarized eigenwaves for layers A and C and retrieve the effective permittivity for each eigenwave. Afterwards, TMM calculations should again be performed.

Thereafter, we simulated the composite structure with ABC stacking-type. The numerical results reveal that increasing the distance between the layers decreases $|T_{xy}|$ as a result of the decreased evanescent-wave coupling. Thus, one should not leave any air gaps. The numerical and experimental results that demonstrate the diodelike asymmetric transmission phenomenon are shown in Fig. 4.10. According to these results, the frequency of the diodelike transmission is 7 GHz. In Fig. 4.10(c), it is observed that $|T_{yx}|$ approaches unity for the backward propagating waves, whereas $|T_{xx}|$ is close to zero for both propagation directions. In turn, Fig. 4.10(a) shows that only 10% of the incident field is transmitted when the structure is excited by a forward propagating wave. To be exact, $|T_{xx}|$ is approximately 0.03, and $|T_{yx}|$ is 0.1 and 0.98 for the forward and backward propagating waves, respectively. These parameters provide 1.09% intensity transmission for the forward propagation and 96.1% intensity transmission for the backward propagation. These values correspond to the contrast of 88 (19.5 dB), which is obtained as the ratio of the two transmitted intensities. For the backward propagation, the magnetic field distribution inside the composite structure (not shown) that is similar to the one given in Ref. [32] reveals the occurrence of the electromagnetic tunneling due to the high magnetic fields (see Fig. 2 in Ref. [32]). The transmission of the composite ABC structure can also be

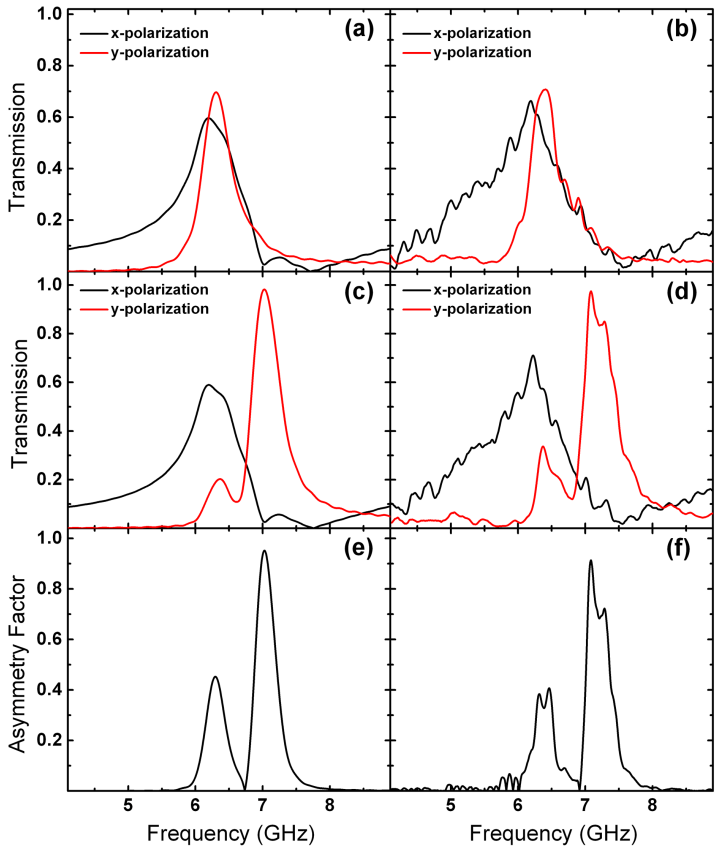

Figure 4.10: Numerical and experimental transmission spectra for the ABS stack, for x-polarized (a), (b) forward and (c), (d) backward propagating waves; (e), (f) numerical and experimental asymmetry factor. Reprinted with permission from [66]. Copyright 2013 by the American Physical Society.

modeled using EMT as we have done for the AB and CB cases. However, in the composite case, the eigenwaves are elliptically polarized, so that significant effort is needed to accurately apply the EMT framework. Instead, subsequently, we will describe the behavior of the structure in terms of the eigenstate interpretation.

According to Fig. 4.10, the experiment results are in good agreement with the numerical results, except for a slight shift of the frequency of the maximal asymmetry (7.1 GHz). The possible reasons for this shift can include (i) the difference of the effective permittivity of the Teflon substrate from the simulations, (ii) the small differences in substrate and metal thicknesses, and (iii) the finite size effects. Experimental data show that $|T_{xx}| = 0.141$ and $|T_{xx}| = 0.171$ for a forward propagating wave. These transmission coefficients yield 4.9% intensity

transmission at 7.1 GHz. On the other hand, for the backward propagation, we obtain that $|T_{xx}| = 0.112$, whereas $|T_{xx}| = 0.974$, which corresponds to 96% intensity transmission. Hence, the experimental contrast is 19.6 (13 dB).

In this context, the *asymmetry factor* is defined as $|T^b_{xx}|^2 + |T^b_{yx}|^2 - |T^f_{xx}|^2 - |T^f_{yx}|^2$. We demonstrate the asymmetry factor of the structure for an x-polarized incident wave numerically and experimentally in Figs. 4.10(e) and 4.10(f), respectively. In particular, one can see two peaks of the asymmetry factor that are positioned at 6.3 GHz and 7 GHz. Such behavior is quite expectable while these two frequencies correspond to the transmission peaks of $|T_{yx}|$, where the transmitted intensity difference is maximized as a result of increasing difference between the forward and backward $|T_{yx}|$ values. The simulation results state a 0.45 and 0.95 asymmetry factor at 6.3 GHz and 7 GHz, respectively. Experimental results show great agreement in terms of the asymmetry factor, which is now of 0.38 at 6.3 GHz and 0.91 at 7.1 GHz. The direction of diodelike transmission is reversed for a y-polarized wave as is obvious from Eqs. 4.37 and 4.38. The asymmetry factor is strongly dependent on the incident polarization and has its maximum for the x- and y-polarized waves. On the other hand, the asymmetry factor is zero for an incident wave that is linearly polarized at 45°, meaning complete symmetry in transmission.

4.5.4 Eigenstate Interpretation

For the achievement of diode-like asymmetric transmission, the Jones matrix descriptions in Eqs. 4.37 and 4.38 state that $T_{xx} = T_{xy} = T_{yy} = 0$ and $T_{yx} = -1$ must be achieved for backward propagation. However, using the present ABC-type stacking approach, the transmission matrix for backward propagation is achieved as

$$T = \begin{pmatrix} 0 & -\alpha e^{j\varphi} \\ -1 & 0 \end{pmatrix}, \tag{4.39}$$

where $\alpha = 0.1$. As it will be demonstrated subsequently, φ does not affect the magnitudes of the transmission coefficients and therefore, its value is not explicitly

given. Afterwards, the eigenwaves of the ABC structure are found as [15]

$$\mathbf{i}_1 = \begin{pmatrix} 1 \\ \alpha^{-1/2} e^{-j\varphi/2} \end{pmatrix}, \qquad \mathbf{i}_2 = \begin{pmatrix} 1 \\ -\alpha^{-1/2} e^{-j\varphi/2} \end{pmatrix}. \tag{4.40}$$

The eigenstates are orthogonal and counter-rotating elliptically polarized waves. We can define the transmitted waves as $T_1\mathbf{i}_1$ and $T_2\mathbf{i}_2$ when $\mathbf{i}_1$ and $\mathbf{i}_2$ are incident on the structure, respectively. Here, T_1 and T_2 are complex transmission coefficients for the eigenwaves. Next, by decomposing an x-polarized incident field in terms of the eigenwaves of the system, we obtain

$$T \begin{pmatrix} 1 \\ 0 \end{pmatrix} = \frac{1}{2}(T_1\mathbf{i}_1 + T_2\mathbf{i}_2) = \begin{pmatrix} (1/2)(T_1 + T_2) \\ (\alpha^{-1/2}/2)e^{-j\varphi/2}(T_1 - T_2) \end{pmatrix}. \tag{4.41}$$

Thus, for the purpose of achieving $|T_{xx}| = 0$, we need $T_2 = -T_1$. In other words, the two counter-rotating eigenwaves must be transmitted with a phase difference of π. At this point, the phase difference is a critical parameter. The subwavelength mesh in the structure acts as a necessary degree of freedom that enables the obtaining of the desired phase difference between the transmitted eigenwaves. Then, $|T_{yx}|$ is found as $\alpha^{-1/2}|T_1|$ and equal to *unity* at 7 GHz and, therefore, for this frequency, $|T_1| = |T_2| = 0.316$. Electromagnetic tunneling becomes evident as a result of the constructive interference of the transmitted eigenwaves in the y direction. Next, we decompose a y-polarized incident wave in terms of the eigenwaves as follows:

$$T \begin{pmatrix} 0 \\ 1 \end{pmatrix} = \frac{e^{j\varphi/2}}{2\alpha^{-1/2}}(T_1\mathbf{i}_1 - T_2\mathbf{i}_2) = \begin{pmatrix} (\sqrt{a}e^{j\varphi/2}/2)(T_1 - T_2) \\ (1/2)(T_1 + T_2) \end{pmatrix}. \tag{4.42}$$

In that case, $|T_{yy}|$ is equal to zero at 7 GHz. On the other hand, $|T_{xy}|$ is given by $\alpha^{1/2}|T_1|$ and equal to 0.1. Moreover, the ratio between $|T_{yx}|$ and $|T_{xy}|$ is found as α^{-1}, as was expected from Eq. 4.39. Note that, due to Lorentz reciprocity $T^b_{xy} = -T^f_{yx}$. Therefore, we conclude that the presented diodelike asymmetric transmission originates from the common effect of the two counter-rotating elliptically polarized eigenwaves that are transmitted through the structure with a

phase difference of π. The phase difference is of crucial importance since it determines the magnitudes of the co- and cross-polarized transmission. One should choose the eigenwaves such that the magnitude of their component along the y-direction ($\alpha^{-1/2}$) should be as large as possible for maximizing the transmission asymmetry. The calculations based on the Jones matrix formalism reveal that, if $\alpha \ll 1$ is achieved, any structure exhibiting the transmission of the elliptically polarized eigenstates with a phase difference of π would exhibit diodelike asymmetric transmission. It is noteworthy that the modification of the mesh thickness can decrease the asymmetry factor significantly as a consequence of modifying the phase difference between the transmitted eigenstates.

Chapter 5

Guided Waves

5.1 Introduction

This theoretical chapter intends to provide a brief understanding of the guided wave and waveguide concept. Firstly, due to its simplicity, the characteristics of transverse electromagnetic (TEM), transverse magnetic (TM), and transverse electric (TE) waves in the parallel-plate metallic waveguide are studied. Afterwards, we extend our investigation to the TE and TM modes inside the dielectric slab waveguide. Similar to metal based waveguides, dielectric slab waveguides can be utilized to confine the energy of traveling waves into a well-defined cross-section and serve as transmission lines. Finally, benefiting from the dielectric slab waveguide results, we determine the TE and TM fields and their dispersions relation inside the periodic dielectric slab waveguide. This chapter is of fundamental importance for ensuring the comprehensive understanding of the theoretical interpretation of high-contrast gratings, which are simply periodic slab waveguides with finite lengths.

In analyzing the parallel-plate metallic waveguide configuration, we benefit from the theoretical analysis given in Ref. [87]. The theoretical analysis of the dielectric slab waveguide is adapted from Refs. [37,88]. Afterwards, we utilize the fundamentals of the dielectric slab waveguide analysis in order to obtain the field equations and the dispersion relations of the periodic dielectric slab waveguide.

5.2 Parallel-Plate Metallic Waveguide

The parallel-plate metallic waveguide geometry is shown in Fig. 5.1 and is simply composed of two metallic plates that are extending to infinity in x and z directions and are separated by a distance of b. For the purpose of generalization, we assume that the region between the plates is filled with a dielectric with an absolute permittivity of ϵ. For the sake of simplicity, we assume that this dielectric is nonmagnetic ($\mu = \mu_0$), linear, isotropic, homogeneous, lossless ($\epsilon'' = 0$), and not conductive ($\mathbf{J} = 0$) and does not sustain a net charge distribution ($\rho = 0$). Furthermore, it will be assumed that the metals are nonmagnetic ($\mu = \mu_0$) and not able to sustain a charge distribution ($\rho = 0$) and dipole moments ($\mathbf{P} = 0$ and $\mathbf{D} = \epsilon_0\mathbf{E}$). For metals, we can apply Ohm's Law, which states that $\mathbf{J} = \sigma\mathbf{E}$, where σ denotes the conductivity of the corresponding metal. This assumption is valid in the microwave frequencies where $\sigma \to \infty$. At frequencies comparable to the plasma frequency, w_p, metals can be characterized by a dispersive permittivity using the Drude model as follows:

$$\epsilon(w) = 1 - \frac{w_p^2}{w^2 + i\gamma w}, \tag{5.1}$$

where γ is the characteristic collision frequency. The consideration of such frequencies is beyond the scope of this thesis and is not shown here. However, it should be noted that the dielectric slab waveguide interpretation, which is shown in Sec. 5.3, can be used in order to understand the characteristics of parallel-plate waveguides at high frequencies. The main difference for high frequencies is that the fields are now able to penetrate into the metal.

Returning to microwave frequencies, at which metals can be considered as perfect electric conductors, the abovementioned assumptions can be reflected to the Maxwell equations as follows:

$$\nabla \times \mathbf{E} = -iw\mu_0\mathbf{H} \tag{5.2a}$$

$$\nabla \times \mathbf{H} = (\sigma + iw\epsilon)\mathbf{E} \tag{5.2b}$$

$$\nabla \cdot \mathbf{E} = 0 \tag{5.2c}$$

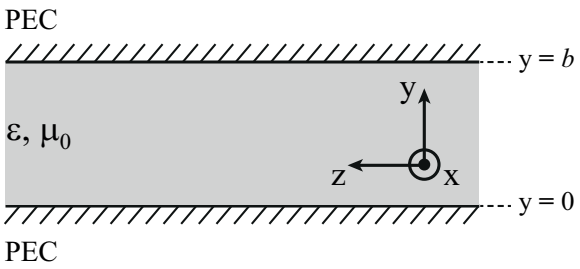

Figure 5.1: Parallel-plate metallic waveguide geometry. The metals are assumed to be perfect electric conductors. The dielectric slab between the two metals is characterized by an absolute permittivity of ϵ and an absolute permeability of μ_0. The structure is assumed to be extending to infinity in the x and z directions. The waveguide modes propagate in the $+z$ direction.

$$\nabla \cdot \mathbf{H} = 0 \tag{5.2d}$$

Application of the vector identity $\nabla \times \nabla \times \mathbf{A} = \nabla(\nabla \cdot \mathbf{A}) - \nabla^2 \mathbf{A}$ to either Eq. 5.2(a) or to Eq. 5.2(b) results in a wavenumber of

$$k^2 = -iw\mu_0(\sigma + iw\epsilon). \tag{5.3}$$

It is seen from Eq. 5.3 that, for a metal, relative permittivity can be expressed in the following form:

$$\epsilon(w) = 1 + i\frac{\sigma}{\epsilon_0 w} \tag{5.4}$$

5.2.1 Rectilinear Propagation

Provided that the dielectric and metal losses are ignored and the propagation is in the $+z$ direction, the assumption of rectilinear (forming a straight line) propagation inside the waveguide is justified. Accordingly, using the superposition principle, electric and magnetic fields can be divided into transverse ($\mathbf{e}_t$ and $\mathbf{h}_t$) and longitudinal ($\mathbf{e}_z$ and $\mathbf{h}_z$) components such that

$$\mathbf{E}(x, y, z) = \mathbf{e}_t(x, y)e^{-i\beta z} + \mathbf{e}_z(x, y)e^{-i\beta z}, \tag{5.5a}$$

$$\mathbf{H}(x,y,z) = \mathbf{h}_t(x,y)e^{-i\beta z} + \mathbf{h}_z(x,y)e^{-i\beta z}, \tag{5.5b}$$

where β is the purely real propagation constant. In rectangular coordinates, taking Eq. 5.5 into account, the Del operator can be written as follows:

$$\nabla = \hat{\mathbf{x}}\frac{\partial}{\partial x} + \hat{\mathbf{y}}\frac{\partial}{\partial y} - \hat{\mathbf{z}}i\beta = \nabla_t - \hat{\mathbf{z}}i\beta, \tag{5.6}$$

where $\hat{\mathbf{x}}$, $\hat{\mathbf{y}}$, and $\hat{\mathbf{z}}$ denote the unit vectors in the corresponding directions and

$$\nabla_t = \hat{\mathbf{x}}\frac{\partial}{\partial x} + \hat{\mathbf{y}}\frac{\partial}{\partial y} \tag{5.7}$$

is the transverse Del operator. Correspondingly, by substituting Eq. 5.5 into Eq. 5.2(a), we obtain the following equation:

$$\nabla_t \times \mathbf{e}_t - i\beta\hat{\mathbf{z}} \times \mathbf{e}_t + \nabla_t \times \mathbf{e}_z = -iw\mu_0\mathbf{h}_t - iw\mu_0\mathbf{h}_z \tag{5.8}$$

Eq. 5.8 can be split into two dependent equations, using the fact that $\nabla_t \times \mathbf{e}_t$ is in the z direction and $\nabla_t \times \mathbf{e}_z - \beta\hat{\mathbf{z}} \times \mathbf{e}_t$ lies in the transverse plane, as follows:

$$\nabla_t \times \mathbf{e}_t = -iw\mu_0\mathbf{h}_z \tag{5.9a}$$

$$\nabla_t \times \mathbf{e}_z - i\beta\hat{\mathbf{z}} \times \mathbf{e}_t = -iw\mu_0\mathbf{h}_t \tag{5.9b}$$

Using the vector identity $\nabla \times (f\mathbf{A}) = f\nabla \times \mathbf{A} + \nabla f \times \mathbf{A}$ and $\mathbf{e}_z = \hat{\mathbf{z}}e_z$ we can rewrite Eq. 5.9(b) in the following form:

$$\hat{\mathbf{z}} \times (\nabla_t e_z + i\beta\mathbf{e}_t) = iw\mu_0\mathbf{h}_t. \tag{5.10}$$

Finally, substitution of Eq. 5.5(a) into Eq. 5.2(c) yields

$$(\nabla_t - i\beta\hat{\mathbf{z}}) \cdot (\mathbf{e}_t + \mathbf{e}_z)e^{-i\beta z} = \nabla_t \cdot \mathbf{e}_t - i\beta e_z = 0. \tag{5.11}$$

By performing the same analysis for $\mathbf{H}$, i.e., substituting Eq. 5.5 into Eq. 5.2(b), we arrive at the following six equations, which are the Maxwell equations for the

rectilinear propagation case:

$$\nabla_t \times \mathbf{e}_t = -iw\mu_0 \mathbf{h}_z \tag{5.12a}$$

$$\nabla_t \times \mathbf{h}_t = iw\epsilon \mathbf{e}_z \tag{5.12b}$$

$$\nabla_t \cdot \mathbf{e}_t = i\beta e_z \tag{5.12c}$$

$$\nabla_t \cdot \mathbf{h}_t = i\beta h_z \tag{5.12d}$$

$$\hat{\mathbf{z}} \times (\nabla_t e_z + i\beta \mathbf{e}_t) = iw\mu_0 \mathbf{h}_t \tag{5.12e}$$

$$\hat{\mathbf{z}} \times (\nabla_t h_z + i\beta \mathbf{h}_t) = -iw\epsilon \mathbf{e}_t \tag{5.12f}$$

5.2.2 TEM Modes

TEM waves are entirely transverse to the direction of propagation such that $\mathbf{e}_z = 0$ and $\mathbf{h}_z = 0$. Accordingly, the rectilinear Maxwell equations take the following form:

$$\nabla_t \times \mathbf{e}_t = 0 \tag{5.13a}$$

$$\nabla_t \times \mathbf{h}_t = 0 \tag{5.13b}$$

$$\nabla_t \cdot \mathbf{e}_t = 0 \tag{5.13c}$$

$$\nabla_t \cdot \mathbf{h}_t = 0 \tag{5.13d}$$

$$\hat{\mathbf{z}} \times \mathbf{e}_t = w\mu_0 \mathbf{h}_t / \beta \tag{5.13e}$$

$$\hat{\mathbf{z}} \times \mathbf{h}_t = -w\epsilon \mathbf{e}_t / \beta \tag{5.13f}$$

It is readily seen from Eq. 5.13(e) and 5.13(f) that the wave impedance, $Z_{\text{TEM}} = |\mathbf{e}_t|/|\mathbf{h}_t| = w\mu_0/\beta$. In addition, for a TEM mode, we have $\beta = \sqrt{\epsilon/\epsilon_0}w/c_0 = \sqrt{\epsilon/\epsilon_0}k_0$.

Next, we note that, according to Eq. 5.13(a), $\nabla_t \times \mathbf{e}_t(x, y) = 0$. Therefore, $\mathbf{e}_t(x, y)$ can be written as a gradient of a scalar function as follows:

$$\mathbf{e}_t(x, y) = -\nabla_t \Phi_t(x, y), \tag{5.14}$$

where $\Phi_t(x, y)$ is generally called the two-dimensional scalar electrical potential.

It is apparent from Eq. 5.13(c) that this function also satisfies $\nabla_t^2 \Phi_t(x, y) = 0$. The electric field can then be obtained from Φ_t as follows:

$$\mathbf{E}_t(x, y, z) = -e^{i\beta z} \nabla_t \Phi_t(x, y). \tag{5.15}$$

As a result of the assumption that the metals and the filling dielectric extend to infinity in the x direction, we obtain $\Phi_t(x, y) = \Phi_t(y)$ and the electrical potential inside the waveguide can be calculated by solving the following simple differential equation:

$$\nabla_t^2 \Phi_t(y) = \frac{d^2}{dy^2} \Phi_t(y) = 0, \tag{5.16}$$

where the solution is in the form of $\Phi_t(y) = c_1 y + c_2$. Assuming a potential difference of V_0 between the two plates, we obtain $\Phi_t(y) = yV_0/b$. Using Eqs. 5.13(e) and 5.15, $\mathbf{E}_t$ and $\mathbf{H}_t$ are obtained as

$$\mathbf{E}_t = -\hat{\mathbf{y}} \frac{V_0}{b} e^{-i\beta z} \tag{5.17a}$$

$$\mathbf{H}_t = \hat{\mathbf{x}} \frac{V_0}{Z_{\text{TEM}} b} e^{-i\beta z} \tag{5.17b}$$

Eq. 5.17 shows that the TEM mode inside a parallel-plate metallic waveguide is equivalent to plane-wave propagation in a dielectric medium. It is also important to notice that the cut-off frequency, which satisfies $\beta = 0$, is given as $f_c = 0$ and therefore, any non-zero frequency can be guided in the TEM mode. This conclusion is quite significant and $f_c = 0$ property is special to only TEM modes.

5.2.3 TE Modes

For TE waves, the electric field is entirely transverse to the propagation direction, whereas the magnetic field is not. Accordingly, we have $\mathbf{e}_z = 0$ and $\mathbf{h}_z \neq 0$ and the rectilinear Maxwell equations assume the following form:

$$\nabla_t \times \mathbf{e}_t = -iw\mu_0 \mathbf{h}_z \tag{5.18a}$$

$$\nabla_t \times \mathbf{h}_t = 0 \tag{5.18b}$$

$$\nabla_t \cdot \mathbf{e}_t = 0 \tag{5.18c}$$

$$\nabla_t \cdot \mathbf{h}_t = i\beta h_z \tag{5.18d}$$

$$\hat{\mathbf{z}} \times i\beta \mathbf{e}_t = iw\mu_0 \mathbf{h}_t \tag{5.18e}$$

$$\hat{\mathbf{z}} \times (\nabla_t h_z + i\beta \mathbf{h}_t) = -iw\epsilon \mathbf{e}_t \tag{5.18f}$$

Modifying the Helmholtz equation ($[\nabla^2 + k^2]\mathbf{H} = 0$) by replacing $\mathbf{H}$ with $(\mathbf{h}_t + \mathbf{h}_z)$ yields the following wave equation:

$$(\nabla_t^2 + k^2 - \beta^2)[\mathbf{h}_t + \mathbf{h}_z] = 0. \tag{5.19}$$

By simply neglecting the transverse component of $\mathbf{H}$ in Eq. 5.19, we obtain

$$(\nabla_t^2 + k^2 - \beta^2)\mathbf{h}_z = 0. \tag{5.20}$$

In addition, we know from Eq. 5.18(b) that $\nabla_t \times \mathbf{h}_t = 0$. We use the vector identity $\nabla_t \times \nabla_t \times \mathbf{A} = \nabla_t(\nabla_t \cdot \mathbf{A}) - \nabla_t^2 \mathbf{A}$ on this equation and obtain

$$\nabla_t \times \nabla_t \times \mathbf{h}_t = \nabla_t(\nabla_t \cdot \mathbf{h}_t) - \nabla_t^2 \mathbf{h}_t. \tag{5.21}$$

Further, by using Eqs. 5.18(d) and the transverse component of Eq. 5.19, Eq. 5.21 can be rewritten as

$$\nabla_t(i\beta h_z) + (k^2 - \beta^2)\mathbf{h}_t = 0. \tag{5.22}$$

Using the vector identity $\mathbf{A} \times (\mathbf{B} \times \mathbf{C}) = (\mathbf{A} \cdot \mathbf{C})\mathbf{B} - (\mathbf{A} \cdot \mathbf{B})\mathbf{C}$ on Eq. 5.18(e) as $\hat{\mathbf{z}} \times (\hat{\mathbf{z}} \times i\beta \mathbf{e}_t) = iw\mu_0(\hat{\mathbf{z}} \times \mathbf{h}_t)$, one can write

$$\mathbf{e}_t = -Z_{\mathrm{TE}} \hat{\mathbf{z}} \times \mathbf{h}_t, \tag{5.23}$$

where $Z_{\mathrm{TE}} = w\mu_0/\beta$ is the characteristic impedance for TE waves. The validation of Z_{TE} is not restricted to TE waves only in parallel-plate metallic waveguides.

In summary, once β is known, one can calculate $\mathbf{h}_z$ from Eq. 5.20 using the appropriate boundary conditions and with this knowledge, $\mathbf{h}_t$ can be calculated from Eq. 5.22. Finally, $\mathbf{e}_t$ can be determined by using Eq. 5.23.

Next, let us assume that $\partial/\partial x = 0$, since the parallel-plate metallic waveguide extends to infinity in the x direction. Under this assumption, Eq. 5.20 simplifies to the following:

$$\frac{\partial^2}{\partial y^2} h_z = -k_c^2 h_z, \tag{5.24}$$

where $k_c^2 = k^2 - \beta^2$ is the lateral wavevector of the corresponding mode. It should be noted that $k_c = 0$ for TEM modes. Eq. 5.24 is a second-order ordinary differential equation and the general form of the solution is

$$h_z = A\sin(k_c y) + B\cos(k_c y). \tag{5.25}$$

Since $e_x(0) = e_x(b) = 0$ due to $\sigma \to \infty$ and $e_x(y)$ is proportional to dh_z/dy, $dh_z(0)/dy = dh_z(b)/dy = 0$ must be satisfied and therefore, we obtain $h_z(y) = B\cos(k_c y)$. Further, the boundary conditions for dh_z/dy are satisfied when

$$k_c b = n\pi \qquad n = 1, 2, 3, ... \tag{5.26}$$

and as a result

$$h_z(y) = B\cos\left(\frac{n\pi}{b} y\right). \tag{5.27}$$

Using Eq. 5.22, one can simply write

$$\mathbf{h}_t(y) = \hat{\mathbf{y}} \frac{i\beta b}{n\pi} B\sin\left(\frac{n\pi}{b} y\right). \tag{5.28}$$

Finally, using Eq. 5.23, we calculate $\mathbf{e}_t$ as

$$\mathbf{e}_t(y) = \hat{\mathbf{x}} \frac{i\beta b}{n\pi} Z_{\mathrm{TE}} B\sin\left(\frac{n\pi}{b} y\right). \tag{5.29}$$

It is noteworthy that Eq. 5.26 allows an infinite number of modes with different field distributions and propagation constants. For this reason, the corresponding field distributions ($\mathbf{h}_z$, $\mathbf{h}_t$, and $\mathbf{e}_t$) are said to describe the TE_n mode for the parallel-plate metallic waveguide. The propagation constant, $\beta = \sqrt{k^2 - k_c^2}$,

of the TE_n mode is given by

$$\beta_n = \sqrt{k^2 - \left(\frac{n\pi}{b}\right)^2}, \tag{5.30}$$

where $k = \sqrt{\epsilon/\epsilon_0}w/c_0$. Below a certain wavelength, β is purely imaginary and the corresponding mode decays exponentially with z without phase progression. The wavelength of transition from a propagating mode to an evanescent mode is called the cut-off wavelength and is written as

$$\lambda_{c,n} = \frac{2b}{n}. \tag{5.31}$$

Above the cut-off wavelength, the corresponding TE_n mode propagates inside the waveguide without attenuation. Finally, it should be noted that the characteristic impedance of TE modes is dependent on both frequency and n.

5.2.4 TM Modes

For TM waves, the magnetic field is entirely transverse to the propagation direction, whereas the electric field is not. Accordingly, we have $\mathbf{h}_z = 0$ and $\mathbf{e}_z \neq 0$ and the rectilinear Maxwell equations assume the following form:

$$\nabla_t \times \mathbf{e}_t = 0 \tag{5.32a}$$

$$\nabla_t \times \mathbf{h}_t = iw\epsilon\mathbf{e}_z \tag{5.32b}$$

$$\nabla_t \cdot \mathbf{e}_t = i\beta\mathbf{e}_z \tag{5.32c}$$

$$\nabla_t \cdot \mathbf{h}_t = 0 \tag{5.32d}$$

$$\hat{\mathbf{z}} \times (\nabla_t e_z + i\beta\mathbf{e}_t) = iw\mu_0\mathbf{h}_t \tag{5.32e}$$

$$\hat{\mathbf{z}} \times i\beta\mathbf{h}_t = -iw\epsilon\mathbf{e}_t \tag{5.32f}$$

It is notable that the rectilinear Maxwell equations for TE and TM waves are in the same mathematical form, see Eqs. 5.18 and 5.32. The variables that occupy identical positions in these equations are called *dual* quantities and if the solution to one equation system is known, the solutions of the *dual* equation system can

TE	$\Longrightarrow$	TM
$\mathbf{e}_t$	$\Longrightarrow$	$\mathbf{h}_t$
$\mathbf{h}_t$	$\Longrightarrow$	$\mathbf{e}_t$
$\mathbf{h}_z$	$\Longrightarrow$	$\mathbf{e}_z$
ϵ	$\Longrightarrow$	$-\mu_0$
μ_0	$\Longrightarrow$	$-\epsilon$

Table 5.1: Dual variables between the TE and TM equations. The equations obtained for TE waves can be directly used for TM waves provided that the changes indicated by the arrows are performed.

be determined by a simple interchange of variables. Therefore, we will not go into the details of the derivation of TM equations. The required variable changes are shown in Table 5.1.

By using the duality principle, Eqs. 5.20, 5.22, 5.23, and 5.24 can be modified to satisfy Eq. 5.32 and the resultant equations are written as follows:

$$(\nabla_t^2 + k^2 - \beta^2)\mathbf{e}_z = 0 \tag{5.33a}$$

$$\nabla_t(i\beta e_z) + (k^2 - \beta^2)\mathbf{e}_t = 0 \tag{5.33b}$$

$$\mathbf{h}_t = \frac{1}{Z_{\mathrm{TM}}}\hat{\mathbf{z}} \times \mathbf{e}_t \tag{5.33c}$$

$$\frac{\partial^2}{\partial y^2}e_z = -k_c^2 e_z \tag{5.33d}$$

In Eq. 5.33, Z_{TM} is the TM field characteristic impedance and using duality, its value is obtained as $Z_{\mathrm{TM}} = \beta/(w\epsilon)$. Similar to Z_{TE}, Z_{TM} is not only valid for the parallel-plate metallic waveguide, but for all waveguides supporting TM modes.

The general solution of Eq. 5.33(d) is

$$e_z(y) = A\sin(k_c y) + B\cos(k_c y). \tag{5.34}$$

The perfect conductivity assumption for metals dictates that $\hat{\mathbf{y}} \times \mathbf{E} = 0$ at $y = 0$ and $y = b$. This condition translates to $e_z(0) = e_z(b) = 0$ and the solution that satisfies the boundary condition requires $B = 0$ and

$$k_c = \frac{\pi}{b}n \qquad n = 1, 2, 3, ... \tag{5.35}$$

Thus, e_z is given by

$$e_z(y) = A \sin\left(\frac{\pi n}{b} y\right). \tag{5.36}$$

Finally, using Eqs. 5.33(b) and (c), we calculate $\mathbf{e}_t$ and $\mathbf{h}_t$ as

$$\mathbf{e}_t(y) = -\hat{\mathbf{y}} \frac{i\beta b}{n\pi} A \cos\left(\frac{n\pi}{b} y\right) \tag{5.37a}$$

$$\mathbf{h}_t(y) = \hat{\mathbf{x}} \frac{i\beta b}{n\pi} \frac{1}{Z_{\mathrm{TM}}} A \cos\left(\frac{n\pi}{b} y\right) \tag{5.37b}$$

We have calculated the field distributions ($\mathbf{e}_z$, $\mathbf{e}_t$, and $\mathbf{h}_t$) for a TM_n mode inside the waveguide. For a complete knowledge of the fields, one needs to evaluate the propagation constant of the TM_n modes, which is

$$\beta_n = \sqrt{k^2 - k_c^2} = \sqrt{k^2 - \left(\frac{n\pi}{b}\right)^2}. \tag{5.38}$$

The propagation constants for the TE_n and TM_n modes are equal and therefore, the cut-off condition given in Eq. 5.31 is also valid for the TM case.

5.3 Dielectric Slab Waveguide

The dielectric slab waveguide geometry that will be investigated theoretically in this section is depicted in Fig. 5.2. In determining the dispersion relations for the dielectric slab waveguide, we will abandon the separation of $\mathbf{E}$ and $\mathbf{H}$ into transverse and longitudinal components and make use of the vector potentials $\mathbf{A}$ and $\mathbf{F}$ since they allow the determination of the full wave components in the space with a relatively simple analysis.

5.3.1 Vector Potential A

In particular, in this context, vector potential $\mathbf{A}$ will be very useful for characterizing the TM modes inside a dielectric slab waveguide.

Since $\nabla \cdot \mathbf{B} = 0$, which states that the $\mathbf{B}$ field is always solenoidal, $\mathbf{B}$ can be

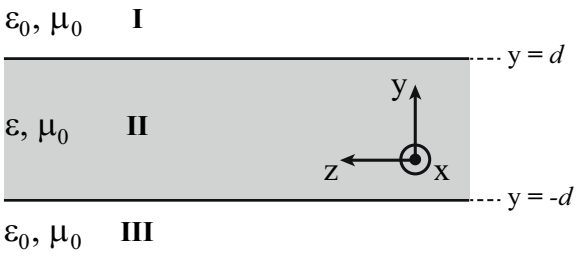

Figure 5.2: Dielectric slab waveguide geometry. The outer dielectrics are assumed to be free-space for simplicity. The inner dielectric is characterized by an absolute permittivity of ϵ and an absolute permeability of μ_0. The structure is assumed to be extending to infinity in the x and z directions. The waveguide modes propagate in the $+z$ direction.

defined as a curl of another vector such that

$$\mathbf{H} = \frac{1}{\mu}\nabla \times \mathbf{A}. \tag{5.39}$$

Using the equation $\nabla \times \mathbf{E} = -iw\mu\mathbf{H}$, we obtain

$$\nabla \times (\mathbf{E} + iw\mathbf{A}) = 0. \tag{5.40}$$

From the vector identity $\nabla \times (-\nabla\Phi) = 0$, it follows that

$$\mathbf{E} = -\nabla\Phi - iw\mathbf{A}, \tag{5.41}$$

where Φ is a function of x, y, and z and generally called the three dimensional scalar electrical potential function. In Eq. 5.39, we have defined the curl of $\mathbf{A}$. However, for a unique description of the vector, $\mathbf{A}$, we have to also define $\nabla \cdot \mathbf{A}$. In the following steps, we will intend to specify the divergence of $\mathbf{A}$. We first start with the vector identity $\nabla \times \nabla \times \mathbf{A} = \nabla(\nabla \cdot \mathbf{A}) - \nabla^2\mathbf{A}$ and using Eq. 5.39, we obtain

$$\mu\nabla \times \mathbf{H} = \nabla(\nabla \cdot \mathbf{A}) - \nabla^2\mathbf{A}. \tag{5.42}$$

Please note that Eq. 5.42 is derived under the assumption that the corresponding medium is homogeneous, i.e., its electromagnetic properties do not depend on

space coordinates. Combining this result with $\nabla \times \mathbf{H} = \mathbf{J} + iw\epsilon\mathbf{E}$ leads to

$$\mu_0\mathbf{J} + iw\mu_0\epsilon\mathbf{E} = \nabla(\nabla \cdot \mathbf{A}) - \nabla^2\mathbf{A}. \tag{5.43}$$

Substituting $\mathbf{E}$ from Eq. 5.41 into Eq. 5.43 yields

$$\nabla^2\mathbf{A} + w^2\mu_0\epsilon\mathbf{A} = -\mu\mathbf{J} + \nabla(\nabla \cdot \mathbf{A} + iw\mu_0\epsilon\Phi). \tag{5.44}$$

We are now able to define the divergence of $\mathbf{A}$ arbitrarily for ensuring a unique description. We use the Lorentz gauge for the purpose of simplifying the subsequent tedious calculations, which assumes that

$$\nabla \cdot \mathbf{A} = -iw\mu_0\epsilon\Phi. \tag{5.45}$$

Therefore, Eq. 5.44 assumes a wave equation form as follows:

$$\nabla^2\mathbf{A} + k^2\mathbf{A} = -\mu\mathbf{J}, \tag{5.46}$$

where $k^2 = w^2\mu_0\epsilon$ is the wavenumber inside the corresponding medium. Finally, by combining Eqs. 5.41 and 5.45, we obtain

$$\mathbf{E} = -iw\mathbf{A} - \frac{i}{w\mu_0\epsilon}\nabla(\nabla \cdot \mathbf{A}), \tag{5.47}$$

which is an important conclusion of this subsection.

Subsequently, we will investigate the relation between $\mathbf{E}$ and $\mathbf{H}$, and $\mathbf{A}$ further for TM waves propagating in the z direction. We will omit the discussion related to TEM waves in this thesis since the dielectric slab waveguide, in contrast to the parallel-plate metallic waveguide, does not support TEM modes.

By expanding Eq. 5.47 in rectangular coordinates, we obtain the following equations that relate $\mathbf{E}$ and $\mathbf{A}$:

$$E_x = -iwA_x - \frac{i}{w\mu_0\epsilon}\left(\frac{\partial^2}{\partial x^2}A_x + \frac{\partial^2}{\partial x\partial y}A_y + \frac{\partial^2}{\partial x\partial z}A_z\right). \tag{5.48a}$$

$$E_y = -iwA_y - \frac{i}{w\mu_0\epsilon}\left(\frac{\partial^2}{\partial x \partial y}A_x + \frac{\partial^2}{\partial y^2}A_y + \frac{\partial^2}{\partial y \partial z}A_z\right). \tag{5.48b}$$

$$E_z = -iwA_z - \frac{i}{w\mu_0\epsilon}\left(\frac{\partial^2}{\partial x \partial z}A_x + \frac{\partial^2}{\partial y \partial z}A_y + \frac{\partial^2}{\partial z^2}A_z\right). \tag{5.48c}$$

By letting $A_x = A_y = 0$ and $\partial/\partial x = 0$, we obtain

$$E_x = 0. \tag{5.49a}$$

$$E_y = -\frac{i}{w\mu_0\epsilon}\frac{\partial^2}{\partial y \partial z}A_z. \tag{5.49b}$$

$$E_z = -\frac{i}{w\mu_0\epsilon}\left(k^2 + \frac{\partial^2}{\partial z^2}\right)A_z. \tag{5.49c}$$

If we perform the same expansion for $\mathbf{H}$ while noting that $H_z = 0$ for a TM wave, we obtain:

$$H_x = \frac{1}{\mu_0}\frac{\partial}{\partial y}A_z \tag{5.50a}$$

$$H_y = 0 \tag{5.50b}$$

$$H_z = 0 \tag{5.50c}$$

5.3.2 Vector Potential F

In order to simplify the analysis of $\mathbf{E}$ and $\mathbf{H}$ fields, we need to define another vector potential, $\mathbf{F}$, by noting that $\nabla \cdot \mathbf{D} = 0$ in a source-free region. Actually, $\mathbf{F}$ is the dual of $\mathbf{A}$ and therefore, we will provide the fundamental properties of $\mathbf{F}$ without performing the steps that are very similar to the ones in the previous subsection. $\mathbf{F}$ will be used for characterizing the TE modes inside a dielectric slab waveguide as opposed to $\mathbf{A}$.

The curl of $\mathbf{F}$ can be defined as

$$\nabla \times \mathbf{F} = -\epsilon\mathbf{E}. \tag{5.51}$$

By using a gauge that suggests $\nabla \cdot \mathbf{F} = -iw\mu_0\epsilon\Phi_m$, where Φ_m is the three dimensional magnetic scalar potential, we can easily prove that $\mathbf{F}$ satisfies the

$\mathbf{A}$	$\Longrightarrow$	$\mathbf{F}$
$\mathbf{E}$	$\Longrightarrow$	$\mathbf{H}$
$\mathbf{H}$	$\Longrightarrow$	$\mathbf{E}$
ϵ	$\Longrightarrow$	$-\mu_0$
μ_0	$\Longrightarrow$	$-\epsilon$
$\mathbf{J}$	$\Longrightarrow$	$-\mathbf{M}$

Table 5.2: Dual variables between $\mathbf{A}$ and $\mathbf{F}$. The equations obtained for $\mathbf{A}$ can be directly used for $\mathbf{F}$ provided that the changes indicated by the arrows are performed.

following wave equation:

$$\nabla^2\mathbf{F} + k^2\mathbf{F} = -\epsilon\mathbf{M}, \tag{5.52}$$

where $\mathbf{M}$ is the hypothetical magnetic current density. Finally, $\mathbf{H}$ can be calculated with the knowledge of $\mathbf{F}$ as follows:

$$\mathbf{H} = -iw\mathbf{F} - \frac{i}{w\mu_0\epsilon}\nabla(\nabla\cdot\mathbf{F}). \tag{5.53}$$

It is readily seen that $\mathbf{A}$ and $\mathbf{F}$ are dual variables and the equations for $\mathbf{F}$ can be obtained by making the specified interchanging operations shown in Table 5.2.

We use the above mentioned duality principle for the obtaining of the relation between $\mathbf{E}$ and $\mathbf{H}$, and $\mathbf{F}$ for TE waves under the assumptions that $F_x = F_y = 0$, i.e., the TE wave is propagating in the z direction and $\partial/\partial x = 0$ due to the lack of any selectivity with respect to the x direction. Accordingly, $\mathbf{E}$ can be determined with the knowledge of $\mathbf{F}$ as follows:

$$E_x = -\frac{1}{\epsilon}\frac{\partial}{\partial y}F_z \tag{5.54a}$$

$$E_y = 0 \tag{5.54b}$$

$$E_z = 0 \tag{5.54c}$$

Finally, $\mathbf{H}$ can be calculated by using $\mathbf{F}$ as

$$H_x = 0 \tag{5.55a}$$

$$H_y = -\frac{i}{w\mu_0\epsilon}\frac{\partial^2}{\partial y\partial z}F_z \tag{5.55b}$$

$$H_z = -\frac{i}{w\mu_0\epsilon}\left(k^2 + \frac{\partial^2}{\partial z^2}\right) F_z \tag{5.55c}$$

5.3.3 TM Modes

Due to the lack of a (perfectly) conducting medium, which ensures $\hat{\mathbf{y}} \times \mathbf{E} = 0$ at the boundaries, $y = -d$ and $y = d$, the mode is expected to leak to the outside of the guiding (central) dielectric. However, the fields are expected to decay exponentially outside the guiding dielectric region due to the fact that their transverse wavenumbers are imaginary in these regions.

Correspondingly, inside the guiding dielectric and for $+z$ propagation, we have

$$A_z^{\mathrm{II}} = [B_2 \cos(k_c y) + C_2 \sin(k_c y)]e^{-i\beta z}, \tag{5.56}$$

where k_c and β denote the transverse wavenumber and the propagation constant, respectively. In Eq. 5.56, the cosine and sine functions denote the even and odd modes, respectively. Further, expectedly, the relation $k_{\mathrm{II}}^2 = k_c^2 + \beta^2$ holds in this region. For $y \geq d$, we have

$$A_z^{\mathrm{I}} = B_1 e^{-\alpha y} e^{-i\beta z} \tag{5.57}$$

and $k_{\mathrm{I}}^2 = \beta^2 - \alpha^2$. Similarly, for $y \leq -d$,

$$A_z^{\mathrm{III}} = B_1 e^{\alpha y} e^{-i\beta z} \tag{5.58}$$

and $k_{\mathrm{III}}^2 = k_{\mathrm{I}}^2$ hold under the assumption that the same dielectric is used in regions I and III.

Next, by using the electromagnetic boundary conditions $\hat{\mathbf{n}} \times (\mathbf{E}_2 - \mathbf{E}_1) = 0$ and $\hat{\mathbf{n}} \times (\mathbf{H}_2 - \mathbf{H}_1) = \mathbf{J}_s$, where $\hat{\mathbf{n}}$ is the surface normal and $\mathbf{J}_s = 0$ is the surface current density, we arrive at the following independent conditions:

$$E_z^{\mathrm{I}}(y = d) = E_z^{\mathrm{II}}(y = d) \tag{5.59a}$$

$$H_x^{\mathrm{I}}(y = d) = H_x^{\mathrm{II}}(y = d) \tag{5.59b}$$

The boundary conditions at $y = -d$ are omitted due to the mirror symmetry of the geometry with respect to $y = 0$. In other words, satisfaction of Eq. 5.59 ensures the satisfaction of the boundary conditions at $y = -d$.

Now, we will investigate the even and odd components of Eq. 5.56 separately for the purpose of determining the dispersion relations for even and odd TM modes. For the sake of simplicity, we assume that regions I and III consist of free-space, i.e., the dielectric permittivity and the wavenumber is equal to ϵ_0 and k_0 in these regions, respectively. For definiteness, it is stated that the dielectric permittivity of the guiding dielectric is assumed to be ϵ and the resultant wavenumber is given by $k_{\mathrm{II}} = k = w\sqrt{\mu_0\epsilon}$.

A. EVEN MODES

For even modes, A_z^{II} is written using Eq. 5.56 as

$$A_z^{\mathrm{II}} = B_2 \cos(k_c y) e^{-i\beta z}. \tag{5.60}$$

The usage of Eqs. 5.49(c) and 5.50(a) yields

$$E_z^{\mathrm{II}} = -i\frac{k^2 - \beta^2}{w\mu_0\epsilon} B_2 \cos(k_c y) e^{-i\beta z}. \tag{5.61a}$$

$$H_x^{\mathrm{II}} = -\frac{k_c}{\mu_0} B_2 \sin(k_c y) e^{-i\beta z}. \tag{5.61b}$$

Afterwards, by using the same equations, but this time for A_z^{I}, we can write

$$E_z^{\mathrm{I}} = -i\frac{k_0^2 - \beta^2}{w\mu_0\epsilon_0} B_1 e^{-\alpha y} e^{-i\beta z}. \tag{5.62a}$$

$$H_x^{\mathrm{I}} = -\frac{\alpha}{\mu_0} B_1 e^{-\alpha y} e^{-i\beta z}. \tag{5.62b}$$

By equating Eqs. 5.61 and 5.62 as suggested by Eq. 5.59, it follows that

$$\frac{k_c^2}{\epsilon} B_2 \cos(k_c d) = -\frac{\alpha^2}{\epsilon_0} B_1 e^{-\alpha d}. \tag{5.63a}$$

$$k_c B_2 \sin(k_c d) = \alpha B_1 e^{-\alpha d}. \tag{5.63b}$$

Division of Eq. 5.63(a) by Eq. 5.63(b) results in the dispersion relation, which relates k_c and α, for even TM modes. Accordingly, we write

$$-\frac{\epsilon_0}{\epsilon}k_c\cot(k_c d)=\alpha. \tag{5.64}$$

B. ODD MODES

For odd modes, A_z^{II} is written using Eq. 5.56 as

$$A_z^{\mathrm{II}}=C_2\sin(k_c y)e^{-i\beta z}. \tag{5.65}$$

The usage of Eqs. 5.49(c) and 5.50(a) yields

$$E_z^{\mathrm{II}}=-i\frac{k^2-\beta^2}{w\mu_0\epsilon}C_2\sin(k_c y)e^{-i\beta z}. \tag{5.66a}$$

$$H_x^{\mathrm{II}}=\frac{k_c}{\mu_0}C_2\cos(k_c y)e^{-i\beta z}. \tag{5.66b}$$

By borrowing the expressions for E_z^{I} and H_x^{I} from Eq. 5.62, and using the corresponding boundary conditions given in Eq. 5.59, we write

$$\frac{k_c^2}{\epsilon}C_2\sin(k_c d)=-\frac{\alpha^2}{\epsilon_0}B_1e^{-\alpha d}. \tag{5.67a}$$

$$k_c C_2\cos(k_c d)=-\alpha B_1 e^{-\alpha d}. \tag{5.67b}$$

Division of Eq. 5.67(a) by Eq. 5.67(b) results in the dispersion relation, which relates k_c and α, for odd TM modes. Accordingly, we write

$$\frac{\epsilon_0}{\epsilon}k_c\tan(k_c d)=\alpha. \tag{5.68}$$

5.3.4 TE Modes

The derivation of the dispersion relations for even and odd TE modes is very similar to the one shown for TM modes. The main difference is that **F** should be utilized instead of **A**. In fact, utilizing duality, one can automatically obtain the

TE dispersion relations using Table 5.2 without going into further derivations. However, for the sake of completeness, we will show the corresponding derivations briefly in this subsection.

First of all, we define $\mathbf{F}$ such that $F_x = F_y = 0$ and

$$F_z^{\mathrm{I}} = B_1 e^{-\alpha y} e^{-i\beta z} \tag{5.69a}$$

$$F_z^{\mathrm{II}} = [B_2 \cos(k_c y) + C_2 \sin(k_c y)] e^{-i\beta z} \tag{5.69b}$$

$$F_z^{\mathrm{III}} = B_1 e^{\alpha y} e^{-i\beta z} \tag{5.69c}$$

Next, we will investigate the characteristics of the even and odd TE modes inside the dielectric slab waveguide.

A. EVEN MODES

For even TE modes, using Eq. 5.69, we write

$$F_z^{\mathrm{II}} = B_2 \cos(k_c y) e^{-i\beta z} \tag{5.70}$$

and, by using Eqs. 5.54(a) and 5.55(c),

$$E_x^{\mathrm{II}} = \frac{k_c}{\epsilon} B_2 \sin(k_c y) e^{-i\beta z}. \tag{5.71a}$$

$$H_z^{\mathrm{II}} = -i \frac{k_c^2}{w\mu_0 \epsilon} B_2 \cos(k_c y) e^{-i\beta z}. \tag{5.71b}$$

A similar analysis for F_z^{I} suggests

$$E_x^{\mathrm{I}} = \frac{\alpha}{\epsilon_0} B_1 e^{-\alpha y} e^{-i\beta z} \tag{5.72a}$$

$$H_z^{\mathrm{I}} = i \frac{\alpha^2}{w\mu_0 \epsilon_0} B_1 e^{-\alpha y} e^{-i\beta z}. \tag{5.72b}$$

Next, by using the electromagnetic boundary conditions $\hat{\mathbf{n}} \times (\mathbf{E}_2 - \mathbf{E}_1) = 0$ and $\hat{\mathbf{n}} \times (\mathbf{H}_2 - \mathbf{H}_1) = 0$, the following equations are obtained:

$$E_x^{\mathrm{I}}(y = d) = E_x^{\mathrm{II}}(y = d) \tag{5.73a}$$

$$H_z^{\mathrm{I}}(y=d) = H_z^{\mathrm{II}}(y=d) \tag{5.73b}$$

Using the boundary conditions given in Eq. 5.73 and E_x^{I}, E_x^{II}, H_z^{I}, and H_z^{II} expressions from Eqs. 5.71 and 5.72 result in

$$k_c^2 B_2 \cos(k_c d) = -\alpha^2 B_1 e^{-\alpha d}. \tag{5.74a}$$

$$k_c B_2 \sin(k_c d) = \alpha B_1 e^{-\alpha d}. \tag{5.74b}$$

By dividing Eq. 5.74(a) by Eq. 5.74(b), we arrive at the dispersion relation for even TE modes:

$$-k_c \cot(k_c d) = \alpha. \tag{5.75}$$

B. ODD MODES

For odd TE modes, using Eq. 5.69, we write

$$F_z^{\mathrm{II}} = C_2 \sin(k_c y) e^{-i\beta z} \tag{5.76}$$

and, by using Eqs. 5.54 and 5.55, we obtain

$$E_x^{\mathrm{II}} = -\frac{k_c}{\epsilon} C_2 \cos(k_c y) e^{-i\beta z}. \tag{5.77a}$$

$$H_z^{\mathrm{II}} = -i\frac{k_c^2}{w\mu_0\epsilon} C_2 \sin(k_c y) e^{-i\beta z}. \tag{5.77b}$$

Applying the boundary conditions given in Eq. 5.73 yields the following set of equations:

$$-\frac{k_c^2}{\epsilon} C_2 \sin(k_c d) = \frac{\alpha^2}{\epsilon_0} B_1 e^{-\alpha d}. \tag{5.78a}$$

$$-\frac{k_c}{\epsilon} C_2 \cos(k_c d) = \frac{\alpha}{\epsilon_0} B_1 e^{-\alpha d}. \tag{5.78b}$$

By dividing Eq. 5.78(a) by Eq. 5.78(b), we arrive at the following dispersion relation for odd TE modes:

$$k_c \tan(k_c d) = \alpha. \tag{5.79}$$

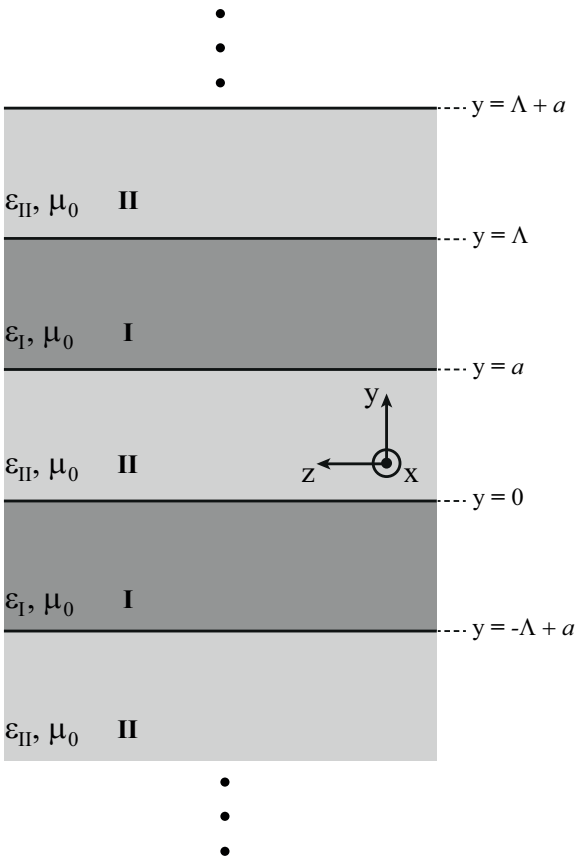

Figure 5.3: Periodic dielectric slab waveguide geometry. The structure is assumed to be extending to infinity in the x and z directions. The waveguide modes propagate in the $+z$ direction.

5.4 Periodic Dielectric Slab Waveguide

In this section, we investigate the electric and magnetic field equations inside and the dispersion relations of a periodic dielectric slab waveguide, which is composed of infinitely many alternating dielectric layers and depicted in Fig. 5.3. In this consideration, the propagation and periodicity directions are given as z and y, respectively. The structure is assumed to be infinitely long in the x direction, resulting in $\partial/\partial x = 0$.

5.4.1 TM Modes

In this theoretical analysis, we will limit our discussion to plane wave excitation and propagation only in the $+z$ direction. We also assume that $E_{x,i} = 0$, $H_{y,i} = 0$, $E_{y,i} \neq 0$, and $H_{x,i} \neq 0$, where i in the subscript is used for referring the incident wave. This assumption is equivalent to stating that the incident wave is a TEM wave and can excite a TM waveguide mode, see Eqs. 5.49 and 5.50. Further, $E_{y,i}$ and $H_{x,i}$ are even functions of the lateral coordinate, y, meaning that only the mode with even transverse field components can be excited by this wave. In other words, (longitudinally) even modes cannot be excited by such a wave since the spatial overlap integral between the incident plane wave and the even mode is proportional to what is given as follows:

$$\int_{-y_i/2}^{y_i/2} \sin(k_c y) dy = 0, \tag{5.80}$$

where y_i denotes the thickness of a particular dielectric slab. The integral limits can be taken as $-y_i/2$ and $y_i/2$, since one can always modify the origin of the coordinate system to yield these limits. Simply, Eq. 5.80 shows that an incident plane wave cannot excite a (longitudinally) even mode due to the lack of spatial matching between the incident wave and the corresponding waveguide mode. By using the results given in Sec. 5.3.3, we can state that only (longitudinally) odd TM modes can be excited in such a structure.

In this analysis, irrespective of whether it is true or not, we will assume that lateral wavenumbers of the waveguide modes are always purely real. This assumption is reasonable, since, under this assumption, the obtaining of a purely imaginary lateral wavenumber corresponds to the hyperbolic cosine function, which exhibits even symmetry with respect to the center of the dielectric and decreases exponentially towards the center. Therefore, the hyperbolic cosine function denotes the evanescently decaying modes in the periodic dielectric slab case.

Accordingly, considering the even symmetry of E_y^{II} and H_x^{II} with respect to $y = a/2$, and E_y^{I} and H_x^{I} with respect to $y = (\Lambda + a)/2$, we write the vector

potentials, A_z^{I} and A_z^{II} as follows:

$$A_z^{\mathrm{I}} = B_1 \sin\left\{k_{c,\mathrm{I}}\left[y - (\Lambda + a)/2\right]\right\} e^{-i\beta z}, \tag{5.81a}$$

$$A_z^{\mathrm{II}} = B_2 \sin\left[k_{c,\mathrm{II}}(y - a/2)\right] e^{-i\beta z}, \tag{5.81b}$$

where $k_{c,\mathrm{I}}$ and $k_{c,\mathrm{II}}$ are the lateral wavenumbers inside regions I and II, respectively. Next, using Eqs. 5.49 and 5.50, we write the longitudinal electric fields as

$$E_z^{\mathrm{I}} = -i\frac{k_{\mathrm{I}}^2 - \beta^2}{w\mu_0\epsilon_{\mathrm{I}}} B_1 \sin\left\{k_{c,\mathrm{I}}\left[y - (\Lambda + a)/2\right]\right\} e^{-i\beta z} \tag{5.82a}$$

$$E_z^{\mathrm{II}} = -i\frac{k_{\mathrm{II}}^2 - \beta^2}{w\mu_0\epsilon_{\mathrm{II}}} B_2 \sin\left[k_{c,\mathrm{II}}(y - a/2)\right] e^{-i\beta z} \tag{5.82b}$$

and the magnetic fields as

$$H_x^{\mathrm{I}} = \frac{k_{c,\mathrm{I}}}{\mu_0} B_1 \cos\left\{k_{c,\mathrm{I}}\left[y - (\Lambda + a)/2\right]\right\} e^{-i\beta z}. \tag{5.83a}$$

$$H_x^{\mathrm{II}} = \frac{k_{c,\mathrm{II}}}{\mu_0} B_2 \cos\left[k_{c,\mathrm{II}}(y - a/2)\right] e^{-i\beta z}. \tag{5.83b}$$

Please note that, in this case, $k_{\mathrm{I}}^2 = w^2\mu_0\epsilon_{\mathrm{I}} = k_{c,\mathrm{I}}^2 + \beta^2$ and $k_{\mathrm{II}}^2 = w^2\mu_0\epsilon_{\mathrm{II}} = k_{c,\mathrm{II}}^2 + \beta^2$.

In contrast to the previously analyzed parallel-plate and dielectric slab waveguides, the periodic boundary conditions are applicable in addition to the electromagnetic boundary conditions given in Eq. 5.59. These periodic boundary conditions are written as follows:

$$E_z^{\mathrm{I}}(y = \Lambda) = E_z^{\mathrm{II}}(y = 0). \tag{5.84a}$$

$$H_x^{\mathrm{I}}(y = \Lambda) = H_x^{\mathrm{II}}(y = 0). \tag{5.84b}$$

Application of Eq. 5.84(a) on Eq. 5.82 yields the following:

$$-\frac{k_{c,\mathrm{I}}^2}{\epsilon_{\mathrm{I}}} B_1 \sin\left(k_{c,\mathrm{I}}\frac{s}{2}\right) = \frac{k_{c,\mathrm{II}}^2}{\epsilon_{\mathrm{II}}} B_2 \sin\left(k_{c,\mathrm{II}}\frac{a}{2}\right), \tag{5.85}$$

where $s = \Lambda - a$. Similarly, by applying Eq. 5.84(b) on Eq. 5.83, we obtain

$$k_{c,\mathrm{I}} B_1 \cos\left(k_{c,\mathrm{I}} \frac{s}{2}\right) = k_{c,\mathrm{II}} B_2 \cos\left(k_{c,\mathrm{II}} \frac{a}{2}\right). \tag{5.86}$$

After the division of Eq. 5.85 by Eq. 5.86, we obtain the dispersion relation for a periodic dielectric slab waveguide, which is given by

$$-\frac{k_{c,\mathrm{I}}}{\epsilon_{\mathrm{I}}} \tan\left(k_{c,\mathrm{I}} \frac{s}{2}\right) = \frac{k_{c,\mathrm{II}}}{\epsilon_{\mathrm{II}}} \tan\left(k_{c,\mathrm{II}} \frac{a}{2}\right). \tag{5.87}$$

Finally, by using the electromagnetic boundary conditions, see Eq. 5.59, and the periodicity of the fields with Λ, one obtains

$$B_1 = \cos\left(k_{c,\mathrm{II}} \frac{a}{2}\right). \tag{5.88a}$$

$$B_2 = \cos\left(k_{c,\mathrm{I}} \frac{s}{2}\right). \tag{5.88b}$$

It is also noteworthy that the dispersion relation given in Eq. 5.87 ensures the satisfaction of the electromagnetic boundary conditions.

5.4.2 TE Modes

Here, we assume that the incident plane wave propagates in the $+z$ direction with $E_{y,i} = 0$, $H_{x,i} = 0$, $E_{x,i} \neq 0$, and $H_{y,i} \neq 0$. Such a wave can excite a TE mode of the periodic dielectric slab waveguide, see Eqs. 5.54 and 5.55.

Since the rest of the derivation is very similar to that of the TM modes, we will not repeat the assumptions and the details of the calculations. Firstly, we write the vector potential $\mathbf{F}$ for regions I and II as follows:

$$F_z^{\mathrm{I}} = B_1 \sin\left\{k_{c,\mathrm{I}} \left[y - (\Lambda + a)/2\right]\right\} e^{-i\beta z}. \tag{5.89a}$$

$$F_z^{\mathrm{II}} = B_2 \sin\left[k_{c,\mathrm{II}} (y - a/2)\right] e^{-i\beta z}. \tag{5.89b}$$

From Eqs. 5.54 and 5.55, we obtain

$$H_z^{\mathrm{I}} = -i\frac{k_{c,\mathrm{I}}^2}{w\mu_0\epsilon_{\mathrm{I}}} B_1 \sin\left\{k_{c,\mathrm{I}}\left[y-(\Lambda+a)/2\right]\right\} e^{-i\beta z} \tag{5.90a}$$

$$H_z^{\mathrm{II}} = -i\frac{k_{c,\mathrm{II}}^2}{w\mu_0\epsilon_{\mathrm{II}}} B_2 \sin\left[k_{c,\mathrm{II}}(y-a/2)\right] e^{-i\beta z} \tag{5.90b}$$

and

$$E_x^{\mathrm{I}} = -\frac{k_{c,\mathrm{I}}}{\epsilon_{\mathrm{I}}} B_1 \cos\left\{k_{c,\mathrm{I}}\left[y-(\Lambda+a)/2\right]\right\} e^{-i\beta z}. \tag{5.91a}$$

$$E_x^{\mathrm{II}} = -\frac{k_{c,\mathrm{II}}}{\epsilon_{\mathrm{II}}} B_2 \cos\left[k_{c,\mathrm{II}}(y-a/2)\right] e^{-i\beta z}. \tag{5.91b}$$

For TE waves, the periodic boundary conditions assumes the following form:

$$H_z^{\mathrm{I}}(y=\Lambda) = H_z^{\mathrm{II}}(y=0). \tag{5.92a}$$

$$E_x^{\mathrm{I}}(y=\Lambda) = E_x^{\mathrm{II}}(y=0). \tag{5.92b}$$

Application of Eq. 5.92 on Eqs. 5.90 and 5.91 yields

$$-\frac{k_{c,\mathrm{I}}^2}{\epsilon_{\mathrm{I}}} B_1 \sin\left(k_{c,\mathrm{I}}\frac{s}{2}\right) = \frac{k_{c,\mathrm{II}}^2}{\epsilon_{\mathrm{II}}} B_2 \sin\left(k_{c,\mathrm{II}}\frac{a}{2}\right). \tag{5.93a}$$

$$\frac{k_{c,\mathrm{I}}}{\epsilon_{\mathrm{I}}} B_1 \cos\left(k_{c,\mathrm{I}}\frac{s}{2}\right) = \frac{k_{c,\mathrm{II}}}{\epsilon_{\mathrm{II}}} B_2 \cos\left(k_{c,\mathrm{II}}\frac{a}{2}\right). \tag{5.93b}$$

For TE modes inside a periodic dielectric slab waveguide, the following dispersion relation is achieved by dividing Eq. 5.93(a) by Eq. 5.93(b):

$$-k_{c,\mathrm{I}} \tan\left(k_{c,\mathrm{I}}\frac{s}{2}\right) = k_{c,\mathrm{II}} \tan\left(k_{c,\mathrm{II}}\frac{a}{2}\right). \tag{5.94}$$

Also for TE waves, B_1 and B_2 assume the form given in Eq. 5.88. Finally, the dispersion relation given in Eq. 5.94 ensures the satisfaction of the electromagnetic boundary conditions given in Eq. 5.73.

Chapter 6

High-Contrast Gratings

6.1 Introduction

High-contrast gratings (HCGs), which are composed of high refractive index gratings with a subwavelength periodicity enclosed by low refractive index materials [89], have been notably studied since the numerical [90] and experimental [91] revelation of their diffraction-free and broadband high-reflectivity regimes. The most notable and intriguing properties of HCGs include large fabrication tolerance, geometrical simplicity, and design flexibility [92]. In addition, their well-established theoretical descriptions [93, 94] also contribute to the enabling of benefiting from HCGs for the purpose of designing various optical devices, i.e., polarization-independent broadband reflectors [95], polarizing beam splitters [96], saturable and cavity-enhanced absorbers [97,98], monolithic high-reflectivity cavity mirrors [99], planar lenses and reflectors with high focusing abilities [100,101], high quality-factor Fabry-Perot resonators [102], vertical-cavity surface emitting and nano-electromechanical lasers [103,104], slow light waveguides [105], and one-, two- and three- dimensional hollow-core low-loss optical waveguides [106–108].

This chapter intends to, first, give a rigorous and detailed theoretical interpretation of HCGs by benefiting from Refs. [93,94] and, then, continue with our HCG based near-infrared broadband quarter-wave plate designs. We will introduce two distinct but similar designs, where the first one is analyzed purely theoretically

and numerically, and, by using the second one, we experimentally demonstrate the quarter-wave plate regime that is centered at $\lambda_0 = 1.55$ μm.

6.2 Theory

For the purpose of understanding the responses of HCGs to a particular incident field, i.e., a normally incident plane wave, a rigorous description of the electromagnetic fields inside and outside the grating region is mandatory. Although rigorous coupled-wave analysis (RCWA) [109, 110] proves to be extremely useful for computing the response of HCGs to an incident plane wave, i.e., the obtaining of reflection and transmission coefficients, and electric and magnetic field distributions everywhere, it does not give enough information about the nature of the fields inside the grating region, i.e., longitudinal and lateral wavevectors, reflection matrix from the interfaces, and phase gain through propagation inside the medium. Therefore, in this section, we will give a fully rigorous electromagnetic solution for the existing waveguide modes inside HCGs. The analysis presented here is adapted from Refs. [93, 94].

The geometry of a generic HCG is depicted in Fig. 6.1. For simplifying the theoretical analysis, we assume that the material constituting regions I and III, and the grooves in region II is free-space. In the subsequent analysis, we will directly use the dispersion relations derived for the periodic dielectric slab waveguide, see Sec. 5.4. In order to be compliant with the literature, different from Sec. 5.4, we use the coordinate system shown in Fig. 6.1. This change of the unit vectors is arbitrary and does not affect the results. If one desires to utilize the coordinate system used in the aforementioned section, the following interchanging operations of the unit vectors are required: $\hat{\mathbf{x}} \rightarrow -\hat{\mathbf{y}}$ and $\hat{\mathbf{y}} \rightarrow \hat{\mathbf{x}}$.

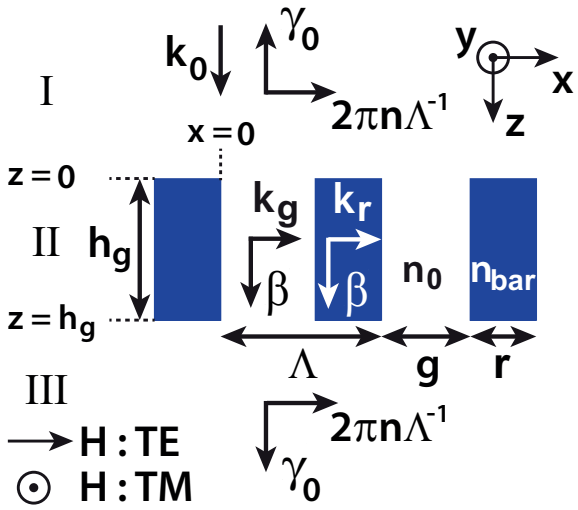

Figure 6.1: A generic HCG geometry. The structure is assumed to be infinitely periodic in the x direction. For simplicity, the material constituting regions I and III, and the grooves in region II is assumed to be free-space. Note that the HCG geometry is very similar to what is shown in Fig. 5.3 except that, now, the periodic dielectric slab waveguide is truncated from both ends at $z = 0$ and $z = h_g$. Reprinted with permission from [111]. Copyright 2012 by the Optical Society of America.

6.2.1 TM Modes

The magnetic field in region I ($z < 0$) can be described as the sum of the incident wave and the reflected diffraction orders as follows:

$$H_y^{\mathrm{I}}(x,z) = \underbrace{e^{-ik_0 z}}_{\text{incident wave}} \underbrace{- \sum_{n=0}^{\infty} r_n \mathcal{H}_{y,n}^{\mathrm{I}}(x) e^{i\gamma_n z}}_{\text{reflected wave}}, \quad n = 0, 1, 2, ... \tag{6.1}$$

where n denotes the diffraction order. r_n and

$$\gamma_n = \sqrt{k_0^2 - (2n\pi\Lambda^{-1})^2} \tag{6.2}$$

are the reflection coefficient and the propagation constant of the n^{th} diffraction order, respectively. Since $\Lambda < \lambda_0$ for HCGs, it is seen from Eq. 6.2 that only γ_0 is positive, whereas γ_n is purely imaginary for all other higher diffraction orders. In other words, in the farfield, only zeroth reflection and transmission orders are

observed, whereas the higher orders decay exponentially as we get further from the structure along the z–axis. Finally, $\mathcal{H}^{\mathrm{I}}_{y,n}(x)$ symbolizes the lateral magnetic field distribution of the n^{th} diffraction order in region I. Next, the electric field distribution in region I can be expressed as:

$$E^{\mathrm{I}}_{x}(x,z) = Z_{\mathrm{TEM}} e^{-ik_0 z} + \sum_{n=0}^{\infty} r_n Z_{\mathrm{TM}} \mathcal{H}^{\mathrm{I}}_{y,n}(x) e^{i\gamma_n z}, \tag{6.3}$$

where $Z_{\mathrm{TEM}} = \sqrt{\mu_0}/\sqrt{\epsilon_0}$, see Sec. 5.2.2, and $Z_{\mathrm{TM}} = (\gamma_n/k_0)\sqrt{\mu_0}/\sqrt{\epsilon_0}$, see Sec. 5.2.4. For simplicity, we can define

$$\mathcal{E}^{\mathrm{I}}_{x,n}(x) = Z_{\mathrm{TM}} \mathcal{H}^{\mathrm{I}}_{y,n}(x), \tag{6.4}$$

where $\mathcal{E}^{\mathrm{I}}_{x,n}(x)$ denotes the lateral electric field distribution of the n^{th} diffraction order in region I. Afterwards, by taking the even symmetry of the incident magnetic field and the HCG structure with respect to $x = g/2$ into account, we note that $\mathcal{H}^{\mathrm{I}}_{y,n}(x)$ must exhibit even symmetry with respect to $x = g/2$ and be periodic with Λ. Therefore, in the most suitable form, we define

$$\mathcal{H}^{\mathrm{I}}_{y,n}(x) = \cos[(2n\pi\Lambda^{-1})(x - g/2)]. \tag{6.5}$$

It is important to note that the plane of symmetry is taken as $x = g/2$ in writing Eq. 6.5. Instead, one can write the same equation by assuming that the symmetry plane is $x = g + r/2$ and the results should be exactly the same. In that case, we have

$$\mathcal{H}^{\mathrm{I}}_{y,n}(x) = \cos[(2n\pi\Lambda^{-1})(x - g - r/2)]. \tag{6.6}$$

However, in this chapter, we will follow the definition given in Eq. 6.5 only due to its simplicity compared to Eq. 6.6. Next, by using a similar approach to Eq. 6.1, one can write the transmitted magnetic field in region III ($z > h_g$) as follows:

$$H^{\mathrm{III}}_{y}(x,z) = \sum_{n=0}^{\infty} \tau_n \mathcal{H}^{\mathrm{III}}_{y,n}(x) e^{-i\gamma_n (z - h_g)}, \tag{6.7}$$

where τ_n denotes the transmission coefficient of the n^{th} diffraction order. In Eq. 6.7, the choice of the spatial coordinate in the exponent is quite arbitrary and we

choose to write $z - h_g$ in order to ease the matching of the boundary conditions at $z = h_g$ since the exponential term becomes unity at this boundary. Now, we also know that the electric field distribution in region III is given by

$$E_x^{\mathrm{III}}(x,z) = \sum_{n=0}^{\infty} \tau_n Z_{\mathrm{TM}} \mathcal{H}_{y,n}^{\mathrm{III}}(x) e^{-i\gamma_n (z-h_g)}. \tag{6.8}$$

For definiteness, we define $\mathcal{E}_{x,n}^{\mathrm{III}}(x) = Z_{\mathrm{TM}} \mathcal{H}_{y,n}^{\mathrm{III}}(x)$. It is worthwhile noting that, as a result of the selection of the same material for regions I and III, the propagation constant, γ_n, is equal in both regions.

Using a modal approach, the incident wave in region I can be expressed by using the vector $(1 \quad 0 \quad 0 \quad ...)^T$. Here, each element of this vector denotes the magnitude of a particular diffraction order depending on the index of the corresponding vector element, i.e., the first and second elements denote the zeroth and first diffraction orders, respectively, and so on. Using a similar approach, one can define the HCG reflection matrix, $\mathbf{R}$, and transmission matrix, $\mathbf{T}$, in terms of r_n and τ_n as follows:

$$\mathbf{r} \equiv (r_0 \quad r_1 \quad r_2 \quad ...) \equiv \mathbf{R}(1 \quad 0 \quad 0 \quad ...)^T, \tag{6.9a}$$

$$\boldsymbol{\tau} \equiv (\tau_0 \quad \tau_1 \quad \tau_2 \quad ...) \equiv \mathbf{T}(1 \quad 0 \quad 0 \quad ...)^T. \tag{6.9b}$$

In Sec. 5.4, we assumed that the waveguide modes propagate only in the $+z$ direction. This assumption does not result in loss of generality since the waveguide is assumed to be infinite and, therefore, reflection from the ends of the waveguide does not occur. However, in the case of HCGs, we have to take the reflection from the ends of the waveguide, i.e., $z = 0$ and $z = h_g$, into account. Correspondingly, we write the magnetic field inside the HCG region (region II) as a superposition of $+z$ and $-z$ propagating waves as follows:

$$H_y^{\mathrm{II}}(x,z) = \sum_{m=0}^{\infty} \mathcal{H}_{y,m}^{\mathrm{II}}(x) \left[a_m e^{-i\beta_m (z-h_g)} - a_m^{\rho} e^{i\beta_m (z-h_g)} \right], \tag{6.10}$$

where m and β_m denote the mode number inside the waveguide and the propagation constant for the corresponding mode, respectively. Plus, a_m and a_m^{ρ} denote

the magnitudes of the $+z$ and $-z$ propagating waves in region II, respectively. By using Eqs. 5.83 and 5.88, one can easily write $\mathcal{H}^{\mathrm{II}}_{y,m}(x)$ in the following form:

$$\mathcal{H}^{\mathrm{II}}_{y,m}(x \ : \ 0<x<g) = \cos\left(k_{r,m}r/2\right)\cos\left[k_{g,m}(x-g/2)\right], \tag{6.11a}$$

$$\mathcal{H}^{\mathrm{II}}_{y,m}(x \ : \ g<x<\Lambda) = \cos\left(k_{g,m}g/2\right)\cos\left\{k_{r,m}\left[y-(\Lambda+g)/2\right]\right\}. \tag{6.11b}$$

By using Eq. 5.32, we express the electric field in region II as

$$E^{\mathrm{II}}_{x}(x,z) = \sum_{m=0}^{\infty} \mathcal{E}^{\mathrm{II}}_{x,m}(x)\left[a_m e^{-i\beta_m(z-h_g)} + a^{\rho}_m e^{i\beta_m(z-h_g)}\right]. \tag{6.12}$$

Having shown that $Z_{\mathrm{TM}} = \beta/(w\epsilon)$, see Sec. 5.2.4, $\mathcal{E}^{\mathrm{II}}_{x,m}$ is expressed as

$$\mathcal{E}^{\mathrm{II}}_{x,m}(x \ : \ 0<x<g) = \frac{\beta_m}{k_0}\sqrt{\frac{\mu_0}{\epsilon_0}}\mathcal{H}^{\mathrm{II}}_{y,m}(x \ : \ 0<x<g), \tag{6.13a}$$

$$\mathcal{E}^{\mathrm{II}}_{x,m}(x \ : \ g<x<\Lambda) = \frac{\beta_m}{k_0}\frac{1}{n^2_{bar}}\sqrt{\frac{\mu_0}{\epsilon_0}}\mathcal{H}^{\mathrm{II}}_{y,m}(x \ : \ g<x<\Lambda). \tag{6.13b}$$

The propagation constants of the waveguide modes can be calculated by

$$\beta^2_m = (2\pi\lambda^{-1})^2 - k^2_{g,m} = (2\pi n_{bar}\lambda^{-1})^2 - k^2_{r,m} \tag{6.14}$$

and, therefore, we can relate $k_{g,m}$ and $k_{r,m}$ as follows:

$$k^2_{r,m} - k^2_{g,m} = (2\pi\lambda^{-1})^2(n^2_{bar}-1). \tag{6.15}$$

Recalling the dispersion equation we have derived for TM modes inside a periodic dielectric slab waveguide, see Eq. 5.87, we also have

$$-\frac{k_{r,m}}{n^2_{bar}}\tan\left(k_{r,m}\frac{r}{2}\right) = k_{g,m}\tan\left(k_{g,m}\frac{g}{2}\right). \tag{6.16}$$

Equation 6.16 is extremely important for the theoretical analysis of HCGs and we have devoted an entire chapter, see Chapter 5, for being able to derive this dispersion relation with a solid electromagnetics background. Since Eqs. 6.15 and 6.16 form an equation system with two unknowns, for the rigorous analysis of a particular HCG geometry, one needs to solve this equation system and determine

the values of $k_{r,m}$ and $k_{g,m}$ for $m = 0, 1, 2, ...$

Now, let us turn our attention to Eq. 6.10, where we define a_m and a_m^ρ. Assume that an HCG is illuminated by a plane wave that excites only the TM modes inside the structure. The corresponding waveguide modes are reflected from the boundaries, $z = 0$ and $z = h_g$, as a result of the impedance mismatch between the TM waveguide modes in region II and the TEM waves in regions I and III. As a result of this reflection, here, a_m and a_m^ρ denote the coefficients of the $+z$ and $-z$ propagating modes. By using the vector formulation we used in Eq. 6.9, we can write

$$\mathbf{a} \equiv (a_0 \quad a_1 \quad a_2 \quad ...)^T, \tag{6.17a}$$

$$\mathbf{a^\rho} \equiv (a_0^\rho \quad a_1^\rho \quad a_2^\rho \quad ...)^T. \tag{6.17b}$$

We can relate $\mathbf{a}$ and $\mathbf{a^\rho}$ with the aid of a square reflection matrix, $\boldsymbol{\rho}$, which shows the characteristics of reflection at $z = 0$ boundary, as follows:

$$\mathbf{a^\rho} = \boldsymbol{\rho}\mathbf{a}. \tag{6.18}$$

The reflection matrix, $\boldsymbol{\rho}$, is generally nondiagonal for HCGs. In other words, upon reflection from a boundary, the waveguide modes can couple into each other. In spite of the fact that the waveguide modes are orthogonal, meaning that

$$\int_0^\Lambda \mathcal{H}_{y,j}^{\mathrm{II}}(x)\mathcal{H}_{y,k}^{\mathrm{II}}(x)dx = 0 \quad \text{for } j \neq k, \tag{6.19}$$

the modes can couple into each other upon reflection via interaction with the external modes of regions I and III.

Furthermore, the definition of a propagation matrix, $\boldsymbol{\varphi}$, is necessary in order to calculate the accumulated phase for each mode upon propagation from $z = 0$ to $z = h_g$. Note that $\boldsymbol{\varphi}$ is a diagonal square matrix due to the fact that the modes

do not couple into each other during propagation and is defined as

$$\boldsymbol{\varphi}_{j,k} = \begin{cases} e^{-i\beta_m h_g} & \text{for } j = k \\ 0 & \text{otherwise} \end{cases}. \tag{6.20}$$

The next step is to satisfy the electromagnetic boundary conditions at $z = 0$ and $z = h_g$ for the purpose of determining $\boldsymbol{\rho}$. We first start with the HCG/air interface at $z = h_g$ by noting that the tangential electric (E_x) and tangential magnetic (H_y) fields must be continuous across the boundary. Accordingly, we write

$$\sum_{m=0}^{\infty} \mathcal{H}_{y,m}^{\mathrm{II}}(x)\,(a_m - a_m^{\rho}) = \sum_{n=0}^{\infty} \tau_n \mathcal{H}_{y,n}^{\mathrm{III}}(x), \tag{6.21a}$$

$$\sum_{m=0}^{\infty} \mathcal{E}_{x,m}^{\mathrm{II}}(x)\,(a_m + a_m^{\rho}) = \sum_{n=0}^{\infty} \tau_n \mathcal{E}_{x,n}^{\mathrm{III}}(x). \tag{6.21b}$$

By performing a Fourier overlap integral on both sides of Eq. 6.21, we obtain

$$\sum_{m=0}^{\infty} (a_m - a_m^{\rho})\,\Lambda^{-1} \int_0^{\Lambda} \mathcal{H}_{y,m}^{\mathrm{II}}(x)\mathcal{H}_{y,n}^{\mathrm{III}}(x)dx = \tau_n \Lambda^{-1} \int_0^{\Lambda} [\mathcal{H}_{y,n}^{\mathrm{III}}(x)]^2 dx, \tag{6.22a}$$

$$\sum_{m=0}^{\infty} (a_m + a_m^{\rho})\,\Lambda^{-1} \int_0^{\Lambda} \mathcal{E}_{x,m}^{\mathrm{II}}(x)\mathcal{E}_{x,n}^{\mathrm{III}}(x)dx = \tau_n \Lambda^{-1} \int_0^{\Lambda} [\mathcal{E}_{x,n}^{\mathrm{III}}(x)]^2 dx. \tag{6.22b}$$

Afterwards, by noting that

$$\mathcal{H}_{y,n}^{\mathrm{III}}(x) = \mathcal{H}_{y,n}^{\mathrm{I}}(x) = \cos[(2n\pi\Lambda^{-1})(x - g/2)], \tag{6.23}$$

one can easily obtain the following result:

$$\int_0^{\Lambda} [\mathcal{H}_{y,n}^{\mathrm{III}}(x)]^2 dx = \int_0^{\Lambda} \left\{\cos[(2n\pi\Lambda^{-1})(x - g/2)]\right\}^2 dx = \frac{\Lambda}{2 - \delta_{n,0}}, \tag{6.24}$$

where $\delta_{n,0}$ is the Kronecker delta function, which is defined as

$$\delta_{n,0} = \begin{cases} 1, & \text{if } n = 0 \\ 0, & \text{if } n \neq 0 \end{cases}. \tag{6.25}$$

Next, by defining the unitless overlap matrices $\mathbf{H}$ and $\mathbf{E}$ as follows:

$$\mathbf{H} = \boldsymbol{\tau} \left(\mathbf{a} - \mathbf{a}^{\boldsymbol{\rho}}\right)^{-1}, \tag{6.26a}$$

$$\mathbf{E} = \boldsymbol{\tau} \left(\mathbf{a} + \mathbf{a}^{\boldsymbol{\rho}}\right)^{-1}, \tag{6.26b}$$

Eq. 6.22(a) can be rewritten in the following form:

$$\mathbf{H}_{n,m} = \Lambda^{-1}(2 - \delta_{n,0}) \int_0^{\Lambda} \mathcal{H}^{\mathrm{II}}_{y,m}(x)\mathcal{H}^{\mathrm{III}}_{y,n}(x)dx. \tag{6.27}$$

By following a similar analysis, Eq. 6.22(b) can be rewritten as

$$\mathbf{E}_{n,m} = \Lambda^{-1}(2 - \delta_{n,0}) \left(\frac{\gamma_n}{k_0}\sqrt{\frac{\mu_0}{\epsilon_0}}\right)^{-2} \int_0^{\Lambda} \mathcal{E}^{\mathrm{II}}_{x,m}(x)\mathcal{E}^{\mathrm{III}}_{x,n}(x)dx. \tag{6.28}$$

Now, by using Eqs. 6.18 and 6.26, we write

$$\boldsymbol{\tau} = \mathbf{H}(\mathbf{I} - \boldsymbol{\rho})\mathbf{a} = \mathbf{E}(\mathbf{I} + \boldsymbol{\rho})\mathbf{a}. \tag{6.29}$$

Using Eq. 6.29, the reflection matrix, $\boldsymbol{\rho}$, can be written in terms of $\mathbf{E}$ and $\mathbf{H}$ as follows:

$$\boldsymbol{\rho} = (\mathbf{I} + \mathbf{H}^{-1}\mathbf{E})^{-1}(\mathbf{I} - \mathbf{H}^{-1}\mathbf{E}). \tag{6.30}$$

Eq. 6.30 is the main result coming from the application of the boundary conditions at $z = h_g$. Next, by using Eqs. 6.1, 6.3, 6.10, and 6.12, we match the

boundary conditions at the input interface, $z = 0$, as follows:

$$\sum_{n=0}^{\infty}(\delta_{n,0} - r_n)\mathcal{H}^{\mathrm{I}}_{y,n}(x) = \sum_{m=0}^{\infty}\mathcal{H}^{\mathrm{II}}_{y,m}(x)\left[a_m e^{i\beta_m h_g} - a^{\rho}_m e^{-i\beta_m h_g}\right], \tag{6.31a}$$

$$\sum_{n=0}^{\infty}(\delta_{n,0} + r_n)\mathcal{E}^{\mathrm{I}}_{x,n}(x) = \sum_{m=0}^{\infty}\mathcal{E}^{\mathrm{II}}_{x,m}(x)\left[a_m e^{i\beta_m h_g} + a^{\rho}_m e^{-i\beta_m h_g}\right]. \tag{6.31b}$$

If one performs Fourier overlap integral on both sides of Eq. 6.31 and, then, define $\mathbf{H}$ and $\mathbf{E}$ as in Eq. 6.26, the following equation is achieved after simple matrix algebra:

$$(\mathbf{I} - \mathbf{R})^{-1}\mathbf{H}(\mathbf{I} - \boldsymbol{\varphi}\boldsymbol{\rho}\boldsymbol{\varphi}) = (\mathbf{I} + \mathbf{R})^{-1}\mathbf{E}(\mathbf{I} + \boldsymbol{\varphi}\boldsymbol{\rho}\boldsymbol{\varphi}). \tag{6.32}$$

By rearranging the terms in Eq. 6.32 and being in harmony with the microwave electronics terminology, we write

$$\mathbf{Z_{in}} \equiv (\mathbf{I} + \mathbf{R})(\mathbf{I} - \mathbf{R})^{-1} = \mathbf{E}(\mathbf{I} + \boldsymbol{\varphi}\boldsymbol{\rho}\boldsymbol{\varphi})(\mathbf{I} - \boldsymbol{\varphi}\boldsymbol{\rho}\boldsymbol{\varphi})^{-1}\mathbf{H}^{-1}. \tag{6.33}$$

Note that, in contrast to the traditional transmission line theory [87], here, $\mathbf{Z_{in}}$ is a square matrix. Finally, by rearranging Eq. 6.33, we obtain

$$\mathbf{R} = (\mathbf{Z_{in}} + \mathbf{I})^{-1}(\mathbf{Z_{in}} - \mathbf{I}). \tag{6.34}$$

By using a similar approach, one can easily show that the coefficient vector, $\mathbf{a}$, can be expressed as

$$\mathbf{a} = 2\boldsymbol{\varphi}\left[(\mathbf{Z}^{-1}_{\mathbf{in}} + \mathbf{I})\mathbf{E}(\mathbf{I} + \boldsymbol{\varphi}\boldsymbol{\rho}\boldsymbol{\varphi})\right]^{-1}(1 \quad 0 \quad 0 \quad ...)^T. \tag{6.35}$$

Finally, by using Eq. 6.29, one can write the transmission matrix, $\mathbf{T}$, as follows:

$$\mathbf{T} = 2\mathbf{E}(\mathbf{I} + \boldsymbol{\rho})\boldsymbol{\varphi}\left[(\mathbf{Z}^{-1}_{\mathbf{in}} + \mathbf{I})\mathbf{E}(\mathbf{I} + \boldsymbol{\varphi}\boldsymbol{\rho}\boldsymbol{\varphi})\right]^{-1}. \tag{6.36}$$

As we have mentioned before, γ_n is real for only $n = 0$ since, for HCGs, we have $\Lambda < \lambda$, see Eq. 6.2. For $n \neq 0$, we have purely imaginary γ_n values, which correspond to exponentially decaying modes. Therefore, reflection and transmission to the farfield occur only in the zeroth diffraction orders. Thus, the

intensity reflection and transmission coefficients are given by $|\mathbf{R}_{00}|^2$ and $|\mathbf{T}_{00}|^2$, respectively, where the subscripts denote the indices of the corresponding matrix element. As stated by the conservation of energy principle, for a system consisting of only lossless dielectrics, we have

$$|\mathbf{R}_{00}|^2 + |\mathbf{T}_{00}|^2 = 1. \tag{6.37}$$

6.2.2 TE Modes

For TE modes, we can write the magnetic field distribution in region I as

$$H_x^{\mathrm{I}}(x,z) = \underbrace{e^{-ik_0 z}}_{\text{incident wave}} \underbrace{- \sum_{n=0}^{\infty} r_n \mathcal{H}_{x,n}^{\mathrm{I}}(x) e^{i\gamma_n z}}_{\text{reflected wave}}, \tag{6.38}$$

where γ_n is defined as given in Eq. 6.2. Using Eq. 6.38, one can express the electric field distribution in region I as follows:

$$E_y^{\mathrm{I}}(x,z) = -Z_{\mathrm{TEM}} e^{-ik_0 z} - \sum_{n=0}^{\infty} r_n Z_{\mathrm{TE}} \mathcal{H}_{x,n}^{\mathrm{I}}(x) e^{i\gamma_n z}, \tag{6.39}$$

where $Z_{\mathrm{TEM}} = \sqrt{\mu_0}/\sqrt{\epsilon_0}$ and $Z_{\mathrm{TE}} = (k_0/\gamma_n)\sqrt{\mu_0}/\sqrt{\epsilon_0}$, see Sec. 5.2.3. For simplicity, similar to what we have done during the analysis of TM modes, we can define

$$\mathcal{E}_{y,n}^{\mathrm{I}}(x) = Z_{\mathrm{TE}} \mathcal{H}_{x,n}^{\mathrm{I}}(x). \tag{6.40}$$

$\mathcal{H}_{x,n}^{\mathrm{I}}(x)$ is very similar to $\mathcal{H}_{y,n}^{\mathrm{I}}(x)$, which is defined for TM modes, and is written as

$$\mathcal{H}_{x,n}^{\mathrm{I}}(x) = \cos[(2n\pi\Lambda^{-1})(x - g/2)]. \tag{6.41}$$

Using a similar approach to Eq. 6.38, one can express the magnetic field distribution in region III as follows:

$$H_x^{\mathrm{III}}(x,z) = \sum_{n=0}^{\infty} \tau_n \mathcal{H}_{x,n}^{\mathrm{III}}(x) e^{-i\gamma_n (z - h_g)}. \tag{6.42}$$

By utilizing Eq. 5.18, one can write the electric field distribution in region III as

$$E_y^{\mathrm{III}}(x,z) = -\sum_{n=0}^{\infty} \tau_n Z_{\mathrm{TE}} \mathcal{H}_{x,n}^{\mathrm{III}}(x) e^{-i\gamma_n (z-h_g)}. \tag{6.43}$$

Similar to Eq. 6.40, we define

$$\mathcal{E}_{y,n}^{\mathrm{III}}(x) = Z_{\mathrm{TE}} \mathcal{H}_{x,n}^{\mathrm{III}}(x). \tag{6.44}$$

Next, by considering the $+z$ and $-z$ propagating waves in region II, we write the magnetic field distribution inside the HCG as

$$H_x^{\mathrm{II}}(x,z) = \sum_{m=0}^{\infty} \mathcal{H}_{x,m}^{\mathrm{II}}(x) \left[a_m e^{-i\beta_m (z-h_g)} - a_m^{\rho} e^{i\beta_m (z-h_g)} \right]. \tag{6.45}$$

By using Eqs. 5.88 and 5.90, one can easily express $\mathcal{H}_{x,m}^{\mathrm{II}}(x)$ in the following form:

$$\mathcal{H}_{x,m}^{\mathrm{II}}(x \ : \ 0 < x < g) = \cos\left(k_{r,m} r/2\right) \cos\left[k_{g,m}(x - g/2)\right], \tag{6.46a}$$

$$\mathcal{H}_{x,m}^{\mathrm{II}}(x \ : \ g < x < \Lambda) = \cos\left(k_{g,m} g/2\right) \cos\left\{k_{r,m}\left[y - (\Lambda + g)/2\right]\right\}. \tag{6.46b}$$

By employing Eq. 5.18, the electric field distribution in region II is written as

$$E_y^{\mathrm{II}}(x,z) = -\sum_{m=0}^{\infty} \mathcal{E}_{y,m}^{\mathrm{II}}(x) \left[a_m e^{-i\beta_m (z-h_g)} + a_m^{\rho} e^{i\beta_m (z-h_g)} \right]. \tag{6.47}$$

Having shown that $Z_{\mathrm{TE}} = w\mu_0/\beta$, see Sec. 5.2.3, $\mathcal{E}_{y,m}^{\mathrm{II}}(x)$ is given by

$$\mathcal{E}_{y,m}^{\mathrm{II}}(x) = \frac{k_0}{\beta_m} \sqrt{\frac{\mu_0}{\epsilon_0}} \mathcal{H}_{x,m}^{\mathrm{II}}(x). \tag{6.48}$$

The propagation constants of the waveguide modes can be easily calculated by

$$\beta_m^2 = (2\pi\lambda^{-1})^2 - k_{g,m}^2 = (2\pi n_{bar}\lambda^{-1})^2 - k_{r,m}^2 \tag{6.49}$$

and, therefore, we can relate $k_{g,m}$ and $k_{r,m}$ as follows:

$$k_{r,m}^2 - k_{g,m}^2 = (2\pi\lambda^{-1})^2(n_{bar}^2 - 1). \tag{6.50}$$

Recalling the dispersion relation we have derived for TE modes inside a periodic dielectric slab waveguide, see Eq. 5.94, we also have

$$-k_{r,m}\tan\left(k_{r,m}\frac{r}{2}\right) = k_{g,m}\tan\left(k_{g,m}\frac{g}{2}\right). \tag{6.51}$$

Eqs. 6.50 and 6.51 form an equation system with two unknowns and one can calculate k_r and k_g by using them. Subsequently, by matching the tangential electric and magnetic fields at $z = h_g$, and performing a Fourier overlap integral on both sides, we obtain

$$\sum_{m=0}^{\infty}(a_m - a_m^{\rho})\,\Lambda^{-1}\int_0^{\Lambda}\mathcal{H}_{x,m}^{\mathrm{II}}(x)\mathcal{H}_{x,n}^{\mathrm{III}}(x)dx = \tau_n\Lambda^{-1}\int_0^{\Lambda}[\mathcal{H}_{x,n}^{\mathrm{III}}(x)]^2dx, \tag{6.52a}$$

$$\sum_{m=0}^{\infty}(a_m + a_m^{\rho})\,\Lambda^{-1}\int_0^{\Lambda}\mathcal{E}_{y,m}^{\mathrm{II}}(x)\mathcal{E}_{y,n}^{\mathrm{III}}(x)dx = \tau_n\Lambda^{-1}\int_0^{\Lambda}[\mathcal{E}_{y,n}^{\mathrm{III}}(x)]^2dx. \tag{6.52b}$$

By using Eqs. 6.41 and 6.43, we evaluate

$$\int_0^{\Lambda}[\mathcal{H}_{x,n}^{\mathrm{III}}(x)]^2dx = \int_0^{\Lambda}\left\{\cos[(2n\pi\Lambda^{-1})(x-g/2)]\right\}^2dx = \frac{\Lambda}{2-\delta_{n,0}}, \tag{6.53a}$$

$$\int_0^{\Lambda}[\mathcal{E}_{y,n}^{\mathrm{III}}(x)]^2dx = Z_{\mathrm{TE}}^2\int_0^{\Lambda}[\mathcal{H}_{x,n}^{\mathrm{III}}(x)]^2dx = \left(\frac{k_0}{\gamma_n}\sqrt{\frac{\mu_0}{\epsilon_0}}\right)^2\frac{\Lambda}{2-\delta_{n,0}}. \tag{6.53b}$$

By using Eq. 6.53(a), Eq. 6.52(a) can be represented in the matrix form as follows:

$$\mathbf{H}_{n,m} = \Lambda^{-1}(2-\delta_{n,0})\int_0^{\Lambda}\mathcal{H}_{x,m}^{\mathrm{II}}(x)\mathcal{H}_{x,n}^{\mathrm{III}}(x)dx. \tag{6.54}$$

Next, Eq. 6.52(b) can also be converted to the matrix form with the aid of Eq. 6.53(b) and is expressed as

$$\mathbf{E}_{n,m} = \Lambda^{-1}(2-\delta_{n,0})\left(\frac{k_0}{\gamma_n}\sqrt{\frac{\mu_0}{\epsilon_0}}\right)^{-2}\int_0^{\Lambda}\mathcal{E}^{\mathrm{II}}_{x,m}(x)\mathcal{E}^{\mathrm{III}}_{x,n}(x)dx. \tag{6.55}$$

The rest of the analysis is the same as the TM mode analysis and, therefore, Eqs. 6.29 – 6.37 can be directly utilized for the theoretical analysis of TE modes.

6.3 Broadband Quarter-Wave Plates Using HCGs

In this section, we exploit the unique and intriguing properties of HCGs for the purpose of designing ultrathin and broadband quarter-wave plates operating at the near-infrared regime. Here, we investigate the transmission characteristics of two distinct designs; the first one being composed of silicon-dioxide and silicon, and the second one being composed of sapphire and silicon. The quarter-wave plate regime is achieved by the satisfaction of the following conditions at the central wavelength, $\lambda_0 = 1.55$ μm:

$$|T_{\mathrm{TM}}| \simeq |T_{\mathrm{TE}}|, \tag{6.56a}$$

$$\angle(T_{\mathrm{TM}}) - \angle(T_{\mathrm{TE}}) \simeq \pi/2, \tag{6.56b}$$

where T_{TM} and T_{TE} denote the transmission coefficients for normally incident TM and TE waves, respectively. Note that, in Eq. 6.56(b), the order of T_{TM} and T_{TE} is completely arbitrary and they can be interchanged. The choice provided in Eq. 6.56(b) results in the transmission of a right-hand circularly polarized wave when the structure is illuminated by a normally incident wave with a polarization plane angle of $\pi/4$ with respect to the x–axis in the first quadrant of the xy–plane.

As a result of the satisfaction of the operation conditions given in Eq. 6.56, a *unity* conversion efficiency from linear polarization to circular one is achieved

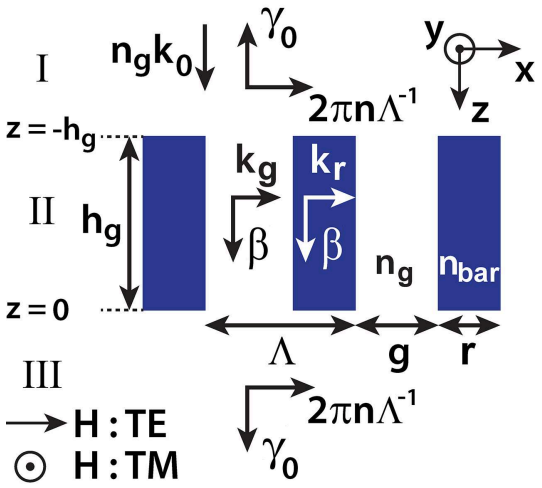

Figure 6.2: Geometrical description of the HCG quarter-wave plate. The dark regions indicate the presence of Si, whereas the white regions are SiO_2. Reprinted with permission from [111]. Copyright 2012 by the Optical Society of America.

at $\lambda_0 = 1.55$ μm. In the analysis of the first design, which we refer as *numerical design*, we show the achievement of the quarter-wave plate regime by using the theoretical approach, which is given in detail in Sec. 6.2, and RCWA [109, 110]. For the second design, which we refer as *experimental design*, the existence of the quarter-wave plate regime is demonstrated by performing finite-difference time-domain (FDTD) method based simulations (FDTD Solutions, Lumerical Inc.) and experimental measurements.

Numerical simulations, in which the dispersion of the material refractive indices is accounted properly, suggest that percent operation bandwidths of 51% and 42% are obtained for the numerical and experimental designs, respectively. On the other hand, experimental results, which are in good agreement with the numerical ones, show that the percent bandwidth of operation is 33% for the experimental design. Finally, it should be noted that, in this context, we define the operation range as the wavelength interval for which the conversion efficiency, C_{eff}, is equal to or larger than 0.9.

6.3.1 Theoretical Design

Firstly, we demonstrate a HCG based quarter-wave plate, where the design target is the maximization of the circular conversion efficiency at $\lambda_0 = 1.55$ μm, total transmission, and operation bandwidth. We base this subsection on Refs. [111, 112], which demonstrate and discuss the properties of the suggested theoretical design in detail. In spite of the fact that the proposed geometry can easily be represented by Fig. 6.1, for the sake of completeness, we show the proposed geometry in Fig. 6.2. We select the material filling the grooves in region II, and constituting regions I and III as silicon-dioxide. The material that constitutes the ridges in region II is selected as silicon due to its high refractive index and low absorption coefficient at $\lambda_0 = 1.55$ μm.

In the theoretical and numerical analysis stages, we assume that regions I and III extend to infinity in the $-z$ and $+z$ directions, respectively. This assumption greatly simplifies the theoretical and numerical modelling process and, in particular, prevents any reflection from the back-sides of the substrate and, therefore, excitation of Fabry-Perot type resonances inside regions I and III. The excitation of such modes might conduce to the modification of the reflection and transmission coefficients of the structure. In the practical realization stage, the infinite medium assumption inside regions I and III can be approximately satisfied by the utilization of a thick substrate, i.e., much thicker than the coherence length of the light source, and the fabrication of a multi-layered anti-reflection coating on the deposited SiO_2 film in region I.

In the subsequent parts of this subsection, we will first analyze the proposed geometry theoretically. Subsequently, we will present the circular conversion coefficients of the proposed design along with the conversion efficiency spectrum and bandwidth related discussions.

6.3.1.1 Theoretical Analysis

Firstly, we start the theoretical analysis of the theoretical design by deriving a closed form expression for the transmission coefficient for HCGs. It can be stated that, since $\Lambda < \lambda_0/n_g$, only the zeroth reflection and transmission orders are propagating modes, whereas the higher orders are exponentially decaying evanescent modes. Therefore, both transmission and reflection are related only to these zeroth reflection and transmission orders. Therefore, in order to calculate the transmission coefficient, one can only calculate τ_0 instead of calculating the complete $\mathbf{T}$ matrix. Using Eq. 6.9(b), one can easily show that $\mathbf{T}_{00} = \tau_0$. Moreover, by using Eq. 6.29, we can write

$$\tau_0 = \sum_m \mathbf{H}_{n=0,m} \left(a_m - a_m^{\rho}\right). \tag{6.57}$$

Using the definition of $\mathbf{H}_{n,m}$ for TM modes as given in Eq. 6.27, we obtain

$$T_{\mathrm{TM}} \equiv \tau_0 = \sum_m \left(a_m^{\mathrm{TM}} - a_m^{\rho,\mathrm{TM}}\right) \Lambda^{-1} \int_0^{\Lambda} \mathcal{H}_{y,m}^{\mathrm{II}}(x). \tag{6.58}$$

Similarly, if we use the definition of $\mathbf{H}_{n,m}$ for TE modes, see Eq. 6.54, we can write

$$T_{\mathrm{TE}} \equiv \tau_0 = \sum_m \left(a_m^{\mathrm{TE}} - a_m^{\rho,\mathrm{TE}}\right) \Lambda^{-1} \int_0^{\Lambda} \mathcal{H}_{x,m}^{\mathrm{II}}(x). \tag{6.59}$$

Noting that we also target transmitting as much power as possible, the condition given in Eq. 6.56(a) translates to

$$\left|\sum_m \left(a_m^{\mathrm{TM}} - a_m^{\rho,\mathrm{TM}}\right) \Lambda^{-1} \int_0^{\Lambda} \mathcal{H}_{y,m}^{\mathrm{II}}(x)\right| \simeq \left|\sum_m \left(a_m^{\mathrm{TE}} - a_m^{\rho,\mathrm{TE}}\right) \Lambda^{-1} \int_0^{\Lambda} \mathcal{H}_{x,m}^{\mathrm{II}}(x)\right| \simeq 1. \tag{6.60}$$

Similarly, the operation condition given in Eq. 6.56(b) can be rewritten as follows:

$$\angle\left(\sum_{m}\left(a_{m}^{\mathrm{TM}}-a_{m}^{\rho,\mathrm{TM}}\right)\Lambda^{-1}\int_{0}^{\Lambda}\mathcal{H}_{y,m}^{\mathrm{II}}(x)\right) - \angle\left(\sum_{m}\left(a_{m}^{\mathrm{TE}}-a_{m}^{\rho,\mathrm{TE}}\right)\Lambda^{-1}\int_{0}^{\Lambda}\mathcal{H}_{x,m}^{\mathrm{II}}(x)\right)\simeq\pi/2. \quad (6.61)$$

The next step in the theoretical analysis is to calculate the lateral and longitudinal wavenumbers of the excited TM and TE modes inside region II. We have provided a detailed and rigorous theoretical formulation for HCGs in Sec. 6.2. One can simply benefit from Eqs. 6.15 and 6.16 for the purpose of determining the wavenumbers of TM modes. Note that, here, Eq. 6.16 is slightly modified due to the existence of SiO_2 instead of free-space and the following is obtained:

$$-\frac{k_{r,m}}{n_{bar}^{2}}\tan\left(k_{r,m}\frac{r}{2}\right)=\frac{k_{g,m}}{n_{g}^{2}}\tan\left(k_{g,m}\frac{g}{2}\right). \quad (6.62)$$

Further, Eqs. 6.50 and 6.51 can be directly used for calculating the TE mode wavenumbers without any modification since TE modes are sensitive to μ rather than ϵ.

In evaluating the wavenumbers for TM and TE modes, we invoke an approximation such that only the first two modes, $m = 0$ and $m = 1$, are considered. This approximation is reasonable since, as it will be shown subsequently, for higher order modes, β_m is imaginary and $|\beta_m|$ is large, so that such modes decay very quickly and therefore, the contribution of these modes to the transmission and reflection coefficients is negligibly small. In the calculations, we take $n_{bar} = 3.48$ and $n_g = 1.47$ at $\lambda_0 = 1.55$ μm. Afterwards, by benefiting from a custom parametric optimization code written in MATLAB®, we search for the geometrical parameters for which Eqs. 6.60 and 6.61 are satisfied simultaneously.

Subsequent to running the optimization code, the optimal geometrical parameters for the achievement of quarter-wave plate regime are obtained as

$r = 160$ nm, $g = 220$ nm, and $h_g = 550$ nm. For these parameters, we calculate the lateral wavenumbers of the TM modes as follows: $k_{g,0}^2 = -4.2/\Lambda^2$, $k_{r,0}^2 = 19.43/\Lambda^2$ and $k_{g,1}^2 = 31.3/\Lambda^2$, $k_{r,1}^2 = 54.9/\Lambda^2$. A similar analysis for the TE modes yields $k_{g,0}^2 = -13.1/\Lambda^2$, $k_{r,0}^2 = 10.48/\Lambda^2$ and $k_{g,1}^2 = 30.2/\Lambda^2$, $k_{r,1}^2 = 53.8/\Lambda^2$. At this point, we recall that the waveguide cutoff condition corresponds to the point where $\beta = 0$ and, using Eq. 6.14, this condition translates to

$$k_r^2 = \left(\frac{n_{bar}}{n_g}\right)^2 k_g^2. \tag{6.63}$$

For the cases where $k_r^2 < (n_{bar}/n_g)^2 k_g^2$, we have purely imaginary β and, as a result, the mode decays exponentially with increasing distance. Accordingly, we see that $\mathrm{TM}_{m=0}$ and $\mathrm{TE}_{m=0}$ modes are propagating modes with real β, whereas $\mathrm{TM}_{m=1}$ and $\mathrm{TE}_{m=1}$ modes are evanescent modes. We repeat that, since $\lambda_0/n_g > \Lambda$ for HCGs ($\lambda_0 = 2.77 n_g \Lambda$ in this particular case) only the zeroth reflection and transmission orders correspond to propagating modes as implied by Eq. 6.2. The qualitative interpretation of this observation is that the reflected and transmitted waves propagate in the $-z$ and $+z$ directions, respectively, when the structure is illuminated by a normally incident plane wave propagating in the $+z$ direction.

The next step is to evaluate T_{TM} and T_{TE} using this theoretical approach. After using Eqs. 6.58 and 6.59 for this evaluation, we obtain $|T_{\mathrm{TM}}| = 0.988$ and $|T_{\mathrm{TE}}| = 0.936$. In addition, the phase difference between the transmitted TM and TE components is calculated as $\angle(T_{\mathrm{TM}}) - \angle(T_{\mathrm{TE}}) = 0.5111\pi = 92°$. These transmission coefficients show that the conditions required for the realization of the quarter-wave plate operation, which are given in Eq. 6.56, are satisfied by the proposed geometrical parameters.

In the final step of the theoretical analysis, under the two-mode approximation, we calculate the magnetic field distributions inside the grating region, i.e., $-h_g \leq z \leq 0$, for the purpose of demonstrating that the unequal lateral wavenumbers and propagation constants for TM and TE modes result in differing field distributions. This discrepancy originates from the fact that unequal wavenumbers and propagation constants conduce to unequal $\mathbf{a}$ and $\mathbf{a}^{\boldsymbol{\rho}}$ matrices and, in turn, unequal h_y^{II} and h_x^{II} vectors are obtained. The resultant magnetic

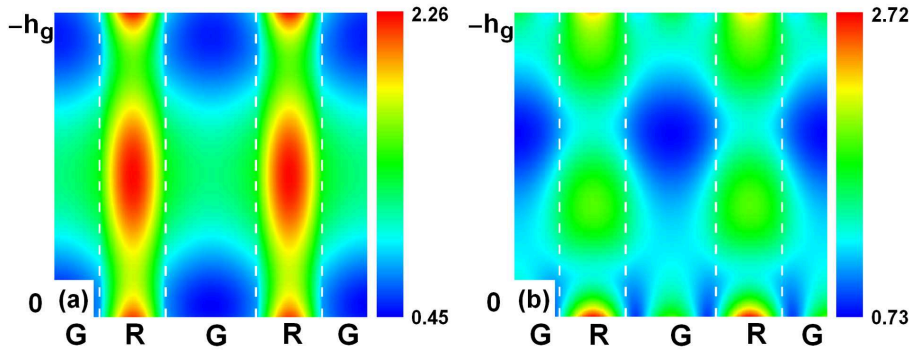

Figure 6.3: Normalized magnetic field distributions inside the grating region at $\lambda_0 = 1.55$ μm, (a) $|H_y^{\mathrm{II}}|/|H_0|$ and (b) $|H_x^{\mathrm{II}}|/|H_0|$ for TM and TE waves, respectively. Note that $|H_0|$ is the amplitude of the magnetic field component of the incident plane wave and assumed to be unity in the theoretical consideration. Ridges and grooves are separated by white dashed lines and denoted by R and G, respectively. Reprinted with permission from [111]. Copyright 2012 by the Optical Society of America.

field distributions are shown in Fig. 6.3. In other words, the excitation of TM and TE modes with unequal wavenumbers leads to the creation of an artificial birefringence.

6.3.1.2 Numerical Validation

For the purpose of verifying the theoretical predictions, we run RCWA [110] simulations in order to compute the transmission coefficients, T_{TM} and T_{TE}. Correspondingly, the amplitudes of the transmission coefficients and their phase difference are plotted in Fig. 6.4. It is noteworthy that, at $\lambda_0 = 1.55$ μm, we compute that $T_{\mathrm{TM}} \simeq T_{\mathrm{TE}}$ and, in addition, $\angle(T_{\mathrm{TM}}) - \angle(T_{\mathrm{TE}}) \simeq \pi/2$, which are compatible with the theoretical analysis performed in Sec. 6.3.1.1. Moreover, we predict that the achievement of $T_{\mathrm{TM}} \approx T_{\mathrm{TE}}$ in a wide wavelength range and the slow dispersion of the phase difference with respect to the wavelength can enable the obtaining of a broadband operation regime.

In order to analyze the operation regime of the proposed structure, we first define the circular conversion coefficients, C_- and C_+, which are a measure of the amplitudes of the left-hand circularly polarized (LCP, $-$) and right-hand

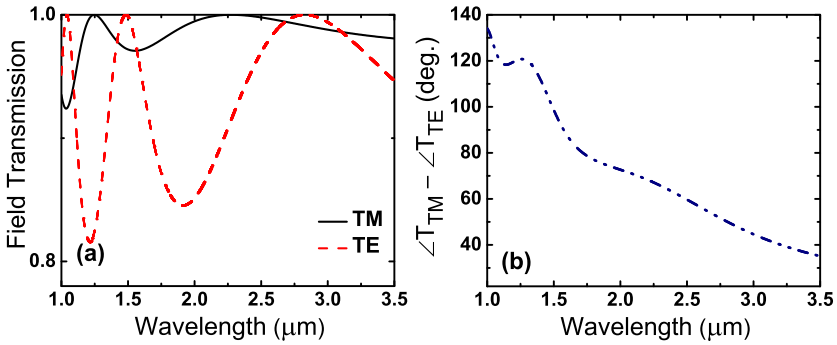

Figure 6.4: (a) Amplitude of the transmission coefficients for TM and TE waves calculated by using the RCWA and (b) the corresponding phase difference. Reprinted with permission from [111]. Copyright 2012 by the Optical Society of America.

circularly polarized (RCP, +) components of the transmitted waves. Note that we describe the incident wave as a plane wave with an electric field vector that makes an angle of $\pi/4$ with the x–axis in the first quadrant of the xy–plane. The circular conversion coefficients can be calculated as

$$C_{\pm} = \frac{1}{2}\left(T_{\mathrm{TM}} \mp iT_{\mathrm{TE}}\right). \tag{6.64}$$

Actually, the calculation of the circular conversion coefficients is a simple transformation of the base vectors from the linearly polarized waves to the circularly polarized ones. For instance, a transmitted wave can be decomposed in terms of its TM and TE polarized components by employing the Jones matrix formalism and the linear transmission coefficients as follows:

$$\begin{pmatrix} E_x^t \\ E_y^t \end{pmatrix} = \begin{pmatrix} T_{\mathrm{TM}} \\ T_{\mathrm{TE}} \end{pmatrix} = T_{\mathrm{TM}} \begin{pmatrix} 1 \\ 0 \end{pmatrix} + T_{\mathrm{TE}} \begin{pmatrix} 0 \\ 1 \end{pmatrix}, \tag{6.65}$$

where E_x^t and E_y^t denote the TM and TE components of the transmitted wave, respectively. In writing Eq. 6.65, we assume that optical activity is not present in the system. Then, we can decompose the transmitted wave given in Eq. 6.65 in the circular base as follows:

$$\begin{pmatrix} T_{\mathrm{TM}} \\ T_{\mathrm{TE}} \end{pmatrix} = C_{+} \begin{pmatrix} 1 \\ +i \end{pmatrix} + C_{-} \begin{pmatrix} 1 \\ -i \end{pmatrix}. \tag{6.66}$$

In solving Eq. 6.66 for C_+ and C_-, one arrives to Eq. 6.64. Afterwards, for being able to measure the degree of conversion from linear polarization to circular one, we define a circular conversion efficiency parameter, C_{eff}, which is described as

$$C_{\text{eff}} = \frac{|C_+|^2 - |C_-|^2}{|C_+|^2 + |C_-|^2}. \tag{6.67}$$

We also note that the ellipticity parameter, η, can be directly calculated with the knowledge of C_{eff} as

$$\eta = \arctan\left(\frac{\sqrt{(1 + C_{\text{eff}}) / (1 - C_{\text{eff}})} - 1}{\sqrt{(1 + C_{\text{eff}}) / (1 - C_{\text{eff}})} + 1}\right) \tag{6.68}$$

and the two parameters have one-to-one correspondence, i.e., knowing one of them implies knowing the other.

As the lower bound of the required performance for quarter wave-plate operation, we select $C_{\text{eff}} = 0.9$. By using Eq. 6.68, it can easily be shown that this condition translates to $\eta \geq 32°$. Note that, by definition, the maximum value η can take is 45° and this value is achieved when $C_{\text{eff}} = 1$ and corresponds to purely right-hand circular polarization. LCP wave transmission can be realized by setting the polarization plane of the normally incident linearly polarized plane wave to $-\pi/4$.

We compute the $C_\pm$ and C_{eff} spectra by using RCWA and Eq. 6.64, and they are shown in Fig. 6.5. In addition to the RCWA method, we employ FDTD simulations, where the dispersion of the refractive indices of Si and SiO_2 is taken into account properly by utilizing the refractive index data given in Ref. [113], in order to demonstrate that the resultant effect of material dispersion does not significantly modify the operation band. As shown in Fig. 6.5(b), material dispersion affects the C_{eff} spectrum mainly for $\lambda_0 \lesssim 1.4$ μm, where the refractive index of Si changes significantly with wavelength, see Ref. [113]. According to RCWA, $C_{\text{eff}} \geq 0.9$ is satisfied between 1.36μm and 2.36μm. FDTD results suggest a slightly different wavelength interval: 1.4μm – 2.36μm. In order to characterize the width of the operation band, we define the *percent bandwidth*

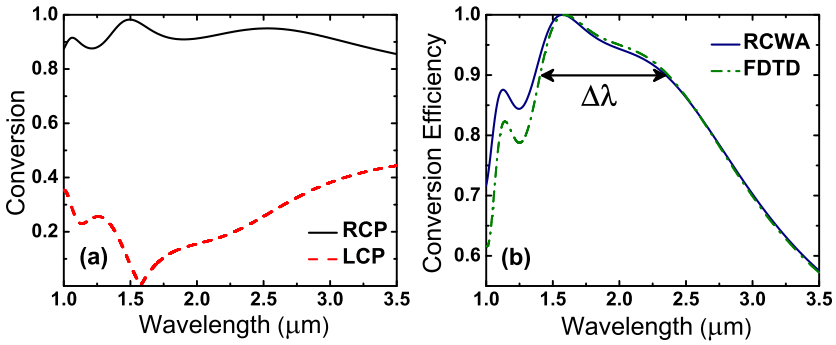

Figure 6.5: (a) $C_{\pm}$ spectra obtained by utilizing RCWA and (b) C_{eff} spectrum obtained by utilizing RCWA and FDTD. In (b), we denote the wavelength range for which $C_{\text{eff}} \geq 0.9$ is satisfied by $\Delta\lambda$. Reprinted with permission from [111]. Copyright 2012 by the Optical Society of America.

parameter as follows:

$$\text{BW}\% = 200\% \frac{\lambda_H/\lambda_L - 1}{\lambda_H/\lambda_L + 1}. \tag{6.69}$$

In Eq. 6.69, λ_H and λ_L denote the higher and lower edges of the operation band, respectively. Accordingly, the RCWA result suggests that BW% = 54% and a similar analysis of the FDTD result yields BW% = 51%. By considering these bandwidth results, we state that, in spite of causing an observable modification in the C_{eff} spectrum, the incorporation of material dispersion does not significantly decrease the percent bandwidth, which is promising in terms of the practical realizability of the proposed structure.

6.3.2 Experimental Design

Secondly, we demonstrate the design, fabrication, and characterization of the experimental HCG based quarter-wave plate design, which is different from the structure analyzed in Sec. 6.3.1 in terms of material choice for region I and the grooves in region II, and geometrical parameters. We base this subsection on Refs. [112, 114]. By modifying the materials occupying regions I, II, and III, we target the achievement of a practically realizable design with a broad operation wavelength range. By considering the potential challenges and device limitations in the nanofabrication stage, we decide to design a HCG structure where region

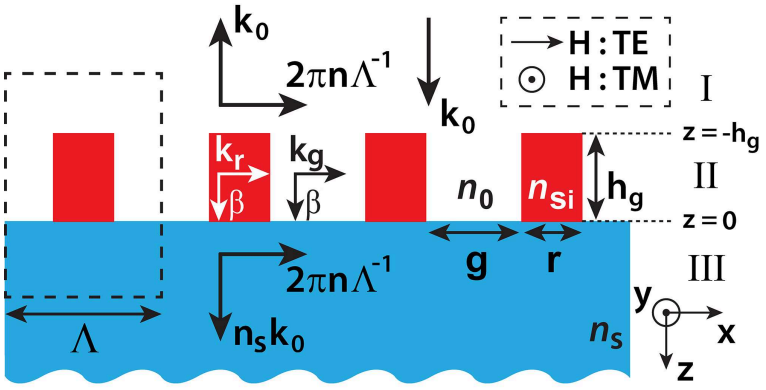

Figure 6.6: Illustration of the proposed experimental design. The dashed black box on the left denotes one period. In this design, region I and the grooves in region II are free-space. In addition, the materials constituting region III and the ridges in region II are given as sapphire and silicon, respectively. Reprinted with permission from [114]. Copyright 2012 by the Optical Society of America.

III and the ridges in region II are composed of sapphire and silicon, respectively. The remaining regions are simply free-space. The proposed geometry for the experimental design is depicted in Fig. 6.6. The polarization state of the incident light is defined as TM and TE when the magnetic field vector is on the y– and x–axis, respectively.

In the analysis of the experimental design, a detailed theoretical solution is not provided since it is mainly the same as what is given in Sec. 6.3.1.1. The fundamental difference of the theoretical analysis of the present design from the one given in the previous section is the utilization of different materials in regions I and III. This discrepancy conduces to different wavenumbers for the reflection and transmission orders, see Eq. 6.2. As a result, different lateral magnetic and electric field profiles are obtained in regions I and III, which can be summarized for TM modes as:

$$H^{\mathrm{I}}_{y,n} \neq H^{\mathrm{III}}_{y,n}, \tag{6.70a}$$

$$E^{\mathrm{I}}_{x,n} \neq E^{\mathrm{III}}_{x,n}, \tag{6.70b}$$

see Eqs. 6.1, 6.3, 6.7, and 6.8. For TE modes, one can simply swap x's and y's in Eq. 6.70. Therefore, the electromagnetic boundary conditions at the two

interfaces, i.e., $z = -h_g$ and $z = 0$, must be satisfied by utilizing the correct lateral distribution.

In optimizing the structure for broadband quarter-wave plate operation, we utilize RCWA based parameter search. Afterwards, we run FDTD simulations in order to incorporate the material dispersion and ensure that it does not significantly modify the bandwidth of operation. In the FDTD simulations, the refractive index data for Si and sapphire are taken from Ref. [113]. The two-dimensional simulations are constructed such that periodic boundary condition is applied along the x–axis, where perfectly matched layer (PML) boundary condition is used for the z–axis. In the simulations, we assume that region III extends to $+\infty$ in the $+z$ direction, meaning that all the layers of PML are terminated inside the sapphire substrate. The reason for this assumption is to avoid the creation of any standing-wave pattern inside the sapphire substrate as a result of the excitation of Fabry-Perot type resonant modes. If a finite-thickness substrate is utilized in the simulations, oscillations in the reflection and transmission spectra are observed as a consequence of the excitation of such modes. As it is going to be evident from the experimental results, the excitation of such modes does not occur when $h_s \gg L_c$, where h_s and L_c denote the thickness of the substrate and the spatial coherence length of the light source, respectively. In the experiments, we utilize a broadband light source, which relies on spontaneous emission, and therefore, the typical coherence length is on the order of several wavelengths for such sources.

By running an RCWA based parametric search algorithm and FDTD simulations, we find that the optimal geometric parameters are given by $r = 220$ nm, $g = 350$ nm, and $h_g = 320$ nm. The resultant periodicity is $\Lambda = 570$ nm and it is equal to $\lambda_0/2.72$ at 1.55μm. Since $\Lambda < \lambda_0/n_s$, only the zeroth reflection and transmission orders are propagating, whereas the higher orders are evanescent waves.

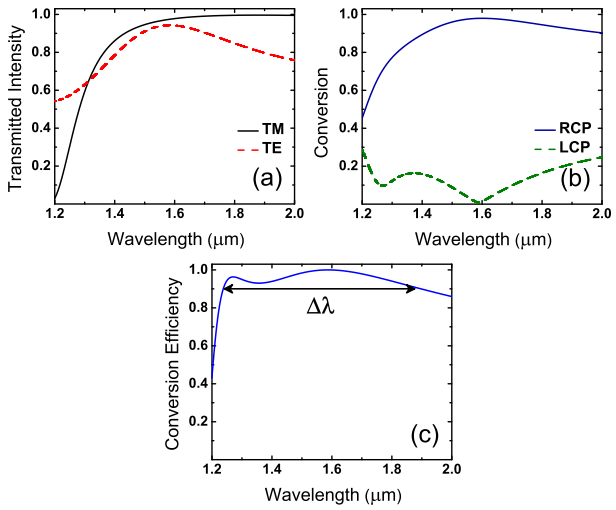

Figure 6.7: Numerical (a) TM and TE transmitted intensities, (b) circular conversion coefficients, and (c) conversion efficiency spectrum obtained via FDTD simulations. The wavelength interval of operation is denoted by $\Delta\lambda$. The numerical conversion efficiency spectrum yields a percent bandwidth of 42%. Reprinted with permission from [114]. Copyright 2012 by the Optical Society of America.

6.3.2.1 Numerical Results

Figure 6.7 shows the normalized transmitted intensity, circular conversion, and conversion efficiency spectra. In obtaining these results, the electric field vector of the incident wave is assumed to make an angle of $\pi/4$ with the x–axis in the first quadrant of the xy–plane. Note that, for the purpose of obtaining an LCP wave in transmission, one can simply rotate the polarization plane of the incident wave by $\pm\pi/2$. As shown in Fig. 6.7(a), one of the quarter-wave plate operation requirements, $|T_{\rm TM}| \simeq |T_{\rm TE}|$, is satisfied in the vicinity of $\lambda_0 = 1.55$ μm. In this section, we do not provide the phase difference between the transmission coefficients, i.e., $\angle(T_{\rm TM}) - \angle(T_{\rm TE})$, explicitly since, as it is going to be evident in the corresponding subsection, phase measurement is not possible in the experimental setups we have prepared for the measurements. Instead, one can use Fig. 6.7(b) and see that $|C_+|^2 \gg |C_-|^2$ is obtained in the vicinity of $\lambda_0 = 1.55$ μm and that implies the satisfaction of the condition in Eq. 6.56(b).

The $C_{\rm eff}$ spectrum that is computed by using Eq. 6.67 is shown in Fig. 6.7. The FDTD results suggest that the operation condition, $C_{\rm eff} \geq 0.9$, is satisfied

between the free-space wavelengths of $\lambda_L = 1.24$ μm and $\lambda_H = 1.40$ μm. This wavelength interval is denoted by $\Delta\lambda$ in Fig. 6.7(c) and the utilization of Eq. 6.69 yields a percent bandwidth of 42%.

6.3.2.2 Fabrication

The proposed HCG structure is fabricated on a silicon-on-sapphire wafer (SOS) with a 100 mm diameter, which is purchased from Valley Design Corporation. The substrate of the SOS wafer is a 0.53 ± 0.05 mm thick R-plane sapphire. The $< 100 >$ silicon layer is grown epitaxially on the substrate and its thickness is specified as 600 ± 60 nm by the company. For an easy handling of the sample, we dice the SOS wafer such that square shaped chips with a dimension of 6 mm by 6 mm are obtained.

The fabrication process starts with the reduction of the thickness of the silicon layer to 320 nm by using a sulfur hexafluoride (SF_6) chemistry based reactive ion etching (RIE) technique. With the aid of a surface profilometer, we verify that the targeted silicon thickness is achieved after the RIE step. Afterwards, poly(methyl methacrylate) (PMMA), which is an electron-beam sensitive positive resist, is deposited on a square SOS chip by means of a conventional spin coating process. Subsequently, the resist is exposed to electron-beam with the utilization of a high-precision e-beam lithography system. This exposing operation modifies the chemistry of the exposed regions of the resist and therefore, with the aid of a developer solution that affects only the exposed regions, the desired pattern can be transferred to the PMMA layer.

Following the e-beam step and the development operation of the PMMA, the final step is accomplished by etching the exposed silicon regions using the RIE system by using SF_6 as the etchant gas. We provide the scanning electron microscope (SEM) micrographs of the successfully fabricated HCG sample in Fig. 6.8. In Fig. 6.8(b), it is seen that the targeted g, r, and Λ parameters are achieved with a precision of a few nanometers.

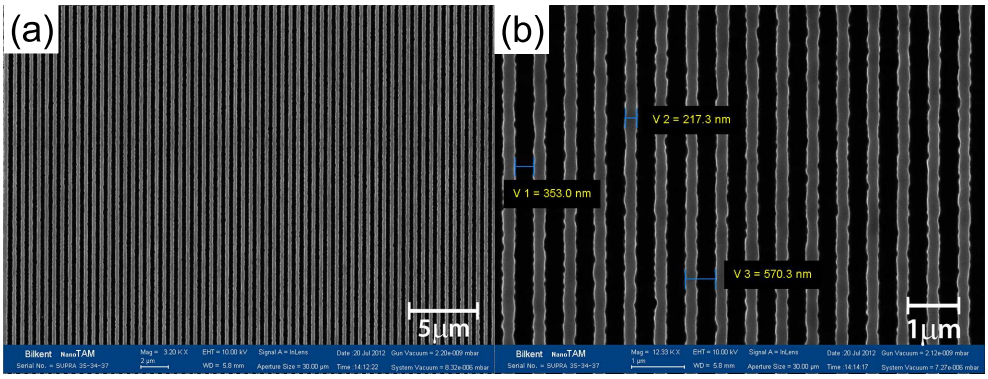

Figure 6.8: (a) Zoomed out and (b) zoomed in top view SEM micrographs of the fabricated HCG structure. In (b), the legends V1, V2, and V3 denote the geometrical parameters g, r, and Λ, respectively. Reprinted with permission from [114]. Copyright 2012 by the Optical Society of America.

6.3.2.3 Experimental Setup

The outlines of the two experimental setups that are constructed for the purpose of measuring $|T_{\mathrm{TM}}|^2$ and $|T_{\mathrm{TE}}|^2$, and $|C_{\pm}|^2$ are shown in Fig. 6.9(a) and 6.9(b) in detail, respectively. In the first experiment setup, we use a broadband near-infrared (NIR) light source (Spectral Products, ASBN-W100-F-L) for illuminating the HCG structure. With the aid of standard commercial objectives, which are specifically designed for the NIR regime, the spot size of the light emerging from the fiber, which is connected to the source, is decreased to 50 μm and the sample is positioned such that it is located at the focus. Afterwards, the light traversing the HCG sample is collimated by another objective and, then, coupled into the fiber that is connected to the NIR spectrometer (Ocean Optics, NIR256-2.5). On the incident wave side, an adjustable linear polarizer (Thorlabs, DGL10) is employed for the purpose of being able to set the polarization of the incident wave to either TM or TE.

In the second experimental setup, we set the transmission axis of the adjustable polarizer on the incident wave side to 45° and add a commercial NIR quarter-wave plate (Thorlabs, WPQ05M-1550), which converts the incident linearly polarized light to the circularly polarized one. The quarter-wave plate is oriented such that its fast axis is along the x–axis and this orientation conduces

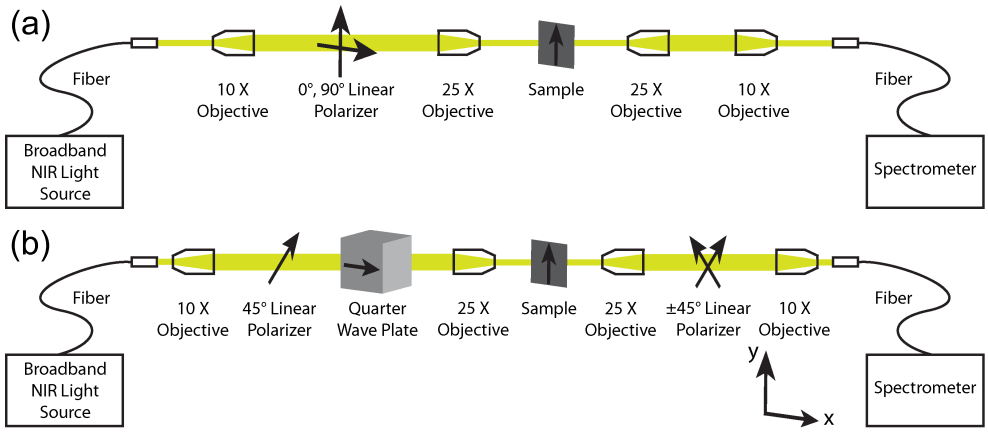

Figure 6.9: Visual illustrations of the experimental setups that are utilized for the measurement of (a) linear transmission coefficients and (b) circular conversion coefficients. The arrows, which lie inside the HCG samples and point upwards, denote the grating direction that is defined in the caption of Fig. 6.6. Reprinted with permission from [114]. Copyright 2012 by the Optical Society of America.

to the transmission of an RCP wave. The transmitted wave is then collimated by an objective and passed through a linear polarizer, the transmission axis of which is set to either $+45°$ or $-45°$. Due to the fact that phase measurement is not possible in these experimental setups, we measure $|C_{\pm}|^2$ with the help of the adjustable polarizer. It can easily be shown that $|C_{-}|^2$ and $|C_{+}|^2$ are measured when the polarizer is adjusted to $+45°$ and $-45°$, respectively. In order to prove this claim, knowing that the system is free from any optically active element, we write the transmission matrix of the HCG as follows:

$$T = \begin{pmatrix} T_{\mathrm{TM}} & 0 \\ 0 & T_{\mathrm{TE}} \end{pmatrix}. \tag{6.71}$$

Note that the cross-polarized transmission coefficients are given by zero in Eq. 6.71 due to the lack of optical activity. Next, the incident wave, which is now an RCP wave, is written in Jones calculus formalism as $2^{-1/2}\begin{pmatrix}1 & -i\end{pmatrix}^T$. The transmitted wave when an RCP wave is incident on the structure can be written as

$$\begin{pmatrix} E_x^t \\ E_y^t \end{pmatrix} = \begin{pmatrix} T_{\mathrm{TM}} & 0 \\ 0 & T_{\mathrm{TE}} \end{pmatrix} \begin{pmatrix} 1/\sqrt{2} \\ -i/\sqrt{2} \end{pmatrix} = \begin{pmatrix} T_{\mathrm{TM}}/\sqrt{2} \\ -iT_{\mathrm{TE}}/\sqrt{2} \end{pmatrix}. \tag{6.72}$$

The next step is to decompose the transmitted wave given in Eq. 6.72 into its

$+45°$ and $-45°$ linearly polarized components. Such a decomposition is always possible since the vectors $2^{-1/2}\,(1 \quad 1)^T$ and $2^{-1/2}\,(1 \quad -1)^T$ are orthogonal to each other and form a basis for the two-dimensional xy–plane. The decomposition operation is performed as

$$\begin{pmatrix} T_{\mathrm{TM}}/\sqrt{2} \\ -iT_{\mathrm{TE}}/\sqrt{2} \end{pmatrix} = C_1 \frac{1}{\sqrt{2}} \begin{pmatrix} 1 \\ 1 \end{pmatrix} + C_2 \frac{1}{\sqrt{2}} \begin{pmatrix} 1 \\ -1 \end{pmatrix}. \tag{6.73}$$

The solution for C_1 and C_2 immediately follows as

$$C_1 = \frac{1}{2}\left(T_{\mathrm{TM}} + iT_{\mathrm{TE}}\right), \tag{6.74a}$$

$$C_2 = \frac{1}{2}\left(T_{\mathrm{TM}} - iT_{\mathrm{TE}}\right). \tag{6.74b}$$

Now, note that C_1 and C_2 are identical to C_- and C_+, respectively, see Eq. 6.64. Since the intensity of the incoming light is measured by the spectrometer, we are able to measure $|C_\pm|^2$ without requiring any phase information.

6.3.2.4 Experimental Results

By using the experimental setups shown in Fig. 6.9, we measure the linear intensity transmission coefficients, $|T_{\mathrm{TM}}|^2$ and $|T_{\mathrm{TE}}|^2$, and circular conversion coefficients, $|C_\pm|^2$, and show these results in Figs. 6.10(a) and 6.10(b), respectively. The resultant conversion efficiency spectrum, which is given in Fig. 6.10(c), is calculated using Eq. 6.67. By analyzing the C_{eff} spectrum, we see that the condition $C_{\mathrm{eff}} \geq 0.9$ is satisfied between $\lambda_L = 1.25$ μm and $\lambda_H = 1.75$ μm. This operation interval corresponds to a percent bandwidth of 33%, see Eq. 6.69.

In our opinion, the major factors that are responsible from the discrepancies between the numerical and experimental results are finite-size and finite substrate thickness related effects. In the numerical analysis, we assumed the simulation to be two-dimensional and the boundary condition along the x–axis to be periodic. These assumptions only approximate the actual structure, which consists of finite number of periods and silicon strips of finite lengths. Such a discrepancy can

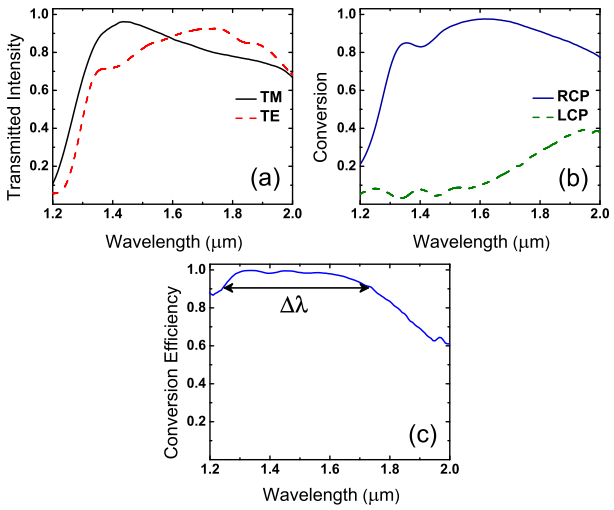

Figure 6.10: Experimentally obtained (a) TM and TE transmitted intensities, (b) circular conversion coefficients, and (c) conversion efficiency spectrum. The wavelength interval of operation is denoted by $\Delta\lambda$. The experimental conversion efficiency spectrum yields a percent bandwidth of 33%. Reprinted with permission from [114]. Copyright 2012 by the Optical Society of America.

possibly modify the lateral and longitudinal wavenumbers of the waveguide modes inside region II, and, in addition, lead to diffraction from the sharp edges of the sample. Furthermore, the utilization of a substrate with a finite thickness can result in multiple back-reflections inside the substrate, modifying the overall behavior of the corrugated surface. Furthermore, Fresnel reflection from the back-side of the substrate can also modify the transmission characteristics of the sample.

In addition to the aforementioned effects, the trapezoidal grating profile achieved after the final etch step and possible deviations of the geometric parameters of the fabricated sample from the design parameters can conduce to the discrepancies between the numerical and experimental results. Furthermore, less significant effects such as the employment of non-ideal optical elements, i.e., linear polarizer and quarter-wave plate, probable small deviation of the actual refractive indices from the ones adopted in the simulations, and human related errors while setting the polarizer transmission axis angle and the angle of incidence might as well contribute to the deviations in the experimental results from the numerical ones.

In principle, back-reflection effects can be subtracted from the measurement results numerically. First of all, as a result of the temporal coherence length, L_c, of the utilized light source being much shorter than the thickness of the substrate ($L_c \ll t_s$), it is safe to assume that the interference effects (arising due to the presence of waves travelling in opposite directions inside the substrate) vanish statistically. At this point, one can disregard the phase information of the travelling waves and use a ray tracing approach in order to write the total reflectance of a finite thickness structure, considering incoherent multireflections, as follows:

$$R_{\text{total}} = R_1 + (1 - R_1)^2 R_2 D^2 \left[\sum_{n=0}^{\infty} \left(R_1 R_2 D^2 \right)^n \right], \tag{6.75}$$

where R_1 and R_2 are the reflection coefficients of the upper (HCG region) and bottom (back of the substrate) interfaces, respectively. In Eq. 6.75, D denotes the spectral absorption that is given by $D = \exp(-0.5\alpha t_s)$, where α is the extinction coefficient of the corresponding medium. The infinite summation in Eq. 6.75 converges to a finite number and the equation can simply be written as:

$$R_{\text{total}} = R_1 + \frac{(1 - R_1)^2 R_2 D^2}{1 - R_1 R_2 D^2}. \tag{6.76}$$

For the purpose of determining R_1, the spectral absorption, D, should be obtained experimentally. In fact, the obtaining of D from the reflection data of an unpatterned substrate is simple. In the bare sapphire substrate case, $R_1 = R_2$ and Eq. 6.76 can be solved for D^2 as follows:

$$D^2 = \frac{R_{\text{total}} - R_2}{(1 - R_2)^2 R_2 + R_2^2 R_{\text{total}} - R_2^3}. \tag{6.77}$$

As it is evident from Eq. 6.77, for the enabling of the obtaining of a sensible D spectrum, meaning that all D values must be real and positive, the total reflectance, R_{total}, for the bare sapphire substrate must always be larger than the reflection from a single interface, R_2. Finally, by modifying Eq. 6.76, we express R_1 in terms of R_{total}, R_2, and D^2 as follows:

$$R_1 = \frac{R_{\text{total}} - R_2 D^2}{1 + R_2 R_{\text{total}} D^2 - 2 R_2 D^2}. \tag{6.78}$$

R_2 can be theoretically calculated by using the Fresnel equations [16] and, for normal incidence, is given as:

$$R_2 = \frac{n_s - n_0}{n_s + n_0}, \tag{6.79}$$

where n_s and n_0 are the refractive indices of sapphire and free-space, respectively.

In summary, the effects of backside- and multi-reflections can be subtracted from the experimental data in five steps: (i) calculation of R_2 using Eq. 6.79, (ii) measurement of R_{total} from a bare sapphire substrate, (iii) usage of Eq. 6.77 to determine D, (iv) measurement of R_{total} from the patterned surface, and (v) usage of Eq. 6.78 to calculate the desired reflection coefficient, R_1.

Recall that, in our case, $n_s = 1.74$ and therefore, we obtain $R_2 = 0.27$ ($R_2^2 = 0.073$). Moreover, it is safe to assume that $\text{Im}\{n_s\} = 0$ in the vicinity of $\lambda_0 = 1.55$ μm, which implies $D = 1$. By noting that R_2^2 is sufficiently smaller than unity and therefore, can be ignored, we do not employ this numerical method to subtract the back- and multi-reflection effects from our experimental data. The result of not applying this method is a small reduction in the overall transmittance of the HCG sample, compare Figs. 6.7(a) and 6.10(a). Since we are more interested in the linear-to-circular conversion efficiency, we believe that this transmission reduction is not crucially important for the verification of the numerical predictions.

Chapter 7

Conclusions

The illustration of the research work related to the high-contrast gratings finalized the technical content of this thesis. Briefly, we have exploited the interesting properties offered by metamaterials and high-contrast gratings, which are artificial structures, to design polarization sensitive devices operating at both microwave and optical frequencies.

In Chapter 2, we first gave a brief overview of circular transmission coefficients, and degree of optical activity and circular dichroism. Then, in Sec. 2.4, we have designed an asymmetric chiral metamaterial structure based on four double-layered U-shaped split ring resonators. Left- and right-hand circularly polarized waves are obtained in the vicinity of 5.1 GHz and 6.4 GHz, respectively, when the structure is illuminated by an x-polarized wave propagating in the $-z$ direction. The design can be utilized as a circular polarizer for microwave applications. In addition, in Sec. 2.5, we combined the giant optical activity effect arising due to chirality with the electromagnetic wave tunneling phenomenon to design an ultrathin, polarization independent, and transparent 90° polarization rotator. Using this tunneling assisted chirality mechanism, cross-polarization conversion was performed with almost 100% efficiency. Such devices can be employed in antenna applications, laser applications, remote sensors, and liquid crystal displays. Plus, the suggested approaches and ideas for the proposed designs may be adapted for the terahertz and optical applications.

In Chapter 3, we showed that the obtaining of truly bound states is possible at a corrugated perfect electric conductor and air (hence, dielectric) interface. Then, we briefly discussed the extraordinary transmission and directional beaming phenomena. Afterwards, in Sec. 3.4, we demonstrated a new approach to enable the unidirectional excitation of spoof surface plasmons and the relevant asymmetric extraordinary transmission and beaming. It can be realized in a composite structure that combines a symmetric metallic grating with a single subwavelength slit and a 90° polarization rotator. This is a good example of that how the integration of structures with substantially different properties allows one obtaining new functionalities beyond those associated with each of the individual structures. From the point of view of the metallic grating with a subwavelength slit, the used stacking of the two structures allows the one-way excitation of spoof surface plasmons and the relevant diodelike transmission effect without utilizing anisotropic or nonlinear materials and, furthermore, at normal incidence. For the composite structure, extraordinary transmission can be obtained for s-polarized incident waves that would be impossible while using the grating alone. From the point of view of the metamaterial based 90° polarization rotator, the diode-like beaming regime would be impossible without stacking with a metallic grating having a subwavelength slit. Reversibility, i.e., ability of the suggested structure to work like a diode in the beaming regime at either s- or p-polarization, depending on whether the forward or the backward case is considered, is very important. It is noteworthy that it either cannot or is difficult to be realized using most of the other known approaches. Clearly, neither reversibility nor diode-like asymmetric transmission would be possible if the spatial inversion symmetry of the composite structure is not broken properly, e.g., if sandwiching the metallic grating between two identical 90° polarization rotators. This mechanism is also expected to be realizable in similar composite structures with a total thickness less than $\lambda/4$. Despite that the performance we used in order to demonstrate the suggested mechanism has been designed for microwave frequencies, the main ideas and the results of this paper can be utilized as guidelines for future terahertz and optical frequency designs.

In Chapter 4, we first discussed the reciprocity conditions in a bianisotropic

medium. Next, the asymmetric transmission phenomenon and the calculation of the degree of asymmetry in transmission was explained. Then, in Sec. 4.4, we designed an electrically thin chiral metamaterial structure that allows obtaining polarization rotation, which is dependent on the polarization angle of the incident linearly polarized plane wave at 6.2 GHz. We derived a closed form expression, which relate the degree of polarization rotation to the polarization angle of the incident wave. In addition, it has been demonstrated that the transmission matrix depends on the propagation direction of the incoming wave. Thus, the transmission through the structure is asymmetric for linearly polarized waves. On the other hand, four angles have been found for which the transmission is symmetric. Finally, surface current distributions at 6.2 GHz are studied in order to explain the underlying mechanism behind the asymmetric transmission. The proposed chiral metamaterial can be utilized in microwave applications as a configurable polarization rotator. Furthermore, In Sec. 4.5, we demonstrated a diodelike asymmetric transmission for normally incident x- and y-polarized waves in an electrically thin reciprocal structure. In addition to the planar ultrathin design, the usage of isotropic and linear materials only makes this and similar structures the promising candidates for practical applications. The backward-to-forward transmission contrast of the structure at the operating frequency 7 GHz is 19.5 and 13 dB according to the simulation and experiment results, respectively. The asymmetry factor at this frequency is 0.95 for the simulation results and 0.91 for the experiments. The ideas of the suggested approaches are promising for future designs at the terahertz and optical frequency ranges.

In Chapter 5, we discussed the guiding mechanisms in parallel-plate metallic waveguides, dielectric slab waveguides, and, more importantly, periodic dielectric slab waveguides. The theoretical background presented in this chapter was crucial for understanding the theoretical description of high-contrast gratings. We used the resultant dispersion relations of periodic dielectric waveguides when developing the theory of high-contrast gratings.

In Chapter 6, we showed the theory of high-contrast gratings for transverse electric and magnetic waves. Afterwards, in Sec. 6.3.1, we designed an optimized two-dimensional HCG such that the transmitted wave is circularly polarized if the

structure is illuminated by a plane wave with a polarization plane angle of $\pi/4$. It has numerically been shown that a conversion efficiency that is larger than 0.9 can be achieved within a 51% bandwidth. Finally, in Sec. 6.3.2, we showed the fabrication and the experimental characterization of a broadband quarter-wave plate that is based on two-dimensional silicon HCGs, where sapphire is employed as the substrate. It was shown that a conversion efficiency that is higher than 0.9 can be achieved in a percent bandwidth of 42% and 33% numerically and experimentally, respectively. RCP and LCP waves can be obtained by adjusting the transmission axis of the linear polarizer to 45° and -45° with respect to the x-axis, respectively. Some possible application areas of these proposed structures can be listed as nanoantenna and laser applications, remote sensors, and liquid crystal displays.

Bibliography

[1] E. Plum, V. A. Fedotov, A. S. Schwanecke, N. I. Zheludev, and Y. Chen, "Giant optical gyrotropy due to electromagnetic coupling," *Applied Physics Letters*, vol. 90, no. 22, p. 223113, 2007.

[2] M. Decker, M. W. Klein, M. Wegener, and S. Linden, "Circular dichroism of planar chiral magnetic metamaterials," *Opt. Lett.*, vol. 32, no. 7, pp. 856–858, 2007.

[3] J. B. Pendry, "A chiral route to negative refraction," *Science*, vol. 306, no. 5700, pp. 1353–1355, 2004.

[4] Z. Li, R. Zhao, T. Koschny, M. Kafesaki, K. B. Alici, E. Colak, H. Caglayan, E. Ozbay, and C. M. Soukoulis, "Chiral metamaterials with negative refractive index based on four "u" split ring resonators," *Applied Physics Letters*, vol. 97, no. 8, p. 081901, 2010.

[5] H. Liu, D. A. Genov, D. M. Wu, Y. M. Liu, Z. W. Liu, C. Sun, S. N. Zhu, and X. Zhang, "Magnetic plasmon hybridization and optical activity at optical frequencies in metallic nanostructures," *Phys. Rev. B*, vol. 76, p. 073101, 2007.

[6] T. Q. Li, H. Liu, T. Li, S. M. Wang, F. M. Wang, R. X. Wu, P. Chen, S. N. Zhu, and X. Zhang, "Magnetic resonance hybridization and optical activity of microwaves in a chiral metamaterial," *Applied Physics Letters*, vol. 92, no. 13, p. 131111, 2008.

[7] H. Liu, J. X. Cao, S. N. Zhu, N. Liu, R. Ameling, and H. Giessen, "Lagrange model for the chiral optical properties of stereometamaterials," *Phys. Rev. B*, vol. 81, p. 241403, 2010.

[8] N. Liu, H. Liu, S. Zhu, and H. Giessen, "Stereometamaterials," *Nat. Photon.*, vol. 3, pp. 157–162, 2009.

[9] A. V. Rogacheva, V. A. Fedotov, A. S. Schwanecke, and N. I. Zheludev, "Giant gyrotropy due to electromagnetic-field coupling in a bilayered chiral structure," *Phys. Rev. Lett.*, vol. 97, p. 177401, 2006.

[10] Y. Ye and S. He, "90° polarization rotator using a bilayered chiral metamaterial with giant optical activity," *Applied Physics Letters*, vol. 96, no. 20, p. 203501, 2010.

[11] B. Bai, Y. Svirko, J. Turunen, and T. Vallius, "Optical activity in planar chiral metamaterials: Theoretical study," *Phys. Rev. A*, vol. 76, p. 023811, 2007.

[12] D.-H. Kwon, P. L. Werner, and D. H. Werner, "Optical planar chiral metamaterial designs for strong circular dichroism and polarization rotation," *Opt. Express*, vol. 16, no. 16, pp. 11802–11807, 2008.

[13] J. Dong, J. Zhou, T. Koschny, and C. Soukoulis, "Bi-layer cross chiral structure with strong optical activity and negative refractive index," *Opt. Express*, vol. 17, no. 16, pp. 14172–14179, 2009.

[14] R. Zhao, T. Koschny, and C. M. Soukoulis, "Chiral metamaterials: retrieval of the effective parameters with and without substrate," *Opt. Express*, vol. 18, no. 14, pp. 14553–14567, 2010.

[15] C. Menzel, C. Rockstuhl, and F. Lederer, "Advanced jones calculus for the classification of periodic metamaterials," *Phys. Rev. A*, vol. 82, p. 053811, 2010.

[16] B. E. A. Saleh and M. C. Teich, *Fundamentals of Photonics*. John Wiley & Sons, 2007.

[17] M. Mutlu, A. E. Akosman, A. E. Serebryannikov, and E. Ozbay, "Asymmetric chiral metamaterial circular polarizer based on four U-shaped split ring resonators," *Opt. Lett.*, vol. 36, no. 9, pp. 1653–1655, 2011.

[18] Nasimuddin, X. Qing, and Z. N. Chen, "Compact asymmetric-slit microstrip antennas for circular polarization," *IEEE Trans. Antenna Propagat.*, vol. 59, pp. 285–288, 2011.

[19] K. L. Wong, C. C. Huang, and W. S. Chen, "Printed ring slot antenna for circular polarization," *IEEE Trans. Antenna Propagat.*, vol. 50, pp. 75–77, 2002.

[20] J. Y. Sze, K. L. Wong, and C. C. Huang, "Coplanar waveguide-fed square slot antenna for broadband circularly polarized radiation," *IEEE Trans. Antenna Propagat.*, vol. 51, pp. 2141–2144, 2003.

[21] T. V. Liseikina and A. Macchi, "Features of ion acceleration by circularly polarized laser pulses," *Applied Physics Letters*, vol. 91, no. 17, p. 171502, 2007.

[22] A. H. Nejadmalayeri and P. R. Herman, "Ultrafast laser waveguide writing: lithium niobate and the role of circular polarization and picosecond pulse width," *Opt. Lett.*, vol. 31, no. 20, pp. 2987–2989, 2006.

[23] Z. Ge, M. Jiao, R. Lu, T. X. Wu, S.-T. Wu, W.-Y. Li, and C.-K. Wei, "Wide-view and broadband circular polarizers for transflective liquid crystal displays," *J. Display Technol.*, vol. 4, no. 2, pp. 129–138, 2008.

[24] Q. Hong, T. Wu, X. Zhu, R. Lu, and S.-T. Wu, "Designs of wide-view and broadband circular polarizers," *Opt. Express*, vol. 13, no. 20, pp. 8318–8331, 2005.

[25] X. Xiong, W.-H. Sun, Y.-J. Bao, M. Wang, R.-W. Peng, C. Sun, X. Lu, J. Shao, Z.-F. Li, and N.-B. Ming, "Construction of a chiral metamaterial with a u-shaped resonator assembly," *Phys. Rev. B*, vol. 81, p. 075119, 2010.

[26] M. Mutlu and E. Ozbay, "A transparent 90° polarization rotator by combining chirality and electromagnetic wave tunneling," *Applied Physics Letters*, vol. 100, no. 5, p. 051909, 2012.

[27] J. Hao, Y. Yuan, L. Ran, T. Jiang, J. A. Kong, C. T. Chan, and L. Zhou, "Manipulating electromagnetic wave polarizations by anisotropic metamaterials," *Phys. Rev. Lett.*, vol. 99, p. 063908, 2007.

[28] J. Y. Chin, M. Lu, and T. J. Cui, "Metamaterial polarizers by electric-field-coupled resonators," *Applied Physics Letters*, vol. 93, no. 25, p. 251903, 2008.

[29] W. Sun, Q. He, J. Hao, and L. Zhou, "A transparent metamaterial to manipulate electromagnetic wave polarizations," *Opt. Lett.*, vol. 36, no. 6, pp. 927–929, 2011.

[30] M. Liu, Y. Zhang, X. Wang, and C. Jin, "Incident-angle-insensitive and polarization independent polarization rotator," *Opt. Express*, vol. 18, no. 11, pp. 11990–12001, 2010.

[31] R. Zhao, L. Zhang, J. Zhou, T. Koschny, and C. M. Soukoulis, "Conjugated gammadion chiral metamaterial with uniaxial optical activity and negative refractive index," *Phys. Rev. B*, vol. 83, p. 035105, 2011.

[32] L. Zhou, W. Wen, C. T. Chan, and P. Sheng, "Electromagnetic-wave tunneling through negative-permittivity media with high magnetic fields," *Phys. Rev. Lett.*, vol. 94, p. 243905, 2005.

[33] B. Hou, H. Wen, Y. Leng, and W. Wen, "Electromagnetic wave transmission through subwavelength metallic meshes sandwiched between split rings," *Applied Physics Letters*, vol. 87, no. 20, p. 201114, 2005.

[34] G. Castaldi, I. Gallina, V. Galdi, A. Alù, and N. Engheta, "Electromagnetic tunneling through a single-negative slab paired with a double-positive bilayer," *Phys. Rev. B*, vol. 83, p. 081105, 2011.

[35] G. Castaldi, V. Galdi, A. Alù, and N. Engheta, "Electromagnetic tunneling of obliquely incident waves through a single-negative slab paired with a

double-positive uniaxial slab," *J. Opt. Soc. Am. B*, vol. 28, no. 10, pp. 2362–2368, 2011.

[36] M. Born and E. Wolf, *Principles of Optics: Electromagnetic Theory of Propagation, Interference and Diffraction of Light*. Cambridge University Press, 1999.

[37] C. A. Balanis, *Advanced Engineering Electromagnetics*. John Wiley & Sons, 1989.

[38] T. W. Ebbesen, H. J. Lezec, H. F. Ghaemi, T. Thio, and P. A. Wolff, "Extraordinary optical transmission through sub-wavelength hole arrays," *Nature*, vol. 391, pp. 667–669, 1998.

[39] M. Mutlu, S. Cakmakyapan, A. E. Serebryannikov, and E. Ozbay, "One-way reciprocal spoof surface plasmons and relevant reversible diodelike beaming," *Phys. Rev. B*, vol. 87, p. 205123, 2013.

[40] J. B. Pendry, L. Martn-Moreno, and F. J. Garcia-Vidal, "Mimicking surface plasmons with structured surfaces," *Science*, vol. 305, no. 5685, pp. 847–848, 2004.

[41] A. P. Hibbins, B. R. Evans, and J. R. Sambles, "Experimental verification of designer surface plasmons," *Science*, vol. 308, no. 5722, pp. 670–672, 2005.

[42] H. Raether, *Surface Plasmons on Smooth and Rough Surfaces and on Gratings*. Springer, Berlin, 1988.

[43] T. Thio, K. M. Pellerin, R. A. Linke, H. J. Lezec, and T. W. Ebbesen, "Enhanced light transmission through a single subwavelength aperture," *Opt. Lett.*, vol. 26, no. 24, pp. 1972–1974, 2001.

[44] H. J. Lezec, A. Degiron, E. Devaux, R. A. Linke, L. Martin-Moreno, F. J. Garcia-Vidal, and T. W. Ebbesen, "Beaming light from a subwavelength aperture," *Science*, vol. 297, no. 5582, pp. 820–822, 2002.

[45] H. Caglayan, I. Bulu, and E. Ozbay, "Extraordinary grating-coupled microwave transmission through a subwavelength annular aperture," *Opt. Express*, vol. 13, no. 5, pp. 1666–1671, 2005.

[46] A. Degiron and T. Ebbesen, "Analysis of the transmission process through single apertures surrounded by periodic corrugations," *Opt. Express*, vol. 12, no. 16, pp. 3694–3700, 2004.

[47] E. Ozbay, "Plasmonics: Merging photonics and electronics at nanoscale dimensions," *Science*, vol. 311, no. 5758, pp. 189–193, 2006.

[48] S. Kim, H. Kim, Y. Lim, and B. Lee, "Off-axis directional beaming of optical field diffracted by a single subwavelength metal slit with asymmetric dielectric surface gratings," *Applied Physics Letters*, vol. 90, no. 5, p. 051113, 2007.

[49] N. Bonod, E. Popov, L. Li, and B. Chernov, "Unidirectional excitation of surface plasmons by slanted gratings," *Opt. Express*, vol. 15, no. 18, pp. 11427–11432, 2007.

[50] I. P. Radko, S. I. Bozhevolnyi, G. Brucoli, L. Martin-Moreno, F. J. Garcia-Vidal, and A. Boltasseva, "Efficient unidirectional ridge excitationof surface plasmons," *Opt. Express*, vol. 17, no. 9, pp. 7228–7232, 2009.

[51] A. Roszkiewicz and W. Nasalski, "Unidirectional spp excitation at asymmetrical two-layered metal gratings," *Journal of Physics B: Atomic, Molecular and Optical Physics*, vol. 43, no. 18, p. 185401, 2010.

[52] S. B. Choi, D. J. Park, Y. K. Jeong, Y. C. Yun, M. S. Jeong, C. C. Byeon, J. H. Kang, Q.-H. Park, and D. S. Kim, "Directional control of surface plasmon polariton waves propagating through an asymmetric bragg resonator," *Applied Physics Letters*, vol. 94, no. 6, p. 063115, 2009.

[53] F. Lopez-Tejeira, S. G. Rodrigo, L. Martin-Moreno, F. J. Garcia-Vidal, E. Devaux, T. W. Ebbesen, J. R. Krenn, I. P. Radko, S. I. Bozhevolnyi, M. U. Gonzalez, J. C. Weeber, and A. Dereux, "Efficient unidirectional nanoslit couplers for surface plasmons," *Nat. Phys.*, vol. 3, pp. 324–328, 2007.

[54] S. Cakmakyapan, A. E. Serebryannikov, H. Caglayan, and E. Ozbay, "One-way transmission through the subwavelength slit in nonsymmetric metallic gratings," *Opt. Lett.*, vol. 35, no. 15, pp. 2597–2599, 2010.

[55] S. Cakmakyapan, H. Caglayan, A. E. Serebryannikov, and E. Ozbay, "Experimental validation of strong directional selectivity in nonsymmetric metallic gratings with a subwavelength slit," *Applied Physics Letters*, vol. 98, no. 5, p. 051103, 2011.

[56] A. B. Khanikaev, S. H. Mousavi, G. Shvets, and Y. S. Kivshar, "One-way extraordinary optical transmission and nonreciprocal spoof plasmons," *Phys. Rev. Lett.*, vol. 105, p. 126804, 2010.

[57] A. E. Serebryannikov, "One-way diffraction effects in photonic crystal gratings made of isotropic materials," *Phys. Rev. B*, vol. 80, p. 155117, 2009.

[58] A. E. Serebryannikov, A. O. Cakmak, and E. Ozbay, "Multichannel optical diode with unidirectional diffraction relevant total transmission," *Opt. Express*, vol. 20, no. 14, pp. 14980–14990, 2012.

[59] A. O. Cakmak, E. Colak, A. E. Serebryannikov, and E. Ozbay, "Unidirectional transmission in photonic-crystal gratings at beam-type illumination," *Opt. Express*, vol. 18, no. 21, pp. 22283–22298, 2010.

[60] X.-F. Li, X. Ni, L. Feng, M.-H. Lu, C. He, and Y.-F. Chen, "Tunable unidirectional sound propagation through a sonic-crystal-based acoustic diode," *Phys. Rev. Lett.*, vol. 106, p. 084301, 2011.

[61] A. E. Serebryannikov and E. Ozbay, "Unidirectional transmission in nonsymmetric gratings containing metallic layers," *Opt. Express*, vol. 17, no. 16, pp. 13335–13345, 2009.

[62] R. Singh, E. Plum, C. Menzel, C. Rockstuhl, A. K. Azad, R. A. Cheville, F. Lederer, W. Zhang, and N. I. Zheludev, "Terahertz metamaterial with asymmetric transmission," *Phys. Rev. B*, vol. 80, p. 153104, 2009.

[63] V. A. Fedotov, P. L. Mladyonov, S. L. Prosvirnin, A. V. Rogacheva, Y. Chen, and N. I. Zheludev, "Asymmetric propagation of electromagnetic waves through a planar chiral structure," *Phys. Rev. Lett.*, vol. 97, p. 167401, 2006.

[64] V. A. Fedotov, A. S. Schwanecke, N. I. Zheludev, V. V. Khardikov, and S. L. Prosvirnin, "Asymmetric transmission of light and enantiomerically sensitive plasmon resonance in planar chiral nanostructures," *Nano Letters*, vol. 7, no. 7, pp. 1996–1999, 2007.

[65] C. Menzel, C. Helgert, C. Rockstuhl, E.-B. Kley, A. Tünnermann, T. Pertsch, and F. Lederer, "Asymmetric transmission of linearly polarized light at optical metamaterials," *Phys. Rev. Lett.*, vol. 104, p. 253902, 2010.

[66] M. Mutlu, A. E. Akosman, A. E. Serebryannikov, and E. Ozbay, "Diodelike asymmetric transmission of linearly polarized waves using magnetoelectric coupling and electromagnetic wave tunneling," *Phys. Rev. Lett.*, vol. 108, p. 213905, 2012.

[67] F. J. Garcia-Vidal, L. Martín-Moreno, and J. B. Pendry, "Surfaces with holes in them: new plasmonic metamaterials," *Journal of Optics A: Pure and Applied Optics*, vol. 7, no. 2, p. S97, 2005.

[68] S. A. Maier, *Plasmonics: Fundamentals and Applications*. Springer, 2007.

[69] H. A. Bethe, "Theory of diffraction by small holes," *Phys. Rev.*, vol. 66, pp. 163–182, 1944.

[70] P. Banzer, J. Kindler, S. Quabis, U. Peschel, and G. Leuchs, "Extraordinary transmission through a single coaxial aperture in a thin metalfilm," *Opt. Express*, vol. 18, no. 10, pp. 10896–10904, 2010.

[71] S. M. Orbons and A. Roberts, "Resonance and extraordinary transmission in annular aperture arrays," *Opt. Express*, vol. 14, no. 26, pp. 12623–12628, 2006.

[72] H. F. Ghaemi, T. Thio, D. E. Grupp, T. W. Ebbesen, and H. J. Lezec, "Surface plasmons enhance optical transmission through subwavelength holes," *Phys. Rev. B*, vol. 58, pp. 6779–6782, 1998.

[73] L. Martín-Moreno, F. J. García-Vidal, H. J. Lezec, A. Degiron, and T. W. Ebbesen, "Theory of highly directional emission from a single subwavelength aperture surrounded by surface corrugations," *Phys. Rev. Lett.*, vol. 90, p. 167401, 2003.

[74] A. Figotin and I. Vitebsky, "Nonreciprocal magnetic photonic crystals," *Phys. Rev. E*, vol. 63, p. 066609, 2001.

[75] Z. Yu, Z. Wang, and S. Fan, "One-way total reflection with one-dimensional magneto-optical photonic crystals," *Applied Physics Letters*, vol. 90, no. 12, p. 121133, 2007.

[76] C. E. Ruter, K. G. Makris, R. El-Ganainy, D. N. Christodoulides, M. Segev, and D. Kip, "Observation of parity-time symmetry in optics," *Nat. Phys.*, vol. 6, no. 3, pp. 192–195, 2010.

[77] E. Plum, V. A. Fedotov, and N. I. Zheludev, "Planar metamaterial with transmission and reflection that depend on the direction of incidence," *Applied Physics Letters*, vol. 94, no. 13, p. 131901, 2009.

[78] D. K. Cheng and J.-A. Kong, "Covariant descriptions of bianisotropic media," *Proceedings of the IEEE*, vol. 56, no. 3, pp. 248–251, 1968.

[79] J.-A. Kong and D. K. Cheng, "Modified reciprocity theorem for bianisotropic media," *Electrical Engineers, Proceedings of the Institution of*, vol. 117, no. 2, pp. 349–350, 1970.

[80] M. Mutlu, A. E. Akosman, A. E. Serebryannikov, and E. Ozbay, "Asymmetric transmission of linearly polarized waves and polarization angle dependent wave rotation using a chiral metamaterial," *Opt. Express*, vol. 19, no. 15, pp. 14290–14299, 2011.

[81] T. Li, H. Liu, S.-M. Wang, X.-G. Yin, F.-M. Wang, S.-N. Zhu, and X. Zhang, "Manipulating optical rotation in extraordinary transmission

by hybrid plasmonic excitations," *Applied Physics Letters*, vol. 93, no. 2, p. 021110, 2008.

[82] D. M. H. Leung, B. Rahman, and K. T. V. Grattan, "Numerical analysis of asymmetric silicon nanowire waveguide as compact polarization rotator," *Photonics Journal, IEEE*, vol. 3, no. 3, pp. 381–389, 2011.

[83] Z. Li, H. Caglayan, E. Colak, J. Zhou, C. M. Soukoulis, and E. Ozbay, "Coupling effect between two adjacent chiral structure layers," *Opt. Express*, vol. 18, no. 6, pp. 5375–5383, 2010.

[84] R. Zhao, T. Koschny, E. N. Economou, and C. M. Soukoulis, "Comparison of chiral metamaterial designs for repulsive casimir force," *Phys. Rev. B*, vol. 81, p. 235126, 2010.

[85] X. Hu, C. Xin, Z. Li, and Q. Gong, "Ultrahigh-contrast all-optical diodes based on tunable surface plasmon polaritons," *New Journal of Physics*, vol. 12, no. 2, p. 023029, 2010.

[86] S. I. Maslovski, D. K. Morits, and S. A. Tretyakov, "Symmetry and reciprocity constraints on diffraction by gratings of quasi-planar particles," *Journal of Optics A: Pure and Applied Optics*, vol. 11, no. 7, p. 074004, 2009.

[87] R. S. Elliott, *An Introduction to Guided Waves and Microwave Circuits*. Prentice-Hall, 1993.

[88] J. D. Jackson, *Classical Electrodynamics*. John Wiley & Sons, 1975.

[89] V. Karagodsky and C. J. Chang-Hasnain, "Physics of near-wavelength high contrast gratings," *Opt. Express*, vol. 20, no. 10, pp. 10888–10895, 2012.

[90] C. Mateus, M. Huang, Y. Deng, A. Neureuther, and C. Chang-Hasnain, "Ultrabroadband mirror using low-index cladded subwavelength grating," *IEEE Photonic Tech. Lett.*, vol. 16, no. 2, pp. 518 –520, 2004.

[91] C. Mateus, M. Huang, L. Chen, C. Chang-Hasnain, and Y. Suzuki, "Broadband mirror (1.12-1.62 μm) using a subwavelength grating," *IEEE Photonic Tech. Lett.*, vol. 16, no. 7, pp. 1676 –1678, 2004.

[92] Y. Zhou, M. Huang, and C. Chang-Hasnain, "Large fabrication tolerance for VCSELs using high-contrast grating," *IEEE Photonic Tech. Lett.*, vol. 20, no. 6, pp. 434 –436, 2008.

[93] V. Karagodsky, F. G. Sedgwick, and C. J. Chang-Hasnain, "Theoretical analysis of subwavelength high contrast grating reflectors," *Opt. Express*, vol. 18, no. 16, pp. 16973–16988, 2010.

[94] C. J. Chang-Hasnain and W. Yang, "High-contrast gratings for integrated optoelectronics," *Adv. Opt. Photon.*, vol. 4, no. 3, pp. 379–440, 2012.

[95] H. Wu, W. Mo, J. Hou, D. Gao, R. Hao, H. Jiang, R. Guo, W. Wu, and Z. Zhou, "A high performance polarization independent reflector based on a multilayered configuration grating structure," *J. Opt.*, vol. 12, no. 4, p. 045703, 2010.

[96] H. Wu, W. Mo, J. Hou, D. Gao, R. Hao, R. Guo, W. Wu, and Z. Zhou, "Polarizing beam splitter based on a subwavelength asymmetric profile grating," *J. Opt.*, vol. 12, no. 1, p. 015703, 2010.

[97] W. Yang, F. Sedgwick, Z. Zhang, and C. J. Chang-Hasnain, "High contrast grating based saturable absorber for mode-locked lasers," p. CThI5, Optical Society of America, 2010.

[98] M. Zohar, M. Auslender, L. Faraone, and S. Hava, "Novel resonant cavity-enhanced absorber structures for high-efficiency midinfrared photodetector application," *J. Nanophoton.*, vol. 5, no. 1, p. 051824, 2011.

[99] F. Brückner, D. Friedrich, T. Clausnitzer, M. Britzger, O. Burmeister, K. Danzmann, E.-B. Kley, A. Tünnermann, and R. Schnabel, "Realization of a monolithic high-reflectivity cavity mirror from a single silicon crystal," *Phys. Rev. Lett.*, vol. 104, no. 16, p. 163903, 2010.

[100] F. Lu, F. G. Sedgwick, V. Karagodsky, C. Chase, and C. J. Chang-Hasnain, "Planar high-numerical-aperture low-loss focusing reflectors and lenses using subwavelength high contrast gratings," *Opt. Express*, vol. 18, no. 12, pp. 12606–12614, 2010.

[101] D. Fattal, J. Li, Z. Peng, M. Fiorentino, and R. G. Beausoleil, "Flat dielectric grating reflectors with focusing abilities," *Nat. Photon.*, vol. 4, no. 7, pp. 466–470, 2010.

[102] V. Karagodsky, C. Chase, and C. J. Chang-Hasnain, "Matrix Fabry–Perot resonance mechanism in high-contrast gratings," *Opt. Lett.*, vol. 36, no. 9, pp. 1704–1706, 2011.

[103] M. C. Y. Huang, Y. Zhou, and C. J. Chang-Hasnain, "A surface-emitting laser incorporating a high-index-contrast subwavelength grating," *Nat. Photon.*, vol. 1, no. 2, pp. 119–122, 2007.

[104] M. C. Y. Huang, Y. Zhou, and C. J. Chang-Hasnain, "A nanoelectromechanical tunable laser," *Nat. Photon.*, vol. 2, no. 3, pp. 180–184, 2008.

[105] V. Karagodsky, B. Pesala, F. G. Sedgwick, and C. J. Chang-Hasnain, "Dispersion properties of high-contrast grating hollow-core waveguides," *Opt. Lett.*, vol. 35, no. 24, pp. 4099–4101, 2010.

[106] Y. Zhou, V. Karagodsky, B. Pesala, F. G. Sedgwick, and C. J. Chang-Hasnain, "A novel ultra-low loss hollow-core waveguide using subwavelength high-contrast gratings," *Opt. Express*, vol. 17, no. 3, pp. 1508–1517, 2009.

[107] Y. Yue, L. Zhang, X. Wang, H. Huang, W. Yang, J. Ferrara, V. Karagodsky, C. Chase, M. Tur, C. Chang-Hasnain, and A. Willner, "Three-dimensional chirped high-contrast grating hollow-core waveguide," *IEEE Photonic Tech. Lett.*, vol. 4, no. 5, pp. 1372 –1380, 2012.

[108] H. Huang, Y. Yue, L. Zhang, C. Chase, D. Parekh, F. Sedgwick, M. Wu, C. Chang-Hasnain, M. Tur, and A. Willner, "Analog signal transmission in a high-contrast-gratings-based hollow-core-waveguide," *J. Lightwave Technol.*, vol. 30, no. 23, pp. 3640 –3646, 2012.

[109] M. G. Moharam and T. K. Gaylord, "Rigorous coupled-wave analysis of planar-grating diffraction," *J. Opt. Soc. Am.*, vol. 71, no. 7, pp. 811–818, 1981.

[110] M. G. Moharam, E. B. Grann, D. A. Pommet, and T. K. Gaylord, "Formulation for stable and efficient implementation of the rigorous coupled-wave analysis of binary gratings," *J. Opt. Soc. Am. A*, vol. 12, no. 5, pp. 1068–1076, 1995.

[111] M. Mutlu, A. E. Akosman, and E. Ozbay, "Broadband circular polarizer based on high-contrast gratings," *Opt. Lett.*, vol. 37, no. 11, pp. 2094–2096, 2012.

[112] M. Mutlu, A. E. Akosman, G. Kurt, M. Gokkavas, and E. Ozbay, "Broadband quarter-wave plates at near-infrared using high-contrast gratings," *Proc. SPIE 8633, High Contrast Metastructures II*, p. 86330O, 2013.

[113] E. D. Palik, *Handbook of optical constants of solids*. Academic Press, 1998.

[114] M. Mutlu, A. E. Akosman, G. Kurt, M. Gokkavas, and E. Ozbay, "Experimental realization of a high-contrast grating based broadband quarter-wave plate," *Opt. Express*, vol. 20, no. 25, pp. 27966–27973, 2012.

Appendix A

Publication List

1. M. Mutlu, A. E. Akosman, A. E. Serebryannikov, and E. Ozbay, "Asymmetric chiral metamaterial circular polarizer based on four U-shaped split ring resonators," Opt. Lett., vol. 36, pp. 1653–1655, 2011.

2. M. Mutlu, A. E. Akosman, A. E. Serebryannikov, and E. Ozbay, "Asymmetric transmission of linearly polarized waves and polarization angle dependent wave rotation using a chiral metamaterial," Opt. Express, vol. 19, no. 15, pp. 14290–14299, 2011.

3. A. E. Akosman, M. Mutlu, H. Kurt, and E. Ozbay, "Compact wavelength de-multiplexer design using slow light regime of photonic crystal waveguides," Opt. Express, vol. 19, no. 24, pp. 24129–24138, 2011.

4. M. Mutlu and E. Ozbay, "A transparent 90° polarization rotator by combining chirality and electromagnetic wave tunneling," Applied Physics Letters, vol. 100, no. 5, p. 051909, 2012.

5. M. Mutlu, A. E. Akosman, A. E. Serebryannikov, and E. Ozbay, "Diodelike asymmetric transmission of linearly polarized waves using magnetoelectric coupling and electromagnetic wave tunneling," Phys. Rev. Lett., vol. 108, p. 213905, 2012.

6. M. Mutlu, A. E. Akosman, and E. Ozbay, "Broadband circular polarizer

based on high-contrast gratings," Opt. Lett., vol. 37, pp. 2094–2096, 2012.

7. A. E. Akosman, M. Mutlu, H. Kurt, and E. Ozbay, "Dual-frequency division de-multiplexer based on cascaded photonic crystal waveguides," Physica B, vol. 407, pp. 4043–4047, 2012.

8. M. Mutlu, A. E. Akosman, G. Kurt, M. Gokkavas, and E. Ozbay, "Experimental realization of a high-contrast grating based broadband quarter-wave plate," Opt. Express, vol. 20, pp. 27966–27973, 2012.

9. Z. Li, M. Mutlu, and E. Ozbay, "Chiral metamaterials: from optical activity and negative refractive index to asymmetric transmission," J. Opt., vol. 15, p. 023001, 2013.

10. M. Mutlu, S. Cakmakyapan, A. E. Serebryannikov, and E. Ozbay, "One-way reciprocal spoof surface plasmons and relevant reversible diodelike beaming," Phys. Rev. B, vol. 87, p. 205123, 2013.

AMERICAN INSTITUTE OF PHYSICS LICENSE TERMS AND CONDITIONS

May 24, 2013

All payments must be made in full to CCC. For payment instructions, please see information listed at the bottom of this form.

License Number	3155340794597
Order Date	May 24, 2013
Publisher	American Institute of Physics
Publication	Applied Physics Letters
Article Title	A transparent 90° polarization rotator by combining chirality and electromagnetic wave tunneling
Author	Mehmet Mutlu, Ekmel Ozbay
Online Publication Date	Feb 3, 2012
Volume number	100
Issue number	5
Type of Use	Thesis/Dissertation
Requestor type	Author (original article)
Format	Print and electronic
Portion	Figure/Table
Number of figures/tables	3
Title of your thesis / dissertation	Chiral Metamaterial and High-Contrast Grating Based Polarization Selective Devices
Expected completion date	Jun 2013
Estimated size (number of pages)	150
Total	0.00 USD

Terms and Conditions

American Institute of Physics -- Terms and Conditions: Permissions Uses

American Institute of Physics ("AIP") hereby grants to you the non-exclusive right and license to use and/or distribute the Material according to the use specified in your order, on a one-time basis, for the specified term, with a maximum distribution equal to the number that you have ordered. Any links or other content accompanying the Material are not the subject of this license.

1. You agree to include the following copyright and permission notice with the reproduction of the Material: "Reprinted with permission from [FULL CITATION]. Copyright [PUBLICATION YEAR], American Institute of Physics." For an article, the copyright and permission notice must be printed on the first page of the article or book chapter. For photographs, covers, or tables, the copyright and permission notice may appear with the Material, in a footnote, or in the reference list.
2. If you have licensed reuse of a figure, photograph, cover, or table, it is your responsibility to ensure that the material is original to AIP and does not contain the copyright of another entity, and that the copyright notice of the figure, photograph, cover, or table does not indicate that it was reprinted by AIP, with permission, from another source. Under no circumstances does AIP, purport or intend to grant permission to reuse material to which it

does not hold copyright.

3. You may not alter or modify the Material in any manner. You may translate the Material into another language only if you have licensed translation rights. You may not use the Material for promotional purposes. AIP reserves all rights not specifically granted herein.
4. The foregoing license shall not take effect unless and until AIP or its agent, Copyright Clearance Center, receives the Payment in accordance with Copyright Clearance Center Billing and Payment Terms and Conditions, which are incorporated herein by reference.
5. AIP or the Copyright Clearance Center may, within two business days of granting this license, revoke the license for any reason whatsoever, with a full refund payable to you. Should you violate the terms of this license at any time, AIP, American Institute of Physics, or Copyright Clearance Center may revoke the license with no refund to you. Notice of such revocation will be made using the contact information provided by you. Failure to receive such notice will not nullify the revocation.
6. AIP makes no representations or warranties with respect to the Material. You agree to indemnify and hold harmless AIP, American Institute of Physics, and their officers, directors, employees or agents from and against any and all claims arising out of your use of the Material other than as specifically authorized herein.
7. The permission granted herein is personal to you and is not transferable or assignable without the prior written permission of AIP. This license may not be amended except in a writing signed by the party to be charged.
8. If purchase orders, acknowledgments or check endorsements are issued on any forms containing terms and conditions which are inconsistent with these provisions, such inconsistent terms and conditions shall be of no force and effect. This document, including the CCC Billing and Payment Terms and Conditions, shall be the entire agreement between the parties relating to the subject matter hereof.

This Agreement shall be governed by and construed in accordance with the laws of the State of New York. Both parties hereby submit to the jurisdiction of the courts of New York County for purposes of resolving any disputes that may arise hereunder.

If you would like to pay for this license now, please remit this license along with your payment made payable to "COPYRIGHT CLEARANCE CENTER" otherwise you will be invoiced within 48 hours of the license date. Payment should be in the form of a check or money order referencing your account number and this invoice number RLNK501028571. Once you receive your invoice for this order, you may pay your invoice by credit card. Please follow instructions provided at that time.

Make Payment To:
Copyright Clearance Center
Dept 001
P.O. Box 843006
Boston, MA 02284-3006

For suggestions or comments regarding this order, contact RightsLink Customer Support: customercare@copyright.com or +1-877-622-5543 (toll free in the US) or +1-978-646-2777.

Gratis licenses (referencing $0 in the Total field) are free. Please retain this printable license for your reference. No payment is required.